DISSERTATION

EVALUATING POTENTIAL LITHOLOGIC SOURCES OF SYN-RIFT MAGMATISM IN THE LITHOSPHERE AND ASTHENOSPHERE USING GEODYNAMIC MODELS

Submitted by

Micah Mayle

Department of Geosciences

In partial fulfillment of requirements

For the Degree of Doctor of Philosophy

Colorado State University

Fort Collins, Colorado

Spring 2026

Doctoral Committee:

Advisor: Dennis Harry

Derek Schutt
Eric Brown
Wolfgang Banger

ABSTRACT

EVALUATING POTENTIAL LITHOLOGIC SOURCES OF SYN-RIFT MAGMATISM IN THE LITHOSPHERE AND ASTHENOSPHERE USING GEODYNAMIC MODELS

Rifting and related magmatism are key processes associated with the fragmentation of continents and supercontinents. However, the sources of syn-rift magmatism are often disputed as early syn-rift magmatism is generally attributed to either elevated mantle temperatures from mantle plumes or the presence of fusible lithologies in the lithosphere and/or asthenosphere. In most cases, the mantle lithologies are not known. Neither are the relationships between the magmatic evolution of a rift and the thermal and geodynamic history of the rift clearly understood. In this dissertation, I evaluate the dynamics of melt generation from various proposed lithologic sources of syn-rift magmatism and the impacts such melting may have on the magmatic, thermal, and structural evolution of a rift.

To evaluate syn-rift melting behavior of fusible mantle sources I developed one-dimensional (1D) and two-dimensional (2D) geodynamic modeling packages. The 1D package, consisting of the MATLAB packages MELT1D and MELT1D2, computes pressure and temperature in an extending lithosphere and rising asthenosphere and calculates the resulting melt fraction, melting rates, and total melt produced during rifting for different common mantle lithologies. MELT1D does not include the latent heat of melting in the temperature calculation and thus calculates maximum melting scenarios. MELT1D2 includes the latent heat of melting in the temperature calculations and thus is a modification of MELT1D. The 2D package developed for this work consists of modifications of the finite-element geodynamic modeling code ASPECT (Advanced Solver for Planetary Evolution, Convection, and Tectonics). The modifications provided new functionality to evaluate melting/freezing and melt transport in a rheologically complex layered earth model.

To assess the relative timing of decompression melting of different protoliths in a compositionally heterogeneous mantle during rifting and the potential impacts of latent heat consumed during early syn-rift magmatism, two groups of 1D models were developed. The first group used MELT1D to create a series of 1D models that simulate syn-rift melt production from i) dry and wet mantle that are compositionally similar to those beneath mid-ocean ridges, ii) dry and wet relatively fertile ultramafic compositions, representing plume or primitive mantle material, iii) pyroxenite, representing recycled ultramafic oceanic crust or magmatic metasomes, and iv) basalt, representing recycled mafic crust or metasomes. These models were evaluated for the relative timing of syn-rift melting of each protolith across a wide range of rift conditions (e.g., mantle temperatures, lithosphere thickness, crustal thickness, extension rates). Model results predicted sequential melting of different mantle compositions that are broadly consistent with observed basalt eruption histories in many Phanerozoic rifts. Results showed a progressive transition in magma sources as the lithosphere thins, beginning with melting of wet mantle and compositionally fertile mafic components near the lithosphere-asthenosphere boundary during the earliest stages of tectonic extension. This transitions to magmatism dominated by melting of relatively fertile ultramafic components (pyrolitic and pyroxenitic compositions) as extension progresses, and finally to melting of ambient lherzolite asthenosphere as lithosphere thinning approaches continental breakup. Results also showed that mantle composition, pre-rift lithosphere thickness, and mantle temperature exert the greatest controls on the timing and volumes of magmas produced from each lithology. These models suggest that a cool or thick lithosphere has a greater capacity to sequester fertile lithologies than thin or warm lithosphere and thus has a greater capacity to produce early syn-rift magmas without requiring a hot mantle plume.

The second group of 1D models used MELT1D2 to evaluate three compositional models representing mantle composed of i) 100% lherzolite; ii) 85% lherzolite and 15% moderately fusible pyroxenite; and iii) 70% lherzolite, 15% moderately fusible pyroxenite, and 15% highly fusible

pyroxenite. These models were used to determine the impact that latent heat consumed during melting has on the thermal/structural evolution and thus magmatic evolution of a rift. The second group of models showed that consumption of latent heat during melting of the most fusible source rocks will enhance syn-rift cooling of the lower lithosphere and upper asthenosphere sufficiently to inhibit later syn-rift melting of less fusible rocks. Such cooling delays or may prevent later melting of moderately fusible lithologies. In the models, melting is primarily concentrated near the lithosphere-asthenosphere boundary, so this boundary is where the thermal evolution of the rift is most impacted by latent heat consumption. However, temperatures in this part of the mantle remained sufficiently high during rifting to prevent latent heat consumption due to mantle melting from having a significant impact on lithospheric strength.

Building on the results from the 1D geodynamic models which focused on fundamental rift processes, 2D models were applied to the West Antarctic Rift System (WARS) where various fusible mantle lithologies have been proposed as the sources of syn-rift magmatism. Five mantle compositional models were tested: i) 100% depleted lherzolite, ii) 100% fertile lherzolite, iii) 30% pyroxenite and 70% peridotite, iv) 30% basalt and 70% peridotite, and v) a reference model where no melting was permitted. The melting of each lithology is evaluated for a range of mantle potential temperatures T_p (1270 °C ≤ T_p ≤ 1330 °C) consistent with thermobarometric results and geodynamic models of previous WARS studies. The 2D WARS models consisted of a layered Earth with crust, lithosphere mantle, and upper asthenosphere layers which use flow laws for diorite, dunite, and lherzolite, respectively. Initial crust and lithosphere mantle thicknesses are 39 km and 141 km for East Antarctica and 45 km and 75 km for West Antarctica. A total extension rate of 7 mm yr^{-1} over 100 m.y. is simulated to reproduce the duration of rifting in the WARS from the Late Cretaceous to present. The models with cool mantle temperatures (T_p = 1300 °C) best reproduced the known structural and magmatic evolution of the WARS. Results also showed that of all lithologies evaluated, only basaltic sources in the mantle would melt during WARS rifting. During the modeled initial Cretaceous broad rifting phase (~100 – 50 Ma), broad melting of basaltic sources occurs in the asthenosphere spanning the Ross Sea but achieves only 7% maximum melt by the end of the rifting phase at ~50 Ma. During the modeled Cenozoic narrow rifting phase (50 Ma – present), the focus of melting shifted to the asthenosphere underlying the western flank of the Ross Sea region, while melting ceased under the rest of the Ross Sea. The models do not include high-temperature mantle plume effects, suggesting that syn-rift melting of basalt or other lithologies with high fusibilities are sufficient to produce observed Cenozoic volcanism along the western margin of the Ross Sea though this does not preclude the presence of an underlying plume beneath Ross Island. However, the absence of melting at the modeled eastern margin of the Ross Sea (i.e. Marie Byrd Land) suggested that elevated temperatures such as those associated with a mantle plume are necessary for Cenozoic magmatism.

ACKNOWLEDGEMENTS

I am sincerely appreciative of the people in my life who gave me the opportunity to pursue this degree and to those who supported me throughout its completion. I would first like to thank my advisor, Dennis Harry, for all of your support, trust, and training but most of all for helping me grow as a researcher and scientist. I am truly grateful for the opportunity you gave me to conduct this research, and I consider myself lucky to have had such a good teacher and advocate. I would also like to thank my committee members, Derek Schutt, Eric Brown, and Wolfgang Bangerth, for always making time to discuss my research or answer questions despite how demanding your schedules are.

I would like to thank my collaborators, mentors, and colleagues who helped me along this journey. Thank you to my mentors and previous advisors, Estella Atekwana and Kevin Mickus. I would not be where I am without your help and guidance. Thank you to Folarin Kolawole who is a great scientist and an even better friend. I am also grateful for the graduate students at Colorado State University (past and present students) who truly created a strong sense of community and a steadfast support system. I am extremely grateful for Jimmy, Lindsay, Manny, Noah, Andrew, David, Jorge, Michael, Hank, and Nikki.

I could not have done this without the love and support of my family and friends. To my parents, Michael and Shelley Mayle, I do not have the words to explain how grateful I am for everything that you have done. To my wife, Stephanie, who has made completing this research and achieving this degree remotely possible, you have all of my love and eternal gratitude.

TABLE OF CONTENTS

INTRODUCTION

The fragmentation of continents, driven by extension of the lithosphere along rifts, is often accompanied by magmatism attributed to decompression melting of the mantle, and ultimately leading to break-up and generation of new oceanic crust (McKenzie & Bickle, 1988). Early syn-rift magmas are generally alkaline and are thought to be produced by low percentage melting of the rising asthenosphere. As rifts mature and extension increases, higher percent melting leads to a progression toward tholeiitic basalt, ultimately producing new oceanic crust (Hirose & Kushiro, 1993; Kushiro, 1996; Wasylenki et al., 2003). The source of syn-rift melting is generally thought to be the upper mantle (e.g., dry lherzolite) responsible for producing Mid Ocean Ridge Basalts (MORBs) depleted in incompatible trace elements and radiogenic isotopes (high ^{143}Nd/^{144}Nd and low ^{87}Sr/^{86}Sr and ^{206}Pb/^{204}Pb) and commonly referred to as depleted MORB mantle (DMM) (Hart et al., 1992; Zindler & Hart, 1986). While variations in timing and volume of syn-rift magmatism can be attributed to differences in mantle temperatures, a growing geochemical database has shown that simple decompression melting of a DMM source such as dry lherzolite is not sufficient to explain the trace element and isotopic compositions observed in many early syn-rift magmatic rocks (Hirschmann et al., 2003; Pilet, 2015; Pilet et al., 2008, 2011). Several studies have appealed to the melting of more fusible sources than ambient mantle (dry lherzolite) to explain early syn-rift magmatism in continental rifts such as in the East Africa Rift System (Furman et al., 2016; Rooney, 2020) and the West Antarctic Rift System (WARS) (Aviado et al., 2015; Panter et al., 2018; Panter & Martin, 2023). These proposed fusible sources include hydrated phases (e.g., wet lherzolite), pyroxenite, and eclogite and are attributed to compositional heterogeneities within the lithospheric and sub-lithospheric mantle. The heterogeneities are often associated with prior tectonomagmatic events such as previous magmatism/metasomatism related to mantle plumes or subduction (Aviado et al., 2015; Hart et al., 1997; Panter et al., 2000; Rooney, 2020).

While it is generally accepted that fusible sources in the lithosphere and/or asthenosphere play a role in syn-rift magmatism, many questions remain. For example, if fusible lithologies were present, would they melt and what impacts would the resulting melt have on the structural development of a rift? Specifically, if multiple lithologies are present in the mantle, at what stage of rifting would each source contribute to melt generation during the life of the rift? Similarly, how would early melting of different lithologies impact the magmatic, thermal, and structural evolution of the rift?

In this dissertation, I explore the melting conditions and behaviors of various proposed mantle sources of syn-rift melts using geodynamic models. Here, I present 1D (one-dimensional) and 2D (two-dimensional) models of rifting and associated magmatism which are used to test the fundamental hypothesis that magmatism observed at different stages in rifting is produced by different lithologic sources.

This dissertation consists of three chapters that are formatted and written as stand-alone manuscripts. In the first chapter, I test the melting of various lithologic mantle sources in a simple 1D model of extension. To simulate melting, I developed a new 1D modeling code in MATLAB, MELT1D, which considers a simple area balance to calculate pressure-temperature conditions generated during rifting. A series of compositional models simulate syn-rift melt production from i) dry and wet mantle compositionally similar to that beneath midocean ridges, ii) dry and wet relatively fertile ultramafic compositions representing plume or primitive mantle material, iii) pyroxenite representing recycled ultramafic oceanic crust or magmatic metasomes, and iv) basalt representing recycled mafic crust or metasomes. These 1D models evaluate melting of different lithologies in a wide range of continental rift conditions (i.e., various crustal and lithosphere thicknesses, temperatures, extension rates) that span global rift conditions. Notably the 1D models do not consider the latent heat of melting and thus evaluate the maximum amount of melt that may be produced during rifting by each lithology. Fundamentally this chapter addresses when different lithologic sources contribute to syn-rift magmatism (in relation to the stages of rifting) and thus what would the sequence of melting be in a multi-lithology mantle. In this chapter, I also evaluate the first-order melting behavior of various lithologic sources such as timing, melt production, and depth of maximum melting. Chapter 1 has been published in the *Journal of Geophysical Research: Solid Earth* (Mayle & Harry, 2023).

In the second chapter, I use similar models tested in the first chapter but consider the latent heat of melting. I show this may have a significant impact on the thermal evolution of a rift, and thus its magmatic and structural evolution. To accomplish this, MELT1D was modified to include the latent heat of melting in the temperature calculations in the lithosphere and asthenosphere resulting in a new geodynamic tool, MELT1D2. Three mantle compositions were considered: a model with a mantle consisting of 100% depleted lherzolite which we refer to as depleted mantle , a model with a mantle consisting of 85% depleted lherzolite and 15% moderately fusible pyroxenite which we refer to as a moderately metasomatized mantle, and a model consisting of 70% depleted lherzolite, 15% moderately fusible pyroxenite, and 15% highly fusible pyroxenite which we refer to as a highly metasomatized mantle. These compositional models were evaluated for decompression melting in a global average rift model (e.g., 120 km thick lithosphere and mantle potential temperature of 1350 °C). The resulting temperatures of the models were then used to generate yield stress envelopes of the lithosphere to determine how and if the heat loss due solely to associated syn-rift melting affects lithospheric strength and how this might impact rifting. This chapter addresses the impacts of the latent heat of melting on syn-rift magmatism and presents implications to rifting and related magmatism of multi-lithology mantle sources which have been hypothesized for various rift systems. Chapter 2 has been prepared for submission to *Geology*.

In the third chapter, I evaluate the role that melting of fusible lithologies had on the structural and magmatic evolution of the WARS. This chapter utilizes insights gained from the first two chapters (which used simple 1D models) to test magmatism and rifting in 2D models constrained by geologic and geophysical observations from the WARS. To complete this work, I modified the finite-element modeling code, ASPECT (Advanced Solver for Planetary Evolution, Convection, and Tectonics) (Bangerth et al., 2024b, 2024a; Dannberg & Heister, 2016; Heister et al., 2017; Kronbichler et al., 2012), to allow for the evaluation of melting in a layered earth model with different rheologies. I also added new lithologic sources to be evaluated for melting (i.e., fertile lherzolite, pyroxenite, and basalt) and new functionality that ensures that the starting model does not contain more of a given composition than the initial pressure-temperature conditions allow. Using the new modifications, I tested 2D WARS models for the melting of mantle lithologies spanning a wide range of fusibilities (e.g., depleted and fertile lherzolite, pyroxenite, and basalt). These models are evaluated for different temperature models that range from cold mantle (1270 °C) to warm mantle (1330 °C) which are constrained by thermobarometric estimates (Armienti & Perinelli, 2010; Perinelli et al., 2006, 2011) and previous geodynamic models of the WARS (Bialas et al., 2007; Harry et al., 2018; Huerta & Harry, 2007; van Wijk et al., 2008). This chapter tests previously proposed hypotheses that attribute WARS syn-rift magmatism to melting of fusible lithologies in the lithosphere and asthenosphere (Aviado et al., 2015; Panter et al., 2018; Panter & Martin, 2023) and to determine how/if melting of such sources impacts the structural and magmatic evolution of the rift. Chapter 3 was prepared for submission to *Geophysics, Geochemistry, and Geosystems*.

References

Armienti, P., & Perinelli, C. (2010). Cenozoic thermal evolution of lithospheric mantle in northern Victoria Land (Antarctica): Evidences from mantle xenoliths. Tectonophysics, 486(1), 28–35. https://doi.org/https://doi.org/10.1016/j.tecto.2010.02.006

Aviado, K. B., Rilling-Hall, S., Bryce, J. G., & Mukasa, S. B. (2015). Submarine and subaerial lavas in the West Antarctic Rift System: Temporal record of shifting magma source components from the lithosphere and asthenosphere. Geochemistry, Geophysics, Geosystems, 16(12), 4344–4361. https://doi.org/10.1002/2015GC006076

Bangerth, W., Dannberg, J., Fraters, M., Gassmoeller, R., Glerum, A., Heister, T., Myhill, R., & Naliboff, J. (2024a). ASPECT: Advanced Solver for Planetary Evolution, Convection, and Tectonics, User Manual. https://doi.org/10.6084/m9.figshare.4865333

Bangerth, W., Dannberg, J., Fraters, M., Gassmoeller, R., Glerum, A., Heister, T., Myhill, R., & Naliboff, J. (2024b). ASPECT v3.0.0. Zenodo. https://doi.org/10.5281/zenodo.14371679

Bialas, R. W., Buck, W. R., Studinger, M., & Fitzgerald, P. G. (2007). Plateau collapse model for the transantarctic mountains-West Antarctic rift system: Insights from numerical experiments. Geology, 35(8), 687–690. https://doi.org/10.1130/G23825A.1

Dannberg, J., & Heister, T. (2016). Compressible magma/mantle dynamics: 3D, adaptive simulations in ASPECT. Geophysical Journal International, 207(3), 1343–1366. https://doi.org/10.1093/gji/ggw329

Furman, T., Nelson, W. R., & Elkins-Tanton, L. T. (2016). Evolution of the East African rift: Drip magmatism, lithospheric thinning and mafic volcanism. Geochimica et Cosmochimica Acta, 185, 418–434. https://doi.org/https://doi.org/10.1016/j.gca.2016.03.024

Harry, D. L., Anoka, J. L., & Jha, S. (2018). Geodynamic models of the West Antarctic Rift System: Implications for the mantle thermal state. Geosphere, 14(6), 2407–2429. https://doi.org/10.1130/GES01594.1

Hart, S. R., Blusztajn, J., LeMasurier, W. E., & Rex, D. C. (1997). Hobbs Coast Cenozoic volcanism: Implications for the West Antarctic rift system. Chemical Geology, 139(1–4), 223–248. https://doi.org/10.1016/S0009-2541(97)00037-5

Hart, S. R., Hauri, E. H., Oschmann, L. A., & Whitehead, J. A. (1992). Mantle plumes and entrainment: Isotopic evidence. Science, 256(5056), 517–520. https://doi.org/10.1126/science.256.5056.517

Heister, T., Dannberg, J., Gassmöller, R., & Bangerth, W. (2017). High accuracy mantle convection simulation through modern numerical methods. II: Realistic models and problems. Geophysical Journal International, 210(2), 833–851. https://doi.org/10.1093/gji/ggx195

Hirose, K., & Kushiro, I. (1993). Partial melting of dry peridotites at high pressures: Determination of compositions of melts segregated from peridotite using aggregates of diamond. Earth and Planetary Science Letters, 114(4), 477–489. https://doi.org/10.1016/0012-821X(93)90077-M

Hirschmann, M. M., Kogiso, T., Baker, M. B., & Stolper, E. M. (2003). Alkalic magmas generated by partial melting of garnet pyroxenite. Geology, 31(6), 481–484. https://doi.org/10.1130/0091-7613(2003)031<0481:AMGBPM>2.0.CO;2

Huerta, A. D., & Harry, D. L. (2007). The transition from diffuse to focused extension: Modeled evolution of the West Antarctic Rift system. Earth and Planetary Science Letters, 255(1–2), 133–147. https://doi.org/10.1016/j.epsl.2006.12.011

Kronbichler, M., Heister, T., & Bangerth, W. (2012). high accuracy mantle convection simulation through modern numerical methods. Geophysical Journal International, 191, 12–29. https://doi.org/10.1111/j.1365-246X.2012.05609.x

Kushiro, I. (1996). Partial melting of a fertile mantle peridotite at high pressures: An experimental study using aggregates of diamond. In Earth Processes: Reading the Isotopic Code (pp. 109–122). American Geophysical Union (AGU). https://doi.org/https://doi.org/10.1029/GM095p0109

Mayle, M., & Harry, D. L. (2023). Syn-rift magmatism and sequential melting of fertile lithologies in the lithosphere and asthenosphere. Journal of Geophysical Research: Solid Earth, 128(9), e2023JB027072. https://doi.org/https://doi.org/10.1029/2023JB027072

McKenzie, D., & Bickle, M. J. (1988). The volume and composition of melt generated by extension of the lithosphere. Journal of Petrology, 29(3), 625–679. https://doi.org/10.1093/petrology/29.3.625

Panter, K. S., Castillo, P., Krans, S., Deering, C., McIntosh, W., Valley, J. W., Kitajima, K., Kyle, P., Hart, S., & Blusztajn, J. (2018). Melt origin across a rifted continental margin: A case for subduction-related metasomatic agents in the lithospheric source of alkaline basalt, NW Ross Sea, Antarctica. Journal of Petrology, 59(3), 517–558. https://doi.org/10.1093/petrology/egy036

Panter, K. S., Hart, S. R., Kyle, P., Blusztanjn, J., & Wilch, T. (2000). Geochemistry of Late Cenozoic basalts from the Crary Mountains: Characterization of mantle sources in Marie Byrd Land, Antarctica. Chemical Geology, 165(3–4), 215–241. https://doi.org/10.1016/S0009-2541(99)00171-0

Panter, K. S., & Martin, A. P. (2023). West Antarctic mantle deduced from mafic magmatism. In A. P. Martin & W. van der Wal (Eds.), The Geochemistry and Geophysics of the Antarctic Mantle (pp. 133–149). Geological Society of London, Memoirs. https://doi.org/10.1144/M56-2021-10

Perinelli, C., Armienti, P., & Dallai, L. (2006). Geochemical and O-isotope constraints on the evolution of lithospheric mantle in the Ross Sea rift area (Antarctica). Contributions to Mineralogy and Petrology, 151(3), 245–266. https://doi.org/10.1007/s00410-006-0065-8

Perinelli, C., Armienti, P., & Dallai, L. (2011). Thermal evolution of the lithosphere in a rift environment as inferred from the geochemistry of mantle cumulates, Northern Victoria Land, Antarctica. Journal of Petrology, 52(4), 665–690. https://doi.org/10.1093/petrology/egq099

Pilet, S. (2015). Generation of low-silica alkaline lavas: Petrological constraints, models, and thermal implications. In G. R. Foulger, M. Lustrino, & S. D. King (Eds.), The Interdisciplinary Earth: A Volume in Honor of Don L. Anderson (pp. 281–304). Geological Society of America. https://doi.org/10.1130/2015.2514(17)

Pilet, S., Baker, M. B., Müntener, O., & Stolper, E. M. (2011). Monte Carlo simulations of metasomatic enrichment in the lithosphere and implications for the source of alkaline basalts. Journal of Petrology, 52(7–8), 1415–1442. https://doi.org/10.1093/petrology/egr007

Pilet, S., Baker, M. B., & Stolper, E. M. (2008). Metasomatized lithosphere and the origin of alkaline lavas. Science, 320(5878), 916–919. https://doi.org/10.1126/science.1156563

Rooney, T. O. (2020). The Cenozoic magmatism of East Africa: Part V – Magma sources and processes in the East African Rift. Lithos, 360–361, 105296. https://doi.org/10.1016/j.lithos.2019.105296

van Wijk, J. W., Lawrence, J. F., & Driscoll, N. W. (2008). Formation of the Transantarctic Mountains related to extension of the West Antarctic Rift system. Tectonophysics, 458(1–4), 117–126. https://doi.org/10.1016/j.tecto.2008.03.009

Wasylenki, L. E., Baker, M. B., Kent, A. J. R., & Stolper, E. M. (2003). Near-solidus melting of the shallow upper mantle: Partial melting experiments on depleted peridotite. Journal of Petrology, 44(7), 1163–1191. https://doi.org/10.1093/petrology/44.7.1163

Zindler, A., & Hart, S. (1986). Chemical geodynamics. Annual Review of Earth and Planetary Sciences, 14, 493–571.

CHAPTER 1: SYN-RIFT MAGMATISM AND SEQUENTIAL MELTING OF FERTILE LITHOLOGIES IN THE LITHOSPHERE AND ASTHENOSPHERE[1]

1.1. Introduction

Continental rifting often leads to decompression melting of the rising mantle and associated basaltic magmatism. Melting of dry lherzolite asthenosphere (ambient mantle) typically begins when the lithosphere has thinned to ca. 60–65 km (McKenzie & Bickle, 1988), assuming the mantle potential temperature is similar to the global average T_p = 1350°C (Lee et al., 2009). Assuming an initial lithosphere thickness of 120 km, this requires ∼100% extension prior to the onset of magmatism. Decompression of rising asthenosphere initially results in low degree partial melting at depth, producing alkali basaltic melts (Hirose & Kushiro, 1993; Kushiro, 1996; Wasylenki et al., 2003). As extension continues and the lithosphere thins further, the degree of melting in the rising asthenosphere increases, leading to a transition toward larger melt volume and more tholeiitic compositions. This scenario accounts for middle and late stage syn-rift magmatism and the transition to seafloor spreading on many rifted continental margins, with mantle potential temperature playing a key role in determining the volume and temporal pattern of magmatism (Brown & Lesher, 2016; McKenzie & Bickle, 1988). However, in many continental rifts magmatism began before the lithosphere had sufficiently thinned to produce decompression melting in rising dry lherzolite asthenosphere, even at elevated mantle temperatures. Examples include the West Antarctic Rift System (WARS), the East African Rift System (EARS), and the western North American Basin and Range province (Aviado et al., 2015; Leeman & Harry, 1993; McMillan et al., 2000; Rooney, 2020).

---

[1] Chapter 1 is published in the *Journal of Geophysical Research: Solid Earth* as “Syn-rift magmatism and sequential melting of fertile lithologies in the lithosphere and asthenosphere” (Mayle and Harry, 2023).

Trace element and isotopic compositions of early syn-rift alkaline basalts in these extensional provinces are typically enriched in incompatible elements compared to mid-ocean ridge basalts (MORB) (e.g., Panter et al., 2018; Pitcavage et al., 2021). The enriched geochemical signatures of the early alkaline basalts support arguments for melting of a mantle source that is distinct from the depleted MORB source (dry lherzolite) (Hirschmann et al., 2003; Pilet et al., 2008, 2011). Consequently, various fertile and/or metasomatic sources in the lithosphere and asthenosphere have been proposed to explain the early melting and distinct geochemical characteristics of the juvenile syn-rift magmas. These include dry mafic and ultramafic compositions (eclogite and pyroxenite), relatively fertile (in comparison to depleted MORB source) primitive mantle lherzolite, and lherzolite metasomatized by hydrous or CO2-enriched fluids (Allègre & Turcotte, 1986; Fitton et al., 1991; Gallagher & Hawkesworth, 1992; Lum et al., 1989; Pilet, 2015; Pilet et al., 2008).

Previous geodynamic models have demonstrated that melting of mafic (basaltic) lithologies previously sequestered as intrusions in the lower lithosphere can reproduce the major element, trace element, and broad-scale temporal patterns of early syn-rift magmatism in the Basin and Range province (e.g., Harry & Leeman, 1995; Leeman & Harry, 1993). These models showed that melt production from such fertile lithosphere sources declines with time due to cooling of the extending lithosphere and/or consumption of the mafic components. Melting of dry asthenosphere begins after melting of mafic lithosphere sources. Magmatism becomes progressively more dominated by decompression melting of the rising asthenosphere thereafter. In this paper, we build on this previous work to consider a broader range of source rock compositions for early syn-rift melt production and consider melt production from fertile components in both the lithosphere and asthenosphere.

To simulate melt production during continental rifting we developed MELT1D, a MATLAB program that computes the timing and volume of syn-rift magmatism for a variety of mantle lithologies. MELT1D computes the 1D (one-dimensional) pressure and temperature (P-T) paths of rock packets rising beneath the rift axis. These P-T paths are used to compute the melt fraction as a function of depth and the total volume of melt produced as a function of time. MELT1D computes the melt production for any source rock composition given equations describing the solidus, liquidus, and melting function. In this paper, we consider melting of several compositions that are taken to represent dry primitive and depleted mantle, hydrous mantle, and anhydrous fertile ultramafic and mafic metasomes. To understand melt production from these proposed sources of syn-rift magmatism, we present a series of MELT1D models using initial and boundary conditions that span the range of realistic rift scenarios. Specifically, we examine impacts on syn-rift melt production that arise from variations in mantle potential temperature, extension rate, the pre-rift thickness of the crust and lithosphere, crustal heat production, and initial width of the extensional province.

1.2. 1D Numerical modeling of rifting and decompression melting

We use the 1D modeling method described by Harry and Leeman (1995) to compute P-T curves as a function of time and depth in the thinning lithosphere during extension (Appendix A1). This method utilizes a Lagrangian formulation to track the P and T for specific nodes at different depths in the lithosphere through time. We assume heat production decays exponentially with depth in the crust, and that there is no heat production in the mantle. The P-T curve in the asthenosphere is defined to be adiabatic and is specified by the mantle potential temperature and adiabatic gradient. Additional boundary conditions include a constant extension rate and a constant temperature at the surface. A time-stepping method is used, in which the thickness of the crust and lithosphere are incrementally decreased as the extensional province widens. The temperature field for the lithosphere at the new time is determined using a fourth order Runge-Kutta finite difference method, and updated density and pressure profiles are then calculated. The temperature at the base of the lithosphere is prescribed to be equal to the asthenosphere adiabatic temperature at all time steps. Initial and boundary conditions and thermal parameters used in the models are shown in Tables 1.1 and 1.2.

Table 1.1. Model Parameters

Model	Crustal thickness (km)	Lithospheric thickness (km)	Initial rift width (km)	Mantle potential temperature (°C)	Extension rate (mm/yr)	Surface heat production rate (W m^{-3})
Reference	40	120	200	1350	10	1.5×10^{-6}
Cold	40	120	200	1300	10	1.5×10^{-6}
Hot	40	120	200	1400	10	1.5×10^{-6}
High Crust Heat Generation	40	120	200	1350	10	10×10^{-6}
No Crust Heat Generation	40	120	200	1350	10	0
Thick Lithosphere	40	200	200	1350	10	1.5×10^{-6}
Thin Lithosphere	40	80	200	1350	10	1.5×10^{-6}
Thick Crust	60	120	200	1350	10	1.5×10^{-6}
Thin Crust	10	120	200	1350	10	1.5×10^{-6}
Narrow	40	120	50	1350	10	1.5×10^{-6}
Wide	40	120	1000	1350	10	1.5×10^{-6}
Fast	40	120	200	1350	20	1.5×10^{-6}
Slow	40	120	200	1350	1	1.5×10^{-6}

Note. Parameter ranges span typical global rift systems as described in Section 1.3.1.

The P-T curves at each time step are used to estimate melt fraction at every depth node for each of the various lithologies. For each lithology, the difference in melt fraction between time steps is integrated over depth to get the total amount of melt generated in each time step (represented by the equivalent melt thickness). For simplicity and speed of computation, the latent heat of fusion during melting is not considered during the discussion here. The resulting mantle temperatures, melt fractions, and total melt volumes are therefore interpreted as maxima (e.g., Bown & White, 1995).

Table 1.2. Thermal and Physical Parameters

Surface Temperature[a]	0 °C
Mantle Potential Temperature[b]	1300 - 1400 °C
Mantle Adiabatic Gradient[c]	4×10^{-4} °C m^{-1}
Crust	
Surface Heat Production Rate[b]	$0 - 10 \times 10^{-6}$ W m^{-3}
Heat Production Decay Constant[a]	10 km
Thermal Conductivity[a]	2.5 W m^{-1} °C^{-1}
Specific Heat[a]	875 J kg^{-1} °C^{-1}
Thermal Expansion Coefficient[d]	3.1×10^{-5} °C^{-1}
Compressibility Coefficient[e]	1×10^{-11} Pa^{-1}
Density[a]	2900 kg m^{-3}
Mantle	
Thermal Conductivity[e]	3.3 W m^{-1} °C^{-1}
Specific Heat[a]	1250 J kg^{-1} °C^{-1}
Thermal Expansion Coefficient[d]	3.1×10^{-5} °C^{-1}
Compressibility Coefficient[e]	1×10^{-11} Pa^{-1}
Density[a]	3330 kg m^{-3}

[a] Values taken from Leeman and Harry (1993).
[b] Parameter ranges chosen to represent global rift systems are described in detail in Section 1.3.1.
[c] Values taken from Katsura et al. (2010).
[d] Values taken from Huerta and Harry (2007).
[e] Values taken from Turcotte and Schubert (2002).

In this paper, we consider melting of six lithologies that are commonly invoked as potential sources of syn-rift magmatism: (a) hydrous, (b) anhydrous depleted MORB mantle (DMM), which we take to represent hydrated and dry ambient upper mantle, (c) dry pyrolite which we take to represent a more fertile dry primitive mantle, (d) wet pyrolite, representing hydrated primitive mantle, (e) pyroxenite, and (f) basalt which respectively represent fertile ultramafic and mafic rocks entrained in the mantle during prior subduction, plume, or magmatic episodes. We use the melting functions of Brown and Lesher (2016) for DMM, pyrolite, and pyroxenite and the melting function of Harry and Leeman (1995) for basalt (Appendix A1). We have chosen the MIX1G pyroxenite (Hirschmann et al., 2003), which represents a global average pyroxenite composition. We evaluate each of these candidate lithologies as if they were present in the lithosphere and/or asthenosphere. While we recognize that subduction modified mantle may have greater water content, the melting of hydrous mantle is modeled using wet DMM and pyrolite compositions assuming 1,000 ppm H_2O prior to melting. We take this to be an upper bound on primitive mantle water content beneath continental rifts (Palme & O'Neill, 2014). Melt production from the lithosphere and asthenosphere for each of these hypothesized source compositions are tracked separately and scaled by their assumed fractional abundances in the pre-rift mantle. Models simulating melting of hydrous and anhydrous DMM and pyrolite assume those compositions make up the entirety of the lithosphere or asthenosphere mantle. To facilitate easy graphical comparison of model results, the volumes of melt produced by pyroxenite and basalt are scaled. The scaling implemented represents a mantle containing 10% pyroxenite or basalt by volume prior to rifting, which we consider to be representative of a slightly metasomatized mantle. The volume of melt predicted by the models would be proportionately higher if the pre-rift volumetric abundance of these compositions in the mantle was greater than 10% prior to rifting. However, the amounts of extension necessary for each candidate lithology to begin melting and to achieve peak melt production rates are independent of the assumed pre-rift abundance of that lithology in our model parameterization. Thus, we focus our discussion of model results on the relative timing of melt production from each candidate lithology, as measured by the amount of extension that occurs before the onset of magmatism and before peak melt production rates are achieved.

Our 1D formulation of rifting has limitations. The model only considers vertical heat flow, which is most applicable at the center of a moderately wide rift. Lateral heat flow may be significant in narrow rifts, near the margins of broad extensional provinces, and in very slow rift systems. Our models thus overestimate melt production and underestimate time elapsed between the onset of extension and onset of melting in such circumstances. Another limitation involves the widening of a rift over time. The 1D parameterization assumes that the lithosphere deforms by pure shear and thus maintains area balance, such that the lithosphere becomes thinner and the rate of lithospheric thinning decreases as the region extends and becomes wider. Natural rifts, however, often show a narrowing of the rift as strain is localized along the axis where the temperatures are elevated. This causes thinning rates near the rift axis to be higher than shown in the models as the rift matures. A final limitation of MELT1D is that our model formulation neglects the latent heat of melting. This is due to two reasons. First, a design goal of MELT1D was to include a broad spectrum of candidate source rock lithologies. This required inclusion of published melt fraction, solidus, and liquidus curves that lack corresponding data constraining the latent heat of fusion. Second, determining the thermal effect of the latent heat of fusion requires a nonlinear iterative solver (e.g., Brown & Lesher, 2016) that greatly increases MELT1D run time. Another design goal of MELT1D is to facilitate rapid comparison of different model scenarios, requiring short run times. Neglecting latent heat causes MELT1D to overestimate the mantle temperatures in the partial melt zone, thus overestimating the volume of melt production. However, the relative timing of onset of magmatism and peak melt production from different compositions in the mantle are not affected. Thus, the melt production and thickness plots for the lithosphere and asthenosphere are each normalized.

1.3. Results

1.3.1. Reference model: a typical rifting scenario

A reference model was constructed to approximate global average rift conditions (Tables 1.1 and 1.2). This model uses a global average mantle potential temperature of 1350°C (Lee et al., 2009). A surface heat production rate of 1.5×10^{-6} W m^{-3} was assumed which approximates the rate of upper crustal heat production from the global geochemical model of Rudnick and Gao (2014). The initial crust thickness of 40 km and initial lithosphere thickness of 120 km approximate global averages for continental crust (Szwillus et al., 2019) and lithosphere (Steinberger & Becker, 2018). The model extension rate of 10 mm yr^{-1} is an

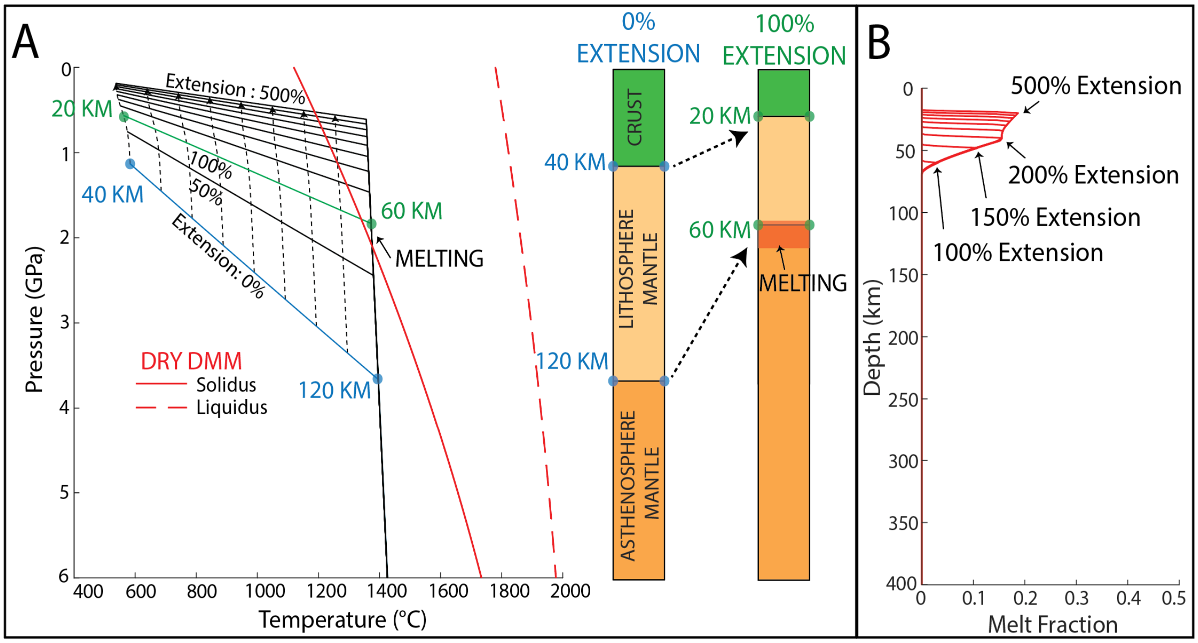

Figure 1.1. A) Reference model pressure–temperature (P-T) plot compared with solidus (dotted red line) and liquidus (dashed red line) of DMM. Subvertical dashed lines show P-T paths of packets of rock positioned at 10 km interval depths prior to rifting, from the base of the crust to the base of the lithosphere. Solid lines show P-T conditions in the lithosphere (sub-horizontal lines) and asthenosphere (subvertical black line) after indicated amounts of extension. Profiles at right show model after 0% and 100% extension. Orange shading indicates partial melting. B) Melt fraction vs depth. Melting begins at slightly less than 100% extension with the greatest degree of melting occurring near the lithosphere-asthenosphere boundary.

estimate of the mean extension rate for active continental rifts (Tetreault & Buiter, 2018). Figure 1.1a shows the P-T conditions in the reference model mantle after different amounts of extension, from 0% to 500% (subhorizontal lines). The subvertical lines show P-T paths for packets of rock in the lithosphere that initially were spaced at 10 km intervals at depths of 40 (the base of the crust) to 120 km (the base of the lithosphere) prior to rifting. The rightmost subvertical line represents the mantle adiabat, which is the path followed by the ascending asthenosphere. Before extension, the base of the crust lies at 1.1 GPa and 586 °C and the base of the lithosphere lies at 3.7 GPa and 1397 °C. After 500% extension, the base of the crust lies at 0.2 GPa and 539 °C while the base of the lithosphere lies at 0.6 GPa and 1358 °C. If dry DMM is present in the lithosphere or asthenosphere, it will begin to melt after about 75% extension, when the lithosphere-asthenosphere boundary (LAB) crosses the solidus (Figure 1.1a). With continued extension, the LAB moves further into the super-solidus field while previously un-melted portions of the overlying lithosphere and underlying asthenosphere cross the solidus and begin to melt. The top of the melt column thus expands upward to include a greater portion of the lower lithosphere as extension progresses. At the same time, thinning of the lithosphere causes the zone of melting to incorporate a greater portion of the underlying rising asthenosphere. The partial melt zone thus encompasses the lowermost lithosphere and uppermost asthenosphere, with the highest degree of melting occurring at the LAB (Figure 1.1b). The rate of melt production from dry DMM in the reference model lithosphere peaks soon after 150% extension (Figure 1.2a). The melt production rate from dry DMM in the asthenosphere peaks at 185% extension (Figure 1.2b). The decrease in the rate of melt production at greater amounts of extension is a result of a decrease in the thinning rate (Figure 1.2c), which itself is a result of maintaining area balance in the model (Harry & Leeman, 1995).

In the reference model, the lithosphere and asthenosphere lie below the dry pyrolite and pyroxenite solidi prior to rifting but the LAB and portions of the lowermost lithosphere and uppermost asthenosphere are above the basalt solidus (Figure 1.3a). Thus, the upper mantle is too warm to sequester basaltic compositions. If any basalt was once present in this portion of the mantle, it would have partially melted before rifting began. In our models, we treat this partial melt predicted prior to the onset of extension as having been extracted prior to rifting and do not consider it in the syn-rift melt production calculations.

At the onset of extension, decompression causes the LAB to move further into the basalt super-solidus field and portions of the overlying lithosphere and underlying asthenosphere to pass into the super-solidus field. This leads to further melting and the production of early syn-rift magmas. In the reference model, the melt production rate from basalt entrained in the lithospheric mantle is at its maximum at the onset of extension (Figure 1.3b) and declines monotonically thereafter. Melt production rates from basaltic components entrained in the asthenosphere peaks after around 15% extension and

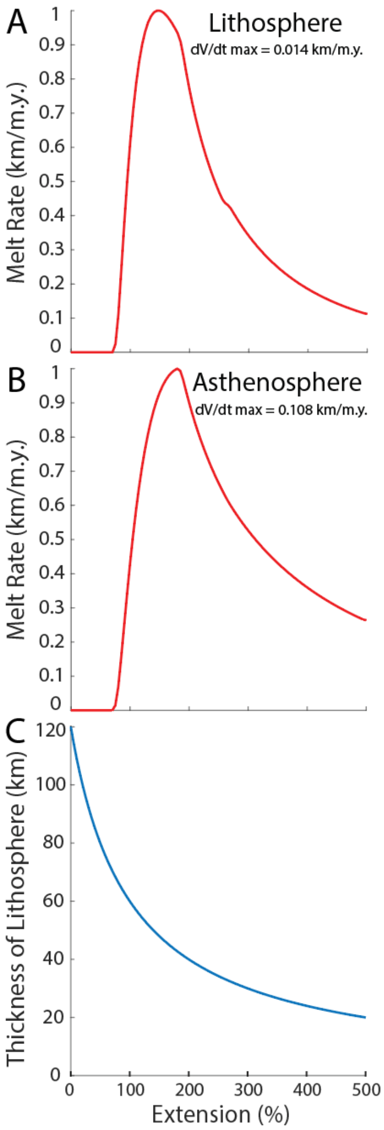

Figure 1.2. Melt production rates from dry DMM mantle in the Reference model (Fig. 1A). A) Lithosphere melting rate. B) Asthenosphere melting rate. C) Lithosphere thickness. Plots are scaled to represent melting of a mantle composed of 100% DMM and are normalized by the maximum melt production rate (dV/dt max).

similarly declines monotonically thereafter (Figure 1.3c). The decrease in melt production rates from basaltic compositions beyond the earliest stages of extension has three causes in our models. First is that the rate of lithosphere thinning, and thus the rate of decompression melting, decreases as the extensional province widens. This is a result of maintaining area balance under a constant extension rate. The second cause is that the LAB moves above the basalt liquidus after roughly 40% extension (Figure 1.3a). At this

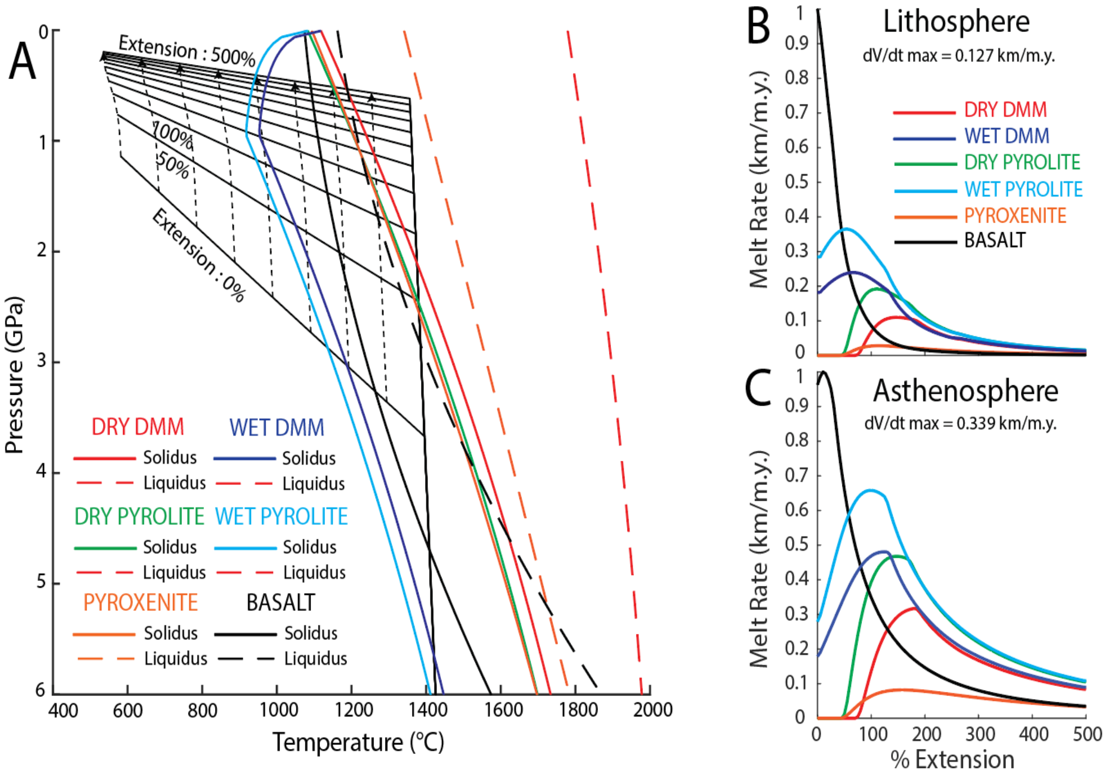

Figure 1.3. A) Pressure–temperature plot for the Reference model (same as Figure 1.1a with additional lithologies). Hydrous and anhydrous pyrolite and DMM share the same liquidus. Plots to the right show the corresponding melt production rates as a function of extension for B) the lithosphere and C) the asthenosphere. The plots are normalized by the maximum melt production rate (dV/dt max). Models simulate melting of mantle composed of either 100% dry or wet DMM, 100% dry or wet pyrolite, or mantle containing 10% pyroxenite or 10% basalt sources.

point, mafic components will have completely melted out of this portion of the mantle, limiting the duration of melt production from such compositions. The third cause is that the P-T paths of the ascending lower lithosphere and upper asthenosphere become semi-parallel to the mafic solidus at low pressures, inhibiting further partial melting (Figure 1.3a).

The LAB crosses the solidi of pyroxenite and dry pyrolite after 45% and 50% extension, respectively. Peak melt production rates from these compositions in the lithosphere are achieved soon after 115% extension (Figure 1.3b). For the asthenosphere, the corresponding amounts of extension are 160% and 150%, respectively (Figure 1.3c). Thus, if pyroxenite and dry pyrolite are present in the lithosphere or asthenosphere mantle, then they will begin melting and reach peak melting before dry DMM but after more fertile mafic components.

Hydrous sources (wet pyrolite or wet DMM) in the lower lithosphere and upper asthenosphere lie above the respective solidi prior to extension in the reference model and thus begin producing melt at the onset of rifting. Any melt generated before extension is considered extracted and is not included in the syn-rift melt calculations. Hydrous pyrolite and hydrous DMM are partially molten over a much broader range of pressures than the dry lithologies, producing melt at much shallower depths in the lithosphere

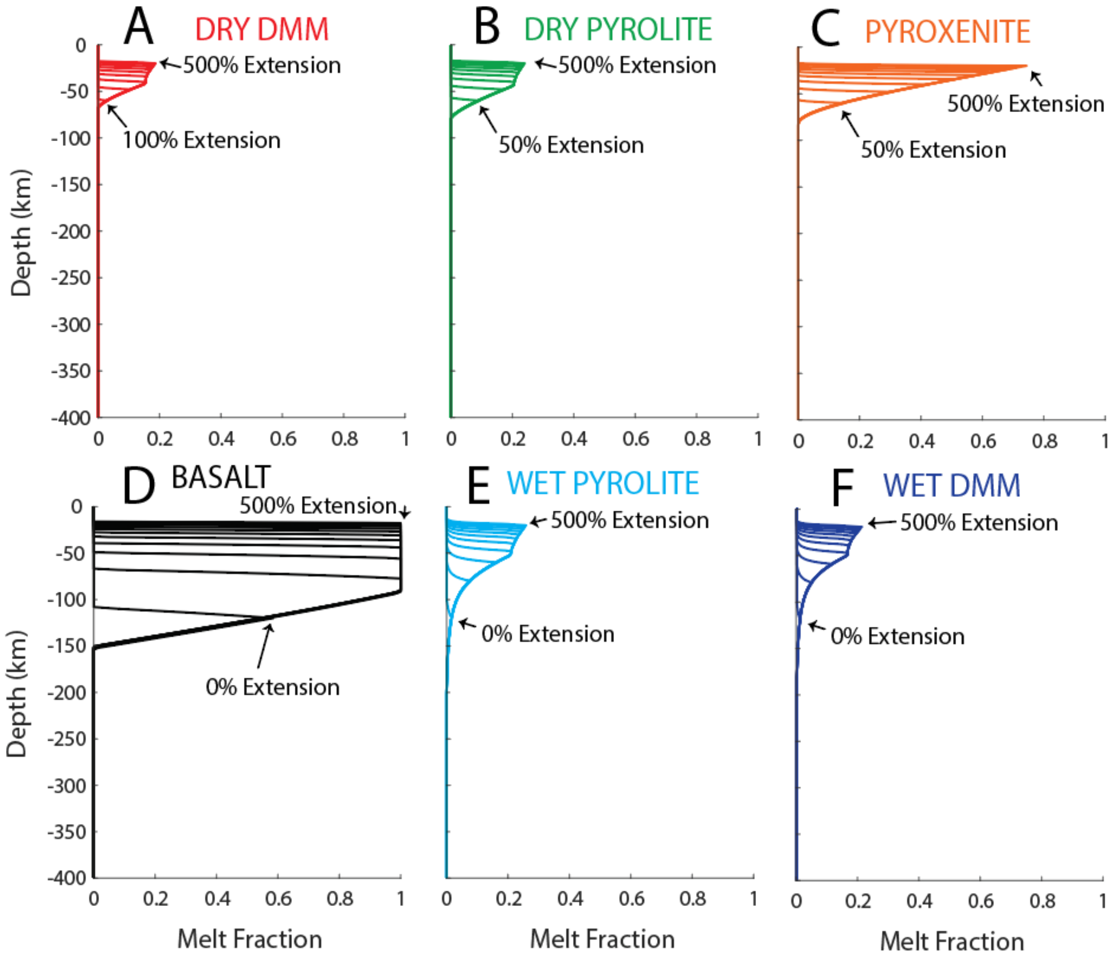

Figure 1.4. Melt fraction vs. depth for different lithologies in Reference model shown in Figure 1.3a. A) Dry DMM, B) dry pyrolite, C) pyroxenite, D) basalt, E) wet pyrolite, and F) wet DMM. The melt fraction is plotted at intervals of 50% extension from 0 – 500%. The largest melt fractions lie near the lithosphere-asthenosphere boundary.

and greater depths in the asthenosphere (Figure 1.4). For example, at the onset of extension the melt column for basalt extends from ~110 to ~150 km depth (Figure 1.4d). In comparison, the wet pyrolite and wet DMM melt columns extend from ~100 to 200 km and ~100 to 180 km, respectively (Figures 1.4e and 1.4f). In the reference model, the peak melt production rate for hydrous pyrolite occurs at 55% and 100% extension in the lithosphere and asthenosphere, respectively. The peak melt production rates for hydrous DMM in the lithosphere and asthenosphere are achieved by 70% and 130% extension (Figures 1.3b and 1.3c). The melt production rates from hydrated mantle are initially greater than those from dry mantle but become similar as extension increases. This is a result of dehydration during melting, which causes the wet solidus to approach that of dry mantle as melting progresses and water is depleted. Wet pyrolite melt production rates for the lithosphere and asthenosphere approach those of dry pyrolite after ~160% and ~170% extension, respectively. In the case of wet DMM, melt production rates for the lithosphere and asthenosphere are similar to those of dry DMM after ~175% and ~190% extension, respectively (Figures 1.3b and 1.3c). The melt calculation for hydrous mantle is based on a batch melting model, which does not capture loss of water during magma extraction. Thus, melt production rates in most continental rift systems are expected to decrease more rapidly than shown in the models if melt is extracted in a fractional manner. Exceptions may occur in arc and back-arc rift systems, where subduction continuously replenishes volatiles (Katz et al., 2003).

1.3.2. Influence of rift initial and boundary conditions on melt production rates

A series of models were developed to examine the impact of rift initial and boundary conditions on melt production. Model variables include the initial lithosphere thickness, initial crust thickness, mantle potential temperature, initial rift width, extension rate, and crust radiogenic heat production (Table 1.1). Pre-rift lithosphere thicknesses used in the models ranged from 80 km, similar to the thin modern lithosphere of the western United States or northeast Africa, to 200 km, similar to the thick lithosphere of cratons (Steinberger & Becker, 2018). Pre-rift model crust thicknesses ranged from 10 km, similar to the global minimum for continental crust (Szwillus et al., 2019), to 60 km, similar to the thick crust underlying the Himalayas (Gilligan et al., 2015). The range in mantle potential temperatures (1300–1400 °C) is consistent with the range of estimated mantle potential temperatures underlying global mid-ocean ridges that are not in close proximity to a hotspot (Lee et al., 2009). Although higher mantle temperatures are common in many mantle plumes (e.g., Rooney et al., 2012), our models are intended to capture scenarios most representative of continental rift systems. Thus, the mantle temperatures in our warmest models are elevated compared to the global average but are not hot compared to many mantle plumes. Initial rift widths ranged from 50–1,000 km, similar to rifts ranging from the narrow Malawi rift (Laó-Dávila et al., 2015) to the wide WARS (Huerta & Harry, 2007). Modeled extension rates were as low as 1 mm yr^{-1}, similar to those observed from the Rio Grande Rift, and as high as 20 mm yr^{-1}, similar to those of the Afar Rift (Tetreault & Buiter, 2018). Surface radiogenic heat production rates ranged from 0 to 10×10^{-6} W m^{-3}. These are consistent with the range of global heat production rates for most igneous rocks (Hasterok & Webb, 2017). The amount of extension required before melting begins and before peak melt production rates are achieved are found to be little influenced by variations in the model initial rift width, extension rate, crustal radiogenic heat production, and initial crustal thickness under the range of conditions examined, and so are not discussed further here (Appendix B1). Conversely, the initial lithosphere thickness and thermal structure of the mantle (in addition to its composition) greatly influence the magmatic history of the rift, as discussed below (Table B1.1).

In general, higher mantle potential temperatures (T_p) promote larger extents of melting and a thicker partial melt column that extends shallower into the lithosphere and deeper into the asthenosphere. As expected, this leads to greater melt volumes at elevated mantle temperatures (Figures 1.5 and 1.6). An exception occurs at very high temperatures, which may cause the mantle to be unable to preserve the most fertile lithologies. For example, basaltic components in the mantle produce similar or slightly less syn-rift melt from both the lithosphere and asthenosphere at breakup in the hot model (T_p =

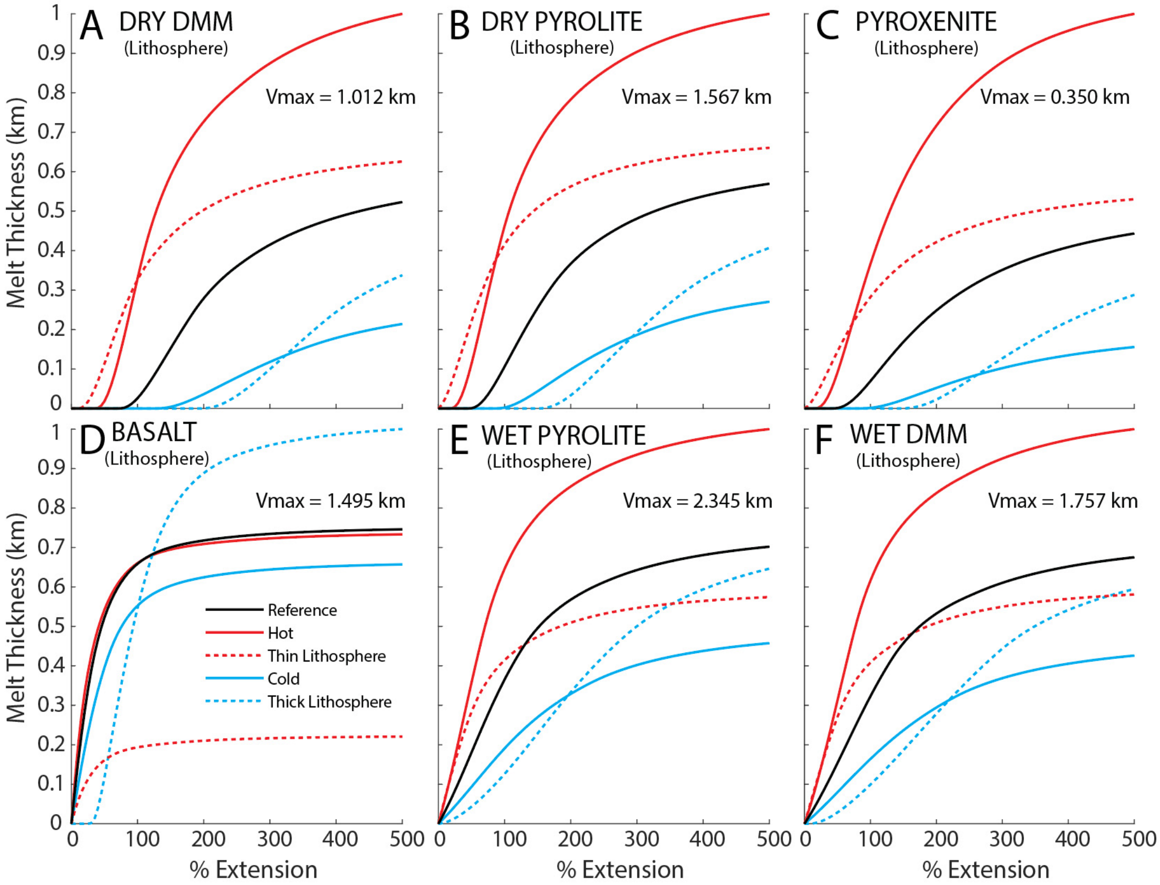

Figure 1.5. Total melt production (thicknesses) for different candidate source rock compositions within the lithosphere assuming different pre-rift mantle temperatures and lithosphere thicknesses (Table 1.1). The plots are normalized by the maximum thickness (Vmax).

1400 °C) than in the reference model (T_p = 1350 °C). This is because a pre-rift mantle lying above the basalt solidus is unable to fully sequester basaltic compositions and thus retains only the most refractory components.

Generally, a hotter mantle requires less decompression and thus less extension before the onset of melting (Figures 1.7 and 1.8, solid lines). For example, dry DMM begins melting in both the lithosphere and asthenosphere when extension reaches 40% in the hot model (T_p = 1400 °C), compared to 70% extension in the cooler reference model (T_p = 1350 °C), and 130% in the cold model (T_p = 1300 °C) (Figures 1.7a and 1.8a). Similarly, if the mantle is hot (T_p = 1400 °C) then relatively fertile (in comparison to dry DMM) pyrolite (Figures 1.7b and 1.8b) and pyroxenite (Figures 1.7c and 1.8c) in the lowermost lithosphere

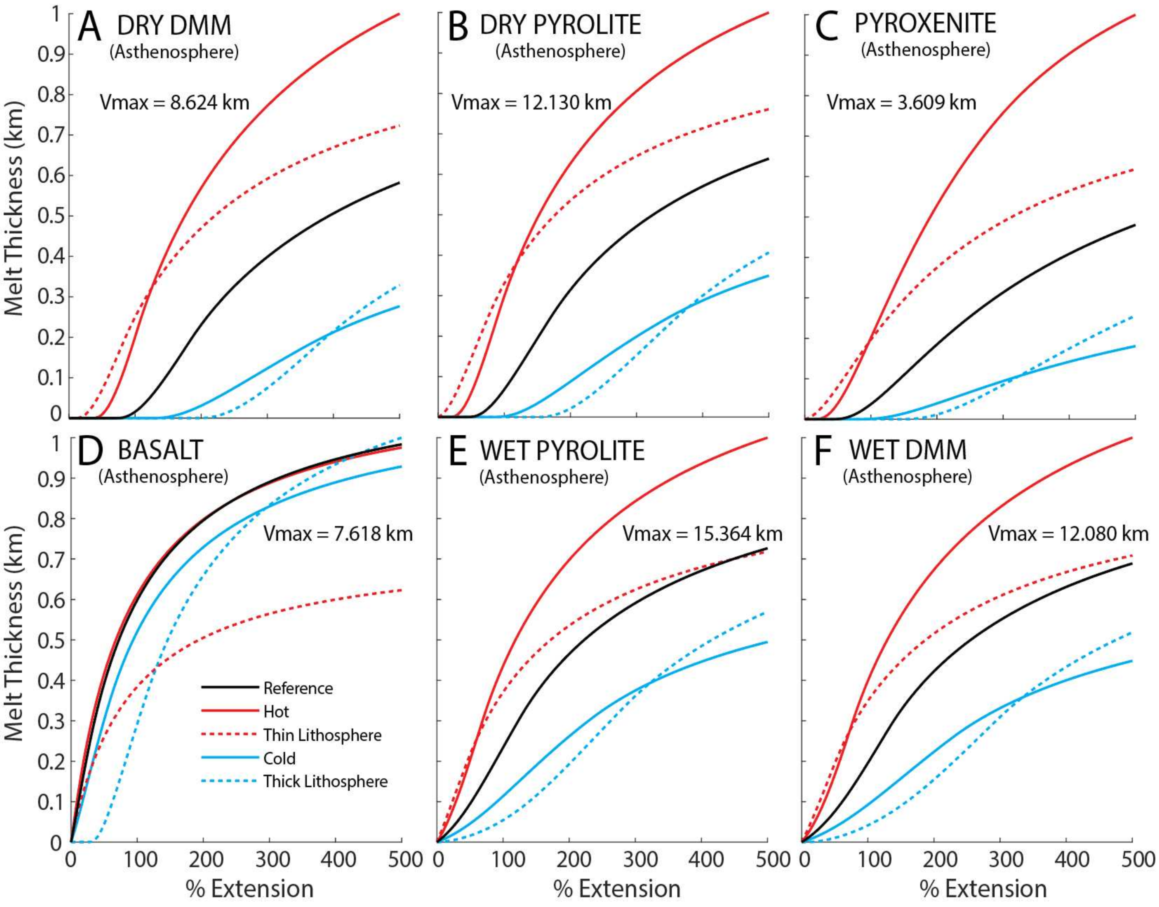

Figure 1.6. Total melt production (thicknesses) for different candidate source rock compositions within the asthenosphere assuming different pre-rift mantle temperatures and lithosphere thicknesses (Table 1.1). The plots are normalized by the maximum thickness (Vmax).

or uppermost asthenosphere will begin to produce melt by 20% and 15% extension, respectively, compared to 50% and 45% extension for the relatively cooler reference model. If basalt (Figures 1.7d and 1.8d), hydrous pyrolite (Figures 1.7e and 1.8e), or hydrous DMM (Figures 1.7f and 1.8f) are present in the lithosphere or asthenosphere then they will begin melting at the onset of extension for all modeled mantle potential temperatures with initial lithosphere thicknesses of ≤120 km, even at mantle potential temperatures as low as 1300 °C.

Peak melt production rates are similarly achieved at lower amounts of extension for all lithologies if the mantle temperature is elevated (Figures 1.7 and 1.8). For example, in the reference model (T_p = 1350 °C) dry DMM reaches peak melt production rates in the lithosphere and asthenosphere by 150% and 185%

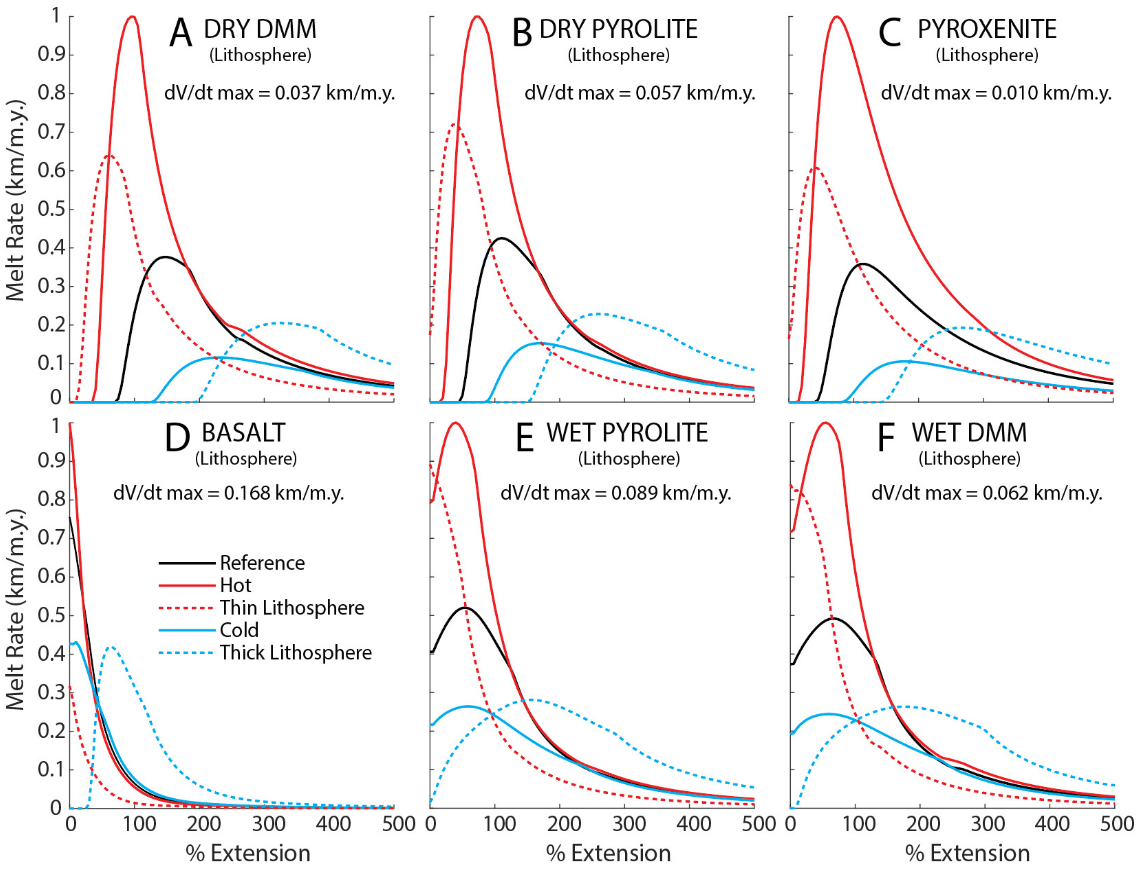

Figure 1.7. Syn-rift melt production rates for different candidate source rock compositions within the lithosphere assuming different pre-rift mantle temperatures and lithosphere thicknesses. Models are similar to the Reference Model in all other regards (Table 1.1). Solid lines compare models with different mantle potential temperatures (blue, T_p = 1300 °C; black, T_p = 1350 °C; red, T_p = 1400 °C;). Dashed lines compare models with different pre-rift lithosphere thickness (red, 80 km; black, 120 km; blue, 200 km). The plots are normalized by the maximum melt production rate (dV/dt max).

extension, respectively. In the hot model with T_p = 1400 °C dry DMM achieves peak melting in the lithosphere and asthenosphere at 100% and 105% extension. If the mantle temperatures are lower (T_p = 1300 °C) peak melting requires 235% and 290% extension.

The thicker the pre-rift lithosphere, generally, the more extension required before the onset of melting (Figures 1.7 and 1.8). For example, in the reference model with pre-rift lithosphere thickness of 120 km, dry DMM, dry pyrolite, pyroxenite, basalt, and wet DMM in the lithosphere and asthenosphere begin melting after 75%, 50%, 45%, 0%, and 0% extension, respectively. If the pre-rift lithosphere is as thick as 200 km, the lithosphere must undergo significantly more extension before melting begins (200%,

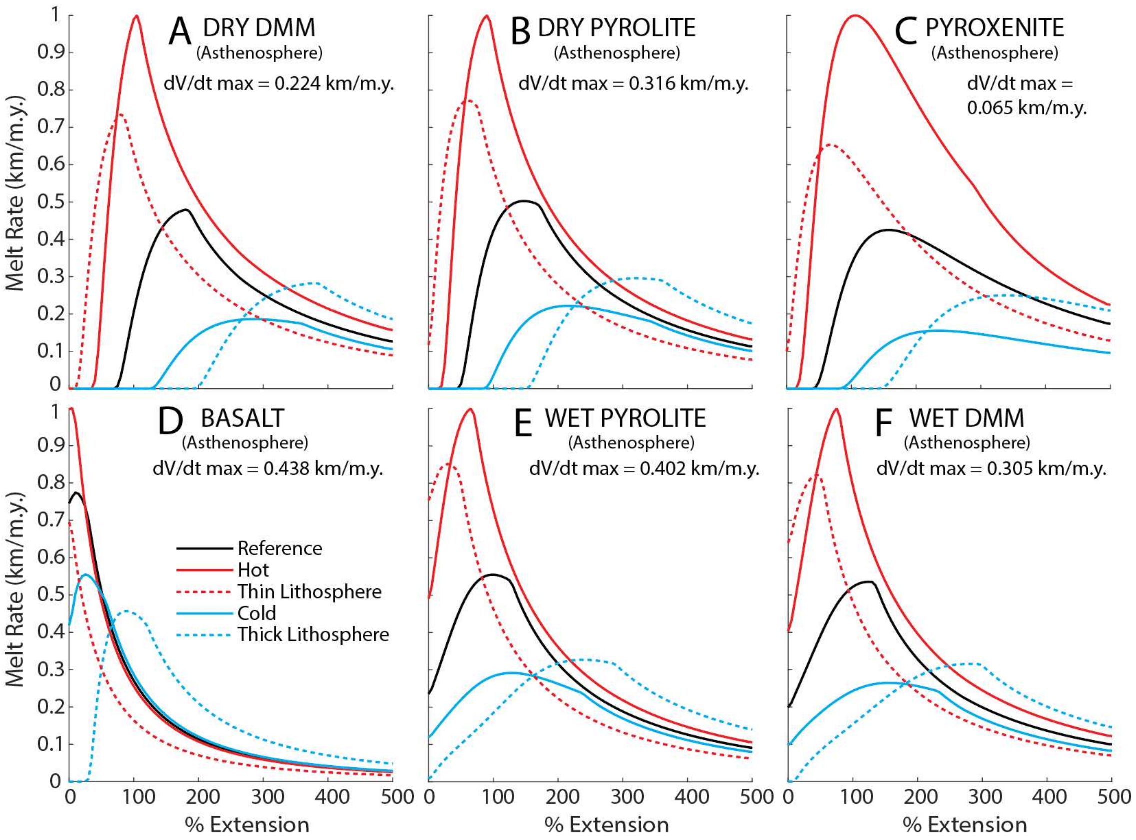

Figure 1.8. Syn-rift melt production rates for different candidate source rock compositions within the asthenosphere assuming different pre-rift mantle temperatures and lithosphere thicknesses. Models are similar to the Reference Model in all other regards (Table 1.1). Solid lines compare models with different mantle potential temperatures (blue, T_p = 1300 °C; black, T_p = 1350 °C; red, T_p = 1400 °C;). Dashed lines compare models with different pre-rift lithosphere thickness (red, 80 km; black, 120 km; blue, 200 km). The plots are normalized by the maximum melt production rate (dV/dt max).

155%, 145%, 35%, and 10% extension, respectively). Hydrous pyrolite begins melting at the onset of extension in all cases, even with very thick pre-rift lithosphere (200 km).

The greater the initial lithosphere thickness the more extension required to reach peak melt production rates (Figures 1.7 and 1.8). For example, in the reference model (120 km) peak melt production rates from dry DMM are achieved prior to 150% extension for lithosphere melts and 185% extension for asthenosphere melts. In contrast, the model with a 200 km thick pre-rift lithosphere requires 330% and 385% extension to reach peak melt production rates in the lithosphere and asthenosphere, respectively.

In all models, wet pyrolite and wet DMM dehydrate as a result of melting and the melt being extracted. Thus, melt production rates of hydrous mantle in the lithosphere and asthenosphere approach those of dry mantle as extension and associated decompression melting increase (Figures 1.9 and 1.10). Greater mantle temperatures promote dehydration at lower amounts of extension. For example, in the reference model (T_p = 1350 °C) the melt production rates from wet pyrolite in the lithosphere and asthenosphere match those of dry pyrolite by ~165% and ~170% extension, respectively. However, in the hot model (T_p = 1400 °C) the melt production rates match after ~90% and ~95% extension, respectively.

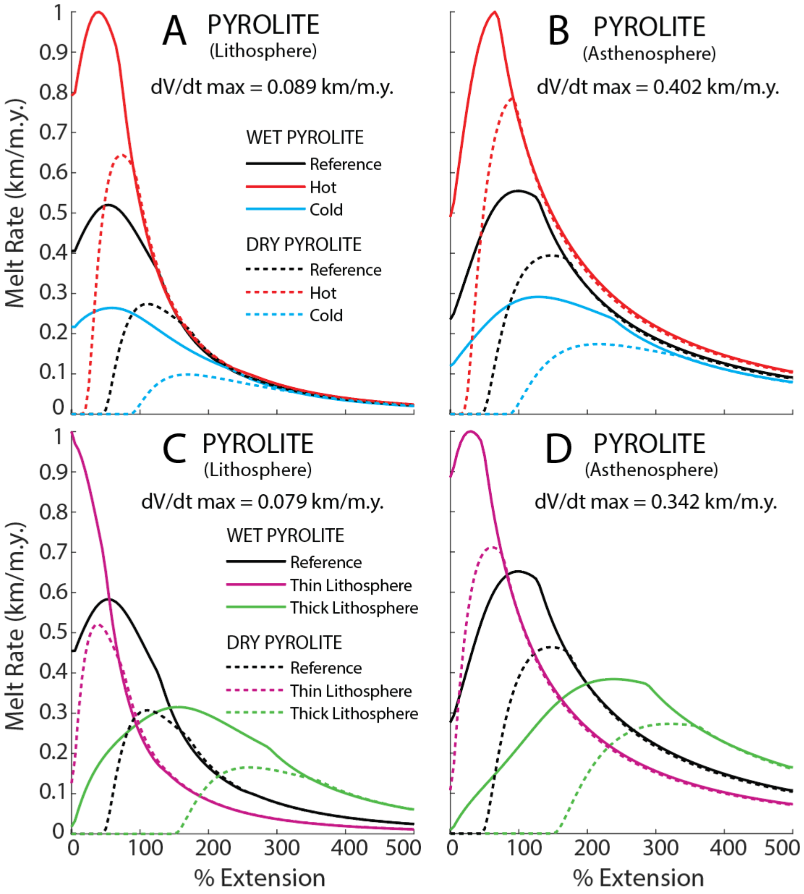

Figure 1.9. Wet and dry pyrolite melt production rates vs extension. Melt production under different mantle potential temperatures shown for A) the lithosphere and B) the asthenosphere. Melt production using different pre-rift lithosphere thickness shown for C) the lithosphere and D) the asthenosphere. The mantle becomes dehydrated by early syn-rift partial melting, causing the melt production curves for wet and dry pyrolite to converge between ~70% and ~370% extension, regardless of the pre-rift thermal conditions or lithosphere thicknesses. The plots are normalized by the maximum melt production rate (dV/dt max).

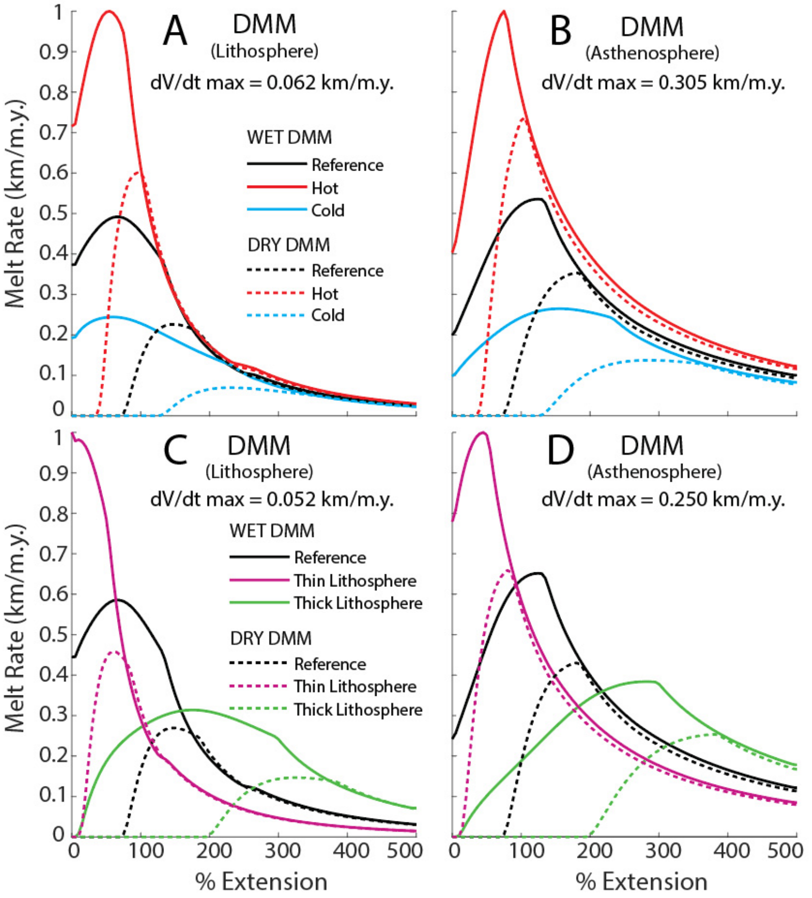

Figure 1.10. Wet and dry DMM melt production rates vs extension. Melt production under different mantle potential temperatures shown for A) the lithosphere and B) the asthenosphere. Melt production using different pre-rift lithosphere thickness shown for C) the lithosphere and D) the asthenosphere. The mantle becomes dehydrated by early syn-rift partial melting, causing the melt production curves for wet and dry pyrolite to converge between ~80% and ~380% extension, regardless of the pre-rift thermal conditions or lithosphere thicknesses. The plots are normalized by the maximum melt production rate (dV/dt max).

Similarly, thicker pre-rift lithosphere requires greater amounts of extension before the melt extraction sufficiently dehydrates the mantle to cause melt production rates to approach those of dry melting conditions.

1.4. Implications of models

The models described above show that if different mantle lithologies are present in the lithosphere and/or asthenosphere prior to extension, then upon melting they will produce distinctive temporal patterns of early syn-rift magmatism. The different lithologies considered in the models represent different petrogenetic scenarios: dry and wet DMM represent relatively depleted anhydrous and hydrous ambient mantle, dry and wet pyrolite represent more fertile primitive mantle compositions, and mafic (basalt) and fertile ultramafic (MIX1G pyroxenite) lithologies represent various fusible sources. Together these lithologies represent a pre-rift lithosphere and/or asthenosphere (ambient) mantle that may be pervasively hydrated, intruded, or entirely replaced by chemically distinct plume material. This pre-rift mantle might contain a network of mafic and ultramafic dikes, sills, veins, slab remnants, and intrusive bodies of varying ages and size, depending on the timing and nature of any previous metasomatism, magmatism, or subduction (e.g., Aviado et al., 2015; Panter et al., 2018; Pilet et al., 2008; Rooney, 2020). If all these lithologies are present, the models shown here indicate that the earliest syn-rift magmas will come from hydrous lithologies and compositionally fertile mafic lithologies such as eclogite. With continued extension, this will be followed by melting of relatively fertile dry ultramafic rocks, such as pyroxenite and primitive mantle compositions, and finally by melting of more depleted ambient mantle (DMM). As extension progresses the more fusible components melt completely and are consumed, causing MORB-like ambient mantle melts to become dominant (unless a mantle plume is present).

Mafic lithologies sequestered in the lowermost lithosphere or uppermost asthenosphere begin melting at the onset of extension with peak melting rates occurring by 30% extension in most cases (Figures 1.7d and 1.8d). Mafic sources in the lower lithosphere and upper asthenosphere are consumed during the early stages of extension (by 50% extension in the reference model). Melt production rates from these sources decrease rapidly thereafter. Thus, mafic lithologies primarily contribute to early syn-rift magmatism and become of lesser importance as extension progresses. An exception to the general tendency of mafic sources to begin melting at the onset of extension occurs if the lithosphere is very thick, as would be typical of cratons. For example, if the pre-rift lithosphere is 200 km thick, the onset of melting of basaltic compositions in the mantle does not occur until after ~35% extension is achieved and peak melt production rates for the lithosphere and asthenosphere are not achieved until 65% and 95% extension, respectively (Figures 1.7d and 1.8d).

Hydrated lithosphere or asthenosphere mantle (hydrous pyrolite or hydrous DMM in the models) begins melting at the onset of extension and reaches peak melt production rates after 40%–70% and 65%–160% extension, respectively, in most cases (Figures 1.7e, 1.7f, 1.8e, and 1.8f). The models show that melt production from hydrous mantle beneath continental rift zones is transient. The presence of volatiles and/or hydrous fluids in the lithosphere or asthenosphere enhances melt production during the early stages of extension, but melt extraction causes the source rocks to rapidly dehydrate. The enhanced melt production rates decrease accordingly, ultimately approaching those of anhydrous mantle. Like mafic sources, the amount of extension required to reach peak melt production rates of hydrous sources in the lithosphere and asthenosphere increases if the lithosphere is very thick (as is the case for cratons). If the pre-rift lithosphere is 200 km thick, peak melt production rates in the lithosphere and asthenosphere are not achieved until after 160%–180% and 245%–285% extension, respectively.

Relatively fertile ultramafic lithologies in the upper mantle (dry pyrolite and pyroxenite) do not begin melting until after the onset of melting of hydrous sources and/or peak melt production rates are achieved from any mafic components. In the reference model, dry pyrolite (representing primitive upper mantle) and pyroxenite begin melting after 50% and 45% extension, respectively. Dry pyrolite in the lithosphere and asthenosphere reaches peak melt production rates after 115% and 150% extension, respectively. Pyroxenite reaches peak melt production rates after similar amounts of extension (115% for the lithosphere and 160% for the asthenosphere). If the lithosphere is very thick, melting of primitive upper mantle compositions does not begin until after 155% extension and peak melt production rates from the lithosphere and asthenosphere are not achieved until after 265% and 325% extension, respectively (Figures 1.7b and 1.8b). Melt production from pyroxenite in the lithosphere and asthenosphere is similarly inhibited by thicker pre-rift lithosphere, with the onset of melting in the thick model not occurring until 145% extension and peak melt production rates not occurring until after 270% and 345%, respectively (Figures 1.7c and 1.8c).

The last lithology to begin melting in all models is dry DMM (representing anhydrous depleted upper mantle). In the reference model dry DMM begins melting after 75% extension and reaches peak lithosphere and asthenosphere melt production rates after 150% and 185% extension, respectively (Figures 1.7a and 1.8a). By 200% extension in this model, dry DMM at the base of the lithosphere has achieved a melt fraction of 15%. Melting DMM upper mantle beyond ca. 15% produces MORB-like tholeiites (Kushiro, 2001). Thus, as extension approaches ca. 200%, MORB-like tholeiitic magmas derived from the rising ambient asthenosphere become progressively more abundant. At the same time, melt production from more fertile compositions in the lithosphere and asthenosphere decrease as those components are consumed or cool below the solidus. The outcome is that MORB-like compositions become progressively more dominant with time.

The models shown here display a general decline in melt production across all lithologies as extension increases. This is partly due to cooling of the lithospheric mantle as extension proceeds, partly due in some cases to consumption of the fertile components by melting, and partly due to the model parameterization. The models shown here extend at constant rates. Under this condition, area balance requires that the rate of thinning decreases as the extensional province widens. This causes the rate of decompression, and thus the rate of melt production, to decrease with continued extension. However, several fertile lithologies show decreases in melt production during the early stages of extension that do not correlate with the progressive decrease in thinning rate and appear to be independent of the model geometric parameterization. The decline in melt production from fertile lithologies during the early stages of extension (<100%) is primarily due to (a) consumption of the fertile lithologies through melting and (b) cooling of the upper mantle as it rises below the rift axis. We note that cooling of the upper mantle will be more pronounced than shown in the models if latent heat of melting is considered.

The melting sequence described above is consistent with petrogenic models that have been suggested for several continental rifts. In the EARS, there is a general transition from alkaline silica-undersaturated magmas erupted during incipient rifting to silica-saturated magmas erupted during more mature rifting (Lippard & Truckle, 1978; MacDonald et al., 2001; Rooney, 2020). This transition has been attributed to a change in melt source with the earliest magmas resulting from melting of fertile lithospheric metasomes and later magmas increasingly produced from melting of dry lherzolite asthenosphere (Rooney, 2020). A similar melting sequence is proposed for the Rio Grande Rift, where isotopic and trace element signatures of syn-rift magmas suggest early syn-rift melting of fertile lithosphere sources that shifts to later melting of ambient asthenosphere as extension increases (McMillan et al., 2000). Petrogenic models of the WARS have also called for the early melting of metasomes and fertile lithologies such as eclogite, pyroxenite, and amphibole-rich sources to explain spatiotemporal changes in basalt chemistry (e.g., Aviado et al., 2015; Panter et al., 2018).

The models shown here emphasize that pre-rift lithosphere and asthenosphere P-T conditions limit the mantle's ability to host fertile lithologies. For example, if we assume a pre-rift lithosphere thickness of 120 km and a mantle potential temperature of 1350 °C (the reference model) then the LAB lies in the super-solidus field for basalt prior to extension (Figure 1.3a). The lithosphere is too hot to fully sequester basaltic compositions. Whether caused by a hot asthenosphere, a mantle plume, or by a thin lithosphere, relatively high pre-rift LAB temperatures inhibit freezing and storage of fertile lithologies in the uppermost mantle. Cooler pre-rift LAB temperatures promote preservation of fertile lithologies, making them available as sources for early syn-rift magmatism. A thick pre-rift lithosphere or craton generally results in a cooler geotherm, and thus creates both volume and P-T conditions favorable for preservation of fusible material in the pre-rift lithosphere mantle.

1.5. Conclusions

The composition and timing of magma produced by decompression melting of the mantle during rifting varies systematically with source rock composition and depth. The most fusible source rocks (e.g., mafic or hydrous components) in the lowermost lithosphere and uppermost asthenosphere begin melting near the onset of extension and are quickly consumed or rapidly become dehydrated (e.g., hydrous sources), thus reaching peak melt production rates at low levels of extension. This leads to the most fusible source rocks contributing most to early syn-rift magmatism and the least fusible source rocks contributing primarily to later magmatism. The relative timing in which the various source rock lithologies contribute most to syn-rift magmatism are consistent regardless of mantle potential temperature or lithospheric thickness. Therefore, each lithology in a highly metasomatized mantle consisting of ambient mantle (depleted MORB-source peridotite) intermixed with comparatively fertile primitive mantle, hydrous, ultramafic, and mafic components will sequentially dominate syn-rift magmatism. Melts derived from mafic components dominate the earliest syn-rift magmatism, followed in turn by the melting of hydrous components, fertile ultramafic components and primitive mantle, and ultimately ambient mantle (Figures 1.11a–1.11d).

The parameters with the greatest effect on the amount of extension required prior to the onset of melting and prior to peak melt production are the mantle composition and temperature and the pre-rift lithosphere thickness. These interact to produce a progressive sequence of melting that is consistent across a broad range of rift conditions (Table 1.1):

1. Mafic source rocks in the lowermost lithosphere and uppermost asthenosphere begin to melt between 0% and 35% extension and reach peak melt production rates in the lithosphere between 0% and 65% extension and in the asthenosphere between 0% and 95% extension. Mafic components in the mantle are the first to reach peak melt production rates.

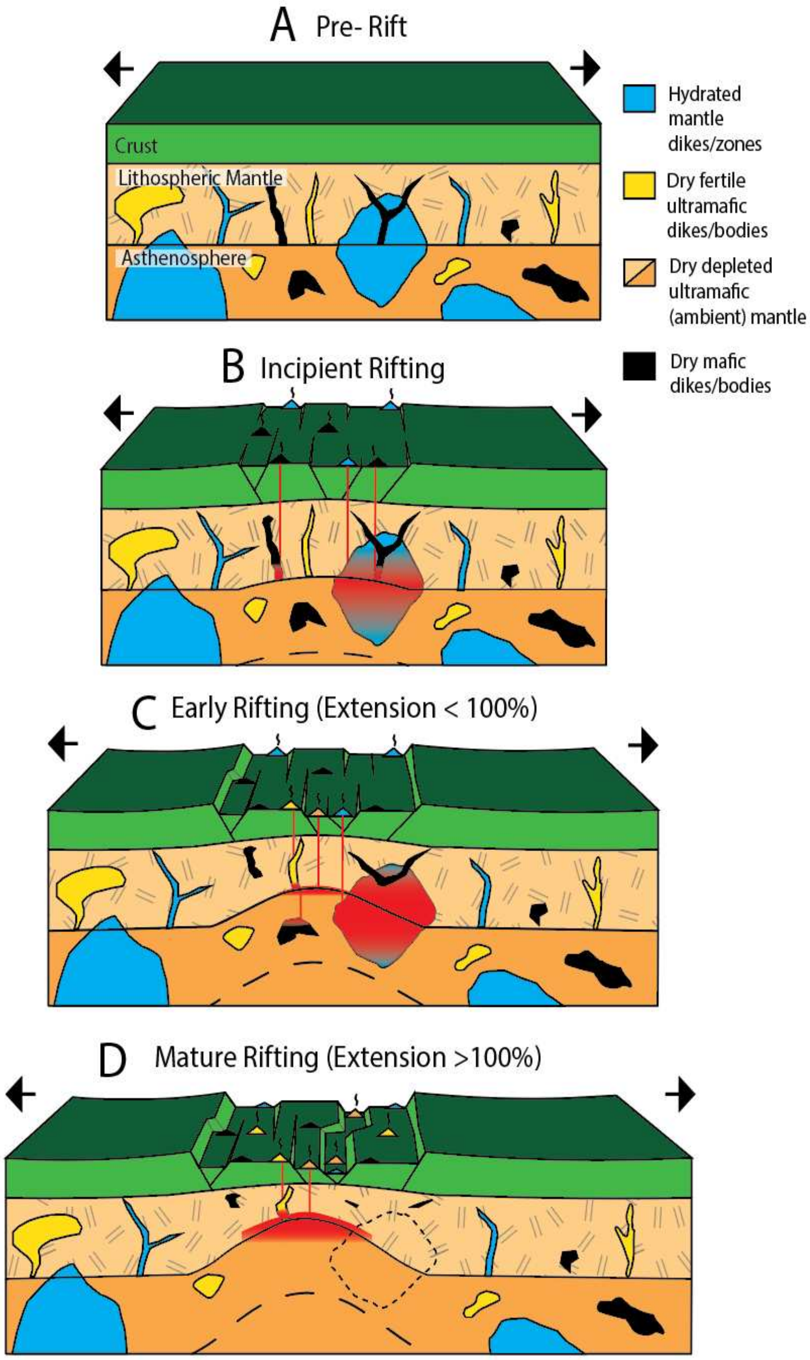

Figure 1.11. Conceptual model of early syn-rift magmatism showing progressive melting of different mantle sources. Model evolution follows the Reference model (Table 1.1, Figure 1.3a). A) Pre-rift. Metasomatized and compositionally heterogeneous ambient mantle (represented here by DMM or depleted MORB mantle) containing hydrated zones and dikes, and fertile ultramafic (e.g., pyroxenite), and mafic (e.g., basalt) intrusions. B) Incipient rifting leads to melting of hydrated mantle and mafic source rocks. The mafic sources reach peak melting rates during the earliest stages of extension. C) Early rifting (< 100% extension). Onset of melting of both fertile dry ultramafic source rocks and ambient mantle. The hydrous sources reach peak melting rates. Mafic source rocks begin depleting. D) Mature rifting (> 100% extension). Prior melt extraction has dehydrated the mantle, causing hydrated regions to converge toward dry mantle melting behavior. Mafic source rocks in the lithosphere and upper asthenosphere have largely been consumed during the earlier phase of rifting. Dry fertile ultramafic lithologies reach peak melting rates. The depleted ambient mantle (DMM) is the last lithology to reach peak melting rates. Red coloring indicates melting, with intensity of shading indicating the extent of melting. The thin dashed line in (D) shows the dehydration of the hydrous source. Volcanoes (triangles) are colored to indicate source. The area below the dashed line at the bottom of (B – D) is deep mantle rising to fill the area beneath the rift. This figure was inspired by the conceptual models of Aviado et al. (2015) and Rooney (2020).

2. Hydrous peridotite, if present in the lowermost lithosphere and uppermost asthenosphere, begins to melt at the onset of extension and reaches peak melt production rates in the lithosphere between 0% and 180% extension and in the asthenosphere between 30% and 285% extension. Melting quickly dehydrates the mantle, shifting the melting behavior toward that of dry peridotite. This causes a rapid decline in melt production after an initial outburst. Hydrous ultramafic components in the mantle reach peak melt production rates after mafic components but before dry ultramafic components.
3. Dry ultramafic source rocks that are fertile in comparison to DMM (including pyroxenite and primitive mantle in our models) in the lowermost lithosphere and uppermost asthenosphere begin to melt between 0% and 155% extension. These fertile ultramafic lithologies reach peak melt production rates in the lithosphere between 40% and 270% extension and in the asthenosphere between 65% and 345% extension. Dry fertile ultramafic components in the mantle reach peak melt production rates after hydrous and mafic components.
4. Melting of ambient mantle (DMM) begins between 10% and 200% extension and reaches peak melt production rates in the lithosphere between 60% and 330% extension and in the asthenosphere between 85% and 385% extension. DMM mantle reaches peak melt production rates after mafic, hydrous, and dry fertile ultramafic mantle components.
5. The ability to preserve fertile lithologies in the mantle depends on how close the P-T conditions in the pre-rift upper mantle lie to the solidi of the fertile lithologies. A cool, thick lithosphere best promotes preservation of fertile lithologies in the upper mantle, whereas a thin, warm lithosphere is less able to host such compositions.

1.6. Data Availability Statement

The MATLAB code MELT1D developed for this study as well as the model input and output files are available at https://doi.org/10.5281/zenodo.7930969.

Appendix A1

A new MATLAB program, MELT1D, was developed to estimate melt production during rifting. MELT1D uses a Lagrangian formulation to compute the pressure-temperature (P-T) profile at specific nodes in the lithosphere and asthenosphere assuming a 1D column of lithosphere is extended at a constant rate with asthenosphere rising vertically to fill the gap. In the lithosphere the depth to a particle initially at depth z_0 prior to rifting is

$$z(t) = \frac{z_0}{\left(1 + \frac{U_x t}{L_0}\right)}, \qquad 0 < z < z_L \tag{A1}$$

where z_L is the depth to the base of the lithosphere, U_x is the extension rate, L_0 is the initial rift width, and *t* is time elapsed since the onset of extension. The temperature *T* in the lithosphere is determined from the one-dimensional heat equation:

$$\rho C_p \frac{dT}{dt} = A + \nabla \cdot k \nabla T + \rho C_p U_z G_a, \qquad 0 < z < z_L \tag{A2}$$

where *k* is thermal conductivity, C_p is specific heat, ρ is density, *A* is heat production, U_z is the ascension rate, and G_a is the mantle adiabatic temperature gradient. The ascension rate is given by the time derivative of equation (A1):

$$U_z(t) = \frac{-z_0 \frac{U_x}{L_0}}{\left(1 + \frac{U_x t}{L_0}\right)^2}, \qquad 0 < z < z_L. \tag{A3}$$

An exponential decrease in heat production with depth is assumed for the crust and no heat production is assumed for the mantle:

$$A(z) = A_0 e^{-\frac{z}{D}}, \qquad 0 < z < z_m \tag{A4}$$

$$A(z) = 0, \qquad z_m \leq z < z_L \tag{A5}$$

where z_m is depth to the base of crust, A_0 is the surface heat production, and D is the heat production decay constant. Boundary conditions include a 0 °C surface temperature and adiabatic temperature at the base of the lithosphere. Pre-extension temperatures in the lithosphere are calculated from equation (A2) assuming $U_z = 0$ and $dT/dz = 0$. Equation (A2) is solved at $t > 0$ using the fourth order Runge-Kutta method (Harry & Leeman, 1995). The temperature in the asthenosphere is prescribed to be adiabatic:

$$T(z) = T_p + G_a z, \qquad z_L \leq z \leq z_a \tag{A6}$$

where T_p is the mantle potential temperature. The pressure P is calculated using

$$P(z) = g \int_0^z \rho_r(z) * \big(1 - \alpha * T(z)\big) dz \tag{A7}$$

where g is the acceleration of gravity, α is the thermal expansion coefficient, and ρ_r is the reference density measured at 0 °C.

MELT1D requires the user to specify the fractional abundance of each lithology present in the mantle prior to the onset of extension. The melt fraction for each lithology at every depth node is evaluated at each time step using the P-T profiles calculated from equations (A2), (A6) and (A7). The difference in melt fraction between time steps is then integrated over depth and scaled by the fractional abundance of each lithology to find the volume of melt produced by decompression melting during each time step. We refer to this as the incremental melt volume. The sum of the incremental melt volumes is the total melt volume produced from each lithology during rifting. The melt production rate for each lithology is calculated by dividing the respective incremental melt volumes by the time step size.

MELT1D includes melting relations for several peridotite rocks, including dry harzburgite, dry garnet peridotite, dry/wet DMM, dry/wet lherzolite, and dry/wet pyrolite (Brown & Lesher, 2016; Katz et al., 2003; McKenzie & Bickle, 1988); three dry pyroxenite compositions (OBS1, G2, and MIX1G of Brown & Lesher, 2016; Kimura & Kawabata, 2015; Pertermann & Hirschmann, 2003); and dry basalt (Harry & Leeman, 1995). The solidus, liquidus, and melting functions for dry basalt and two dry pyroxenite compositions (G2 and MIX1G) follow the general form:

$$T_s(P) = C_1 P^2 + C_2 P + C_3 \tag{A8}$$

$$T_l(P) = C_4 P^2 + C_5 P + C_6 \tag{A9}$$

$$T_n(T,P) = \frac{T - T_s(P)}{T_l(P) - T_s(P)} \tag{A10}$$

$$F(T,P) = C_7 T_n^m(T,P) + C_8 T_n(T,P) + C_9 \tag{A11}$$

where T_s is the solidus, T_l is the liquidus, T_n is the homologous temperature, F is the melt fraction, and C_1-C_9 and m are constants that vary with lithology (Table A1.1). Polynomial functions for the solidus, liquidus, and melting function for dry basalt have not been published, so we determined them by fitting second order polynomials to the piecewise solidus and liquidus curves and experimental melt fraction data in Figure 10 of Harry and Leeman (1995).

The melting functions for dry garnet peridotite are parameterized differently than in equations (A8 – A11). Following McKenzie and Bickle (1988), the melt fraction is calculated using a dimensionless temperature T_d:

$$T_d(T,P) = \frac{T - \frac{1}{2}\left(T_l(P) + T_s(P)\right)}{T_l(P) - T_s(P)} \tag{A12}$$

$$F(T,P) = 0.5 + T_d(T,P) + \left(T_d^2(T,P) - 0.25\right)\left(0.4256 + 2.988 * T_d(T,P)\right). \tag{A13}$$

The liquidus temperature is:

$$T_l(P) = 1736.2 + 4.343 * P + 180 * \tan^{-1}\left(\frac{P}{2.2169}\right). \tag{A14}$$

The solidus is determined from its pressure dependence (McKenzie & Bickle, 1988):

$$P = \frac{T_s - 1100}{136} + 4.968 * 10^{-4} e^{\left(1.2*10^{-2}(T_s - 1100)\right)}. \tag{A15}$$

Here, pressure is calculated from equation (A7) and the solidus temperature is then solved by finding the root of equation (A15) using the fzero algorithm in MATLAB.

The bulk rock solidus and liquidus for dry lherzolite, dry pyrolite, dry DMM, and dry harzburgite follow equations (A8 and A9), respectively (Table A1.1). Following Katz et al. (2003) and Brown and Lesher (2016), piecewise functions are used to describe the melt fraction for these lithologies in order to account for depletion of clinopyroxene at large melt fractions. If $T_s(P) < T(P) < T_l(P)$, then we first compute the temperature at which clinopyroxene is completely melted, $T_{cpx\text{-}out}$. $T_{cpx\text{-}out}$ depends on the bulk rock melt fraction when clinopyroxene is consumed, $F_{cpx\text{-}out}$, and a model parameter $T_{l\text{-}cpx}$ that is analogous to the liquidus temperature of the bulk rock if clinopyroxene were not melted out:

$$T_{cpx-out}(P) = F_{cpx-out}^{\frac{1}{1.5}}(P) * \left(T_{l-cpx}(P) - T_s(P)\right) + T_s(P) \tag{A16}$$

$$T_{l-cpx}(P) = 1475 + 80 * P - 3.2P^2. \tag{A17}$$

$F_{cpx\text{-}out}$ was parameterized from experimental melt results for dry pyrolite, dry DMM, and dry harzburgite and is formulated as piecewise polynomial functions of pressure that follow the general form (Brown & Lesher, 2016):

$$F_{cpx-out}(P) = \frac{r_1P^2 + r_2P + r_3}{100} \tag{A18}$$

where r_1 - r_3 are coefficients that vary for lithology and pressure (Table A1.2). $F_{cpx\text{-}out}$ for dry lherzolite depends on the mass fraction of clinopyroxene initially present M_{cpx} and the clinopyroxene reaction coefficient R_{cpx}:

$$F_{cpx-out}(P) = \frac{M_{cpx}}{R_{cpx}(P)} \tag{A19}$$

$$R_{cpx}(P) = r_4 + r_5P \tag{A20}$$

where M_{cpx} = 0.15, r_3 = 0.5, and r_4 = 0.08 after Katz et al. (2003). The melting function for dry lherzolite, dry pyrolite, dry DMM, and dry harzburgite for $F \leq F_{cpx\text{-}out}$ is

$$F(T,P) = \left[\frac{T - T_s(P)}{T_{l-cpx}(P) - T_s(P)}\right]^{1.5}. \tag{A21}$$

If $F > F_{cpx\text{-}out}$ then the melt fraction is determined using

$$F(T,P) = F_{cpx-out}(P) + \left(1 - F_{cpx-out}(P)\right) * \left[\frac{T - T_{cpx-out}(P)}{T_l(P) - T_{cpx-out}(P)}\right]^{1.5}. \tag{A22}$$

The solidi, liquidi, and melting functions for wet lherzolite, wet pyrolite, and wet DMM are calculated by correcting T_s, T_l, $T_{l\text{-}cpx}$, and $T_{cpx\text{-}out}$, for the temperature decrease due to the presence of water, ΔT_{H2O} (Brown & Lesher, 2016; Katz et al., 2003):

$$T_{ws}(P) = T_s(P) - \Delta T_{H2O} \tag{A23}$$

$$T_{wl}(P) = T_l(P) - \Delta T_{H2O} \tag{A24}$$

$$T_{wl-cpx}(P) = T_{l-cpx}(P) - \Delta T_{H2O} \tag{A25}$$

$$T_{wcpx-out}(P) = T_{cpx-out}(P) - \Delta T_{H2O} \,. \tag{A26}$$

ΔT_{H2O} depends on the mass fraction of water dissolved in the melt X_{H2O}:

$$\Delta T_{H2O} = 43 * (X_{H2O})^{0.75} \,. \tag{A27}$$

X_{H2O} depends on the bulk rock water mass fraction prior to melting, $X_{bulk\text{-}H2O}$, and the distribution coefficient of water between the solid and melt D_{H2O}:

$$X_{H2O} = min\left\{\frac{X_{bulk-H2O}}{D_{H2O} + F * (1 - D_{H2O})}, X_{sat-H2O}\right\} \tag{A28}$$

D_{H2O} = 0.01 for wet lherzolite (Katz et al., 2003) and D_{H2O} = 0.008 for wet pyrolite and wet DMM (Brown & Lesher, 2016). Equation (A28) requires that X_{H2O} not exceed the pressure dependent water saturation limit for melt $X_{sat\text{-}H2O}$, where

$$X_{sat-H2O} = 0.12 * P^{0.6} + 0.01 * P \,. \tag{A29}$$

For wet peridotite, equations (A21 and A22) are modified to include dependence on ΔT_{H2O}. If $F \leq F_{cpx\text{-}out}$ the melt fraction is determined using

$$F(T,P) = \left[\frac{T - (T_s(P) - \Delta T_{H2O}(X_{H2O}(F,P,X_{bulk-H2O})))}{T_{l-cpx}(P) - T_s(P)}\right]^{1.5} . \tag{A30}$$

If $F > F_{cpx\text{-}out}$ then

$$\begin{aligned} F(T,P) = {} & F_{cpx-out}(P) + \left(1 - F_{cpx-out}(P)\right) \\ & * \left[\frac{T - (T_{cpx-out}(P) - \Delta T_{H2O}(X_{H2O}(F,P,X_{bulk-H2O})))}{T_l(P) - T_{cpx-out}(P)}\right]^{1.5} . \end{aligned} \tag{A31}$$

The melt fraction appears on both sides of equations (A30 and A31), which are solved using the fzero root-finding algorithm in MATLAB (Brown & Lesher, 2016; Katz et al., 2003).

MELT1D includes melting relations for the synthetic OBS1 pyroxenite of Kimura and Kawabata (2015). This pyroxenite has a solidus and liquidus of the forms given in equations (A8 and A9). The melt fraction for this composition is given by an exponential expression:

$$F(T,P) = \frac{1}{100}\left(2.2082 * e^{(-0.72*P)} * \left(\frac{T}{1000}\right)^{16.1} - 10\right). \tag{A32}$$

Table A1.1. Constants for Melt Equations

Lithology	Solidus			Liquidus			Melting Function			
	C_1	C_2	C_3	C_4	C_5	C_6	C_7	C_8	C_9	m
Dry Basalt (Leeman & Harry, 1995)	9.173	28.07	1077	12.46	42.81	1165	-0.32	1.32	0	2
Dry G2 Pyroxenite (Brown & Lesher, 2016)	0	130	920	0	114	1175	0.737	0.26	0	2
Dry MIX1G Pyroxenite (Brown & Lesher, 2016)	-3.4535	120.95	1096.8	0	73.6	1343	1	0	0	2
Dry OBS1 Pyroxenite (Kimura & Kawabata, 2015)[a]	1.2583	48.753	1098.5	1.4619	56.571	1274.9				
Dry Lherzollite (Katz et al., 2003)[b]	-5.1	132.9	1085.7	-2	45	1780				
Dry Pyrolite (Brown & Lesher, 2016)[b]	-5.1	132.9	1085.7	-2	45	1780				
Dry DMM (Brown & Lesher, 2016)[b]	-5.1	132.9	1120.7	-2	45	1780				
Dry Harzburgite (Brown & Lesher, 2016)[b]	-5.1	132.9	1147.2	-2	45	1780				
Dry Garnet Peridotite (Mckenzie & Bickle, 1988)[c]										
Wet Pyrolite (Brown & Lesher, 2016)[d]										
Wet DMM (Brown & Lesher, 2016)[d]										
Wet Lherzolite (Katz et al., 2003)[d]										

[a] OBS1 pyroxenite uses an exponential melting function.

[b] The melting function is a piecewise polynomial function dependent on the presence of clinopyroxene.

[c] Uses an exponential solidus function, trigonometric liquidus function, and the defined T_n is not used in the melting function.

[d] The melting equations are calculated by correcting the corresponding dry solidus and liquidus for the presence of water which is dependent on the pressure, melt fraction, and mass fraction of bulk water in the lithology.

Table A1.2. Constants for Determining the Melt Fraction when Clinopyroxene is Absent

Pressure (GPa)	r_1	r_2	r_3
Dry/Wet Pyrolite (Brown and Lesher, 2016)			
$P < 1$	0	0	20
$1 \leq P < 3$	0	1.5	18.5
$P \geq 3$	-0.25	8.25	0.5
Dry/Wet DMM (Brown and Lesher, 2016)			
$P < 1$	0	3.2351	11.368
$P \geq 1$	0	0	14.6031
Dry Harzburgite (Brown and Lesher, 2016)			
$P \leq 1$	0	0	3.2351
$P > 1$	0	3.2351	0

Appendix B1

In comparison to lithology, lithosphere thickness, or mantle potential temperature, variations in crust radiogenic heat production, pre-rift crust thickness, extension rates, or initial rift widths have little impact on either the amount of extension necessary to initiate melting nor the amount of extension required before peak melt production rates are achieved (Table B1.1). For example, the amount of extension required before DMM components in the mantle begin melting ranges from 10 – 195% when the model pre-rift mantle potential temperature is varied between 1300 – 1400 °C or the pre-rift lithosphere thickness is varied between 80 – 200 km. The amount of extension required to reach peak DMM melt production rates has a similarly large range, with peak DMM melt production from the lithosphere and asthenosphere occurring in these models between 60 – 325% extension and 80 – 380% extension, respectively. In contrast, the amount of extension required prior to the onset of DMM melting varies little (between 70-80%) in models where the crust radiogenic heat production, pre-rift crust thickness, extension rates, or initial rift widths are varied (Table 1.1). The amount of extension required before peak melt production rates are achieved also shows little variation in these models, with peak DMM melt production occurring between 130 – 160% extension in the lithosphere and between 175 –

190% extension in the asthenosphere. The melt production histories of these models are very similar to that of the reference model where DMM components in the mantle begin melting by 70% extension and peak melt production rates in the lithosphere and asthenosphere are achieved by 145% and 180% extension, respectively.

Crust heat generation and thickness primarily impact the temperature of the upper and middle lithosphere. These portions of the mantle remain below the solidi of the candidate lithologies throughout rifting in all models, so these model parameters have little to no effect on the modeled melt production history. However, varying the initial lithosphere thickness or mantle potential temperature has a large impact on the mantle geotherm and thus the modeled melt production histories (Figures B1.1 and B1.2).

The amount of extension necessary for the onset of melting as well as to achieve peak melt production rates from any given composition is comparable regardless of the extension rate or initial rift width (compare fast/slow, wide/thin, and reference models in Figures B1.1 and B1.2). This is due largely to the 1D formulation of the model, which prevents cooling due to horizontal heat flow. The models may thus overestimate melt production in slowly extending narrow rifts where cooling of the upwelling mantle may be pronounced.

Table B1.1. Summary Model Results

Model	Lithology	Onset of Melting (% Extension)	Timing of Peak Lithosphere Melt Production Rate (% Extension)	Peak Lithosphere Melt Production Rate (m/m.y.)	Timing of Peak Asthenosphere Melt Production Rate (% Extension)	Peak Asthenosphere Melt Production Rate (m/m.y.)
Reference	DMM	70	145	14	180	108
	Pyrolite	45	110	24	145	159
	Pyroxenite	40	115	4	160	28
	Basalt	0	0	127	10	339
	Wet Pyrolite	0	55	46	100	223

	Wet DMM	0	65	30	125	163
Hot	DMM	35	95	37	105	224
	Pyrolite	20	75	57	90	316
	Pyroxenite	15	75	10	105	65
	Basalt	0	0	168	5	438
	Wet Pyrolite	0	40	89	65	402
	Wet DMM	0	55	62	75	305
Cold	DMM	125	230	4	285	42
	Pyrolite	85	170	9	215	70
	Pyroxenite	80	180	1	235	10
	Basalt	0	10	73	25	243
	Wet Pyrolite	0	60	24	130	117
	Wet DMM	0	60	15	155	81
Thick Lithosphere	DMM	195	325	8	380	63
	Pyrolite	150	260	13	320	93
	Pyroxenite	140	265	2	340	16
	Basalt	30	65	71	90	200
	Wet Pyrolite	0	155	25	240	131
	Wet DMM	10	175	16	280	96
Thin Lithosphere	DMM	10	60	24	80	165
	Pyrolite	0	40	41	60	244
	Pyroxenite	0	40	6	65	43
	Basalt	0	0	53	0	304
	Wet Pyrolite	0	0	79	30	342
	Wet DMM	0	0	52	45	250
Fast	DMM	70	145	29	180	215
	Pyrolite	45	110	50	145	317
	Pyroxenite	40	115	7	155	56
	Basalt	0	0	254	10	678
	Wet Pyrolite	0	55	93	100	446
	Wet DMM	0	70	61	125	326

Slow	DMM	70	150	1	180	11
	Pyrolite	45	115	2	145	16
	Pyroxenite	40	115	0	160	3
	Basalt	0	0	13	10	34
	Wet Pyrolite	0	50	4	100	22
	Wet DMM	0	70	3	125	16
Narrow	DMM	70	150	58	180	431
	Pyrolite	45	115	100	145	635
	Pyroxenite	40	115	15	155	111
	Basalt	0	0	508	10	1357
	Wet Pyrolite	0	55	186	100	893
	Wet DMM	0	70	122	125	652
Wide	DMM	70	150	3	180	22
	Pyrolite	45	115	5	145	32
	Pyroxenite	40	115	1	160	6
	Basalt	0	0	25	10	68
	Wet Pyrolite	0	50	9	100	45
	Wet DMM	0	65	6	125	33
Thick Crust	DMM	70	140	16	175	110
	Pyrolite	45	105	27	140	163
	Pyroxenite	35	110	4	150	29
	Basalt	0	0	139	10	347
	Wet Pyrolite	0	50	52	95	228
	Wet DMM	0	60	34	120	167
Thin Crust	DMM	80	160	12	190	104
	Pyrolite	50	120	20	155	153
	Pyroxenite	45	125	3	170	27
	Basalt	0	0	105	15	328
	Wet Pyrolite	0	60	38	105	215
	Wet DMM	0	75	25	135	157
	DMM	70	130	15	180	107

High Crustal Heat Generation	Pyrolite	45	95	30	145	158
	Pyroxenite	40	100	4	155	28
	Basalt	0	0	178	10	340
	Wet Pyrolite	0	45	64	100	223
	Wet DMM	0	50	41	125	162
No Crustal Heat Generation	DMM	70	150	14	180	108
	Pyrolite	45	115	24	145	159
	Pyroxenite	40	120	4	160	28
	Basalt	0	0	121	10	339
	Wet Pyrolite	0	55	44	100	223
	Wet DMM	0	70	29	125	163

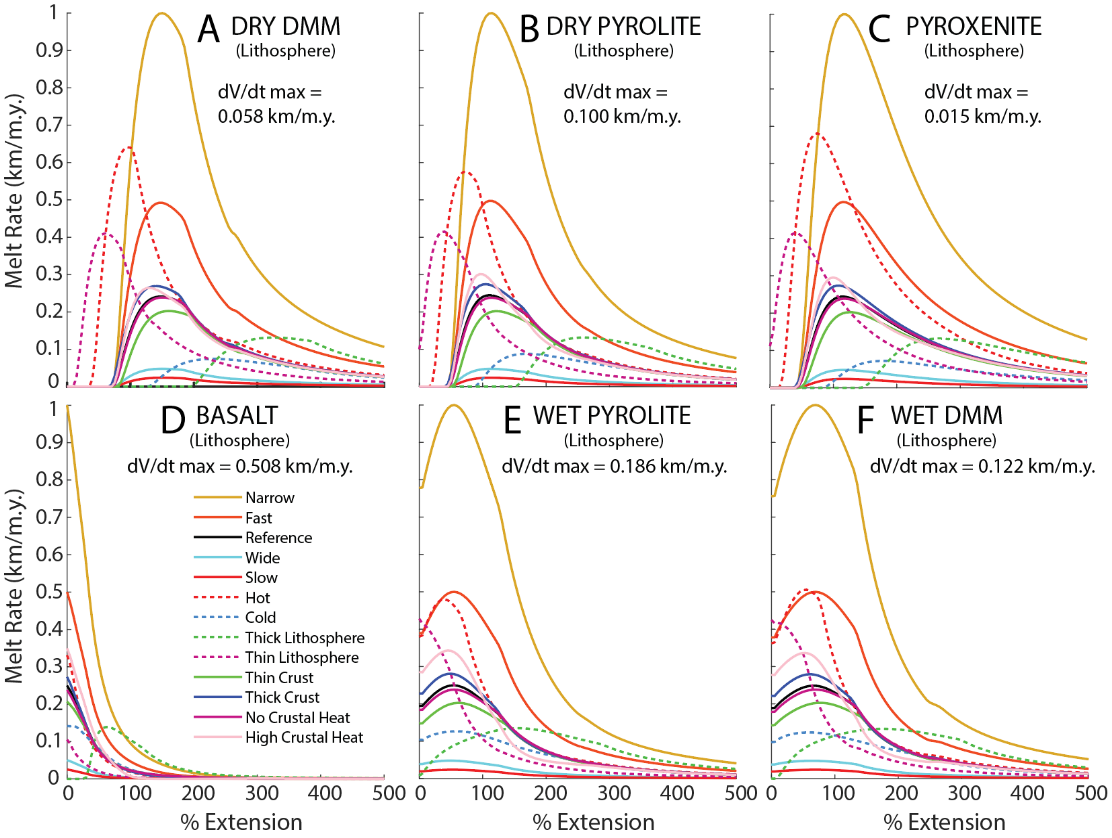

Figure B1.1. Syn-rift melt production rates for different candidate source rock compositions within the lithosphere assuming different pre-rift mantle temperatures, lithosphere and crustal thicknesses, extension rates, rift widths, and crustal heat generation (Table 1.1). Solid lines show models that begin melting and reach peak melt production rates at similar amounts of extension. Dashed lines compare models with different pre-rift lithosphere thicknesses and mantle potential temperatures which have the most impact on the amount of extension required for the onset of melting as well as achieving peak melt production rates. The Reference model plots under the No Crustal Heat model. The plots are normalized by the maximum melt production rate (dV/dt max).

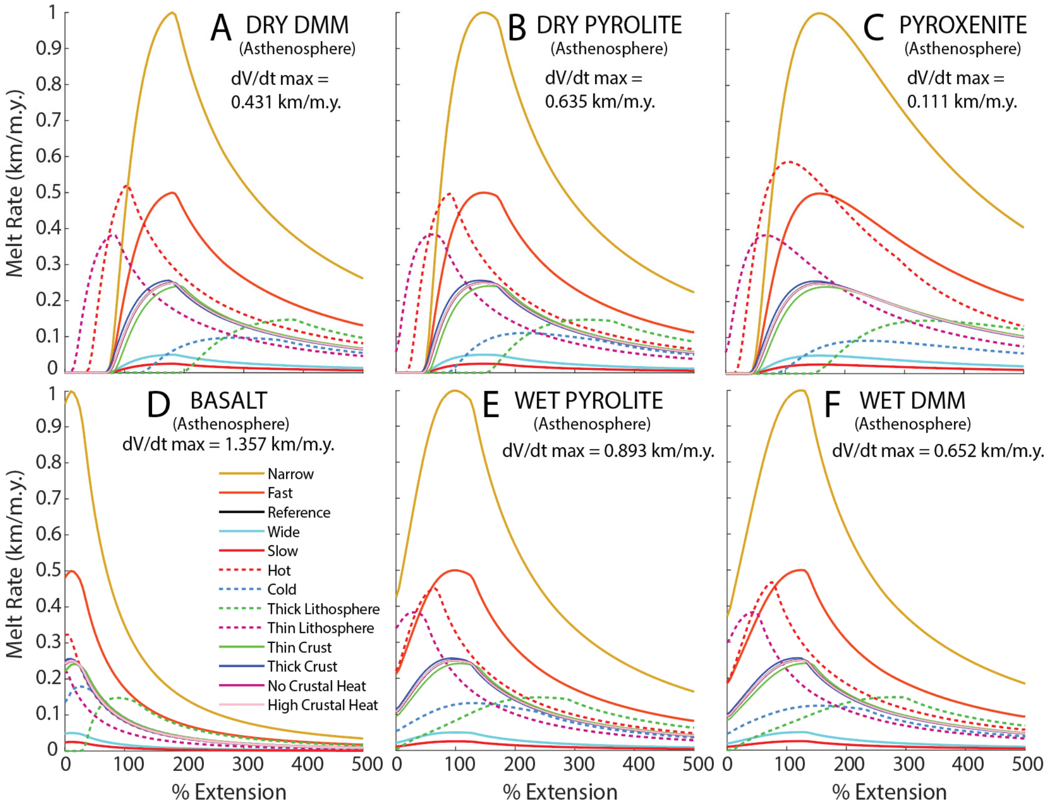

Figure B1.2. Syn-rift melt production rates for different candidate source rock compositions within the asthenosphere assuming different pre-rift mantle temperatures, lithosphere and crustal thicknesses, extension rates, rift widths, and crustal heat generation (Table 1.1). Solid lines show models that begin melting and reach peak melt production rates at similar amounts of extension. Dashed lines compare models with different pre-rift lithosphere thicknesses and mantle potential temperatures which have the most impact on the amount of extension required for the onset of melting as well as achieving peak melt production rates. The Reference model plots under the No Crustal Heat model. The plots are normalized by the maximum melt production rate (dV/dt max).

References in chapter 1

Allègre, C. J., & Turcotte, D. L. (1986). Implications of a two-component marble-cake mantle. Nature, 323(6084), 123–127. https://doi.org/10.1038/323123a0

Aviado, K. B., Rilling-Hall, S., Bryce, J. G., & Mukasa, S. B. (2015). Submarine and subaerial lavas in the West Antarctic Rift System: Temporal record of shifting magma source components from the lithosphere and asthenosphere. Geochemistry, Geophysics, Geosystems, 16(12), 4344–4361. https://doi.org/10.1002/2015GC006076

Bown, J. W., & White, R. S. (1995). Effect of finite extension rate on melt generation at rifted continental margins. Journal of Geophysical Research, 100(B9), 18011–18029. https://doi.org/10.1029/94jb01478

Brown, E. L., & Lesher, C. E. (2016). REEBOX PRO: A forward model simulating melting of thermally and lithologically variable upwelling mantle. Geochemistry, Geophysics, Geosystems, 17(10), 3929–3968. https://doi.org/10.1002/2016GC006579

Fitton, J. G., James, D., & Leeman, W. P. (1991). Basic magmatism associated with late Cenozoic extension in the western United States: Compositional variations in space and time. Journal of Geophysical Research: Solid Earth, 96(B8), 13693–13711. https://doi.org/10.1029/91JB00372

Gilligan, A., Priestley, K. F., Roecker, S. W., Levin, V., & Rai, S. S. (2015). The crustal structure of the western Himalayas and Tibet. Journal of Geophysical Research: Solid Earth, 120(5), 3946–3964. https://doi.org/10.1002/2015JB011891

Gallagher, K., & Hawkesworth, C. (1992). Dehydration melting and the generation of continental flood basalts. Nature, 358(6381), 57–59. https://doi.org/10.1038/358057a0

Harry, D. L., & Leeman, W. P. (1995). Partial melting of melt metasomatized subcontinental mantle and the magma source potential of the lower lithosphere. Journal of Geophysical Research: Solid Earth, 100(B6), 10255–10269. https://doi.org/10.1029/94JB03065

Hasterok, D., & Webb, J. (2017). On the radiogenic heat production of igneous rocks. Geoscience Frontiers, 8(5), 919–940. https://doi.org/10.1016/j.gsf.2017.03.006

Hirose, K., & Kushiro, I. (1993). Partial melting of dry peridotites at high pressures: Determination of compositions of melts segregated from peridotite using aggregates of diamond. Earth and Planetary Science Letters, 114(4), 477–489. https://doi.org/10.1016/0012-821X(93)90077-M

Hirschmann, M. M., Kogiso, T., Baker, M. B., & Stolper, E. M. (2003). Alkalic magmas generated by partial melting of garnet pyroxenite. Geology, 31(6), 481–484. https://doi.org/10.1130/0091-7613(2003)031<0481:AMGBPM>2.0.CO;2

Huerta, A. D., & Harry, D. L. (2007). The transition from diffuse to focused extension: Modeled evolution of the West Antarctic Rift system. Earth and Planetary Science Letters, 255(1–2), 133–147.

https://doi.org/10.1016/j.epsl.2006.12.011

Katsura, T., Yoneda, A., Yamazaki, D., Yoshino, T., & Ito, E. (2010). Adiabatic temperature profile in the mantle. Physics of the Earth and Planetary Interiors, 183(1), 212–218. https://doi.org/10.1016/j.pepi.2010.07.001

Katz, R. F., Spiegelman, M., & Langmuir, C. H. (2003). A new parameterization of hydrous mantle melting. Geochemistry, Geophysics, Geosystems, 4(9), 1–19. https://doi.org/10.1029/2002GC000433

Kimura, J.-I., & Kawabata, H. (2015). Ocean Basalt Simulator version 1 (OBS 1): Trace element mass balance in adiabatic melting of a pyroxenite-bearing peridotite. Geochemistry, Geophysics, Geosystems, 16(1), 267–300. https://doi.org/10.1002/2014GC005606

Kushiro, I. (1996). Partial Melting of a Fertile Mantle Peridotite at High Pressures: An Experimental Study Using Aggregates of Diamond. In Earth Processes: Reading the Isotopic Code (pp. 109–122). American Geophysical Union (AGU). https://doi.org/ 10.1029/GM095p0109

Kushiro, I. (2001). Partial melting experiments on peridotite and origin of mid-ocean ridge basalt. Annual Review of Earth and Planetary Sciences, 29(1), 71–107. https://doi.org/10.1146/annurev.earth.29.1.71

Laó-Dávila, D. A., Al-Salmi, H. S., Abdelsalam, M. G., & Atekwana, E. A. (2015). Hierarchical segmentation of the Malawi Rift: The influence of inherited lithospheric heterogeneity and kinematics in the evolution of continental rifts. Tectonics, 34(12), 2399–2417. https://doi.org/10.1002/2015TC003953

Lee, C. T. A., Luffi, P., Plank, T., Dalton, H., & Leeman, W. P. (2009). Constraints on the depths and temperatures of basaltic magma generation on Earth and other terrestrial planets using new thermobarometers for mafic magmas. Earth and Planetary Science Letters, 279(1–2), 20–33. https://doi.org/10.1016/J.EPSL.2008.12.020

Leeman, W. P., & Harry, D. L. (1993). A binary source model for extension-related magmatism in the Great Basin, western North America. Science, 262(5139), 1550–1554. https://doi.org/10.1126/science.262.5139.1550

Lippard, S. J., & Truckle, P. H. (1978). Spatial and temporal variations in basalt geochemistry in the N. Kenya rift. In Petrology and Geochemistry of Continental Rifts: Volume One of the Proceedings of the NATO Advanced Study Institute Paleorift Systems with Emphasis on the Permian Oslo Rift, held in Oslo, Norway, July 27--August 5, 1977 (pp. 123–131). Springer. https://doi.org/10.1007/978-94-009-9803-2_11

Lum, C. C. L., Leeman, W. P., Foland, K. A., Kargel, J. A., & Fitton, J. G. (1989). Isotopic variations in continental basaltic lavas as indicators of mantle heterogeneity: Examples from the western US Cordillera. Journal of Geophysical Research: Solid Earth, 94(B6), 7871–7884. https://doi.org/10.1029/JB094iB06p07871

MacDonald, R., Rogers, N. W., Fitton, J. G., Black, S., & Smith, M. (2001). Plume-lithosphere interactions in the generation of the basalts of the Kenya Rift, East Africa. Journal of Petrology, 42(5), 877–900. https://doi.org/10.1093/petrology/42.5.877

McKenzie, D., & Bickle, M. J. (1988). The volume and composition of melt generated by extension of the lithosphere. Journal of Petrology, 29(3), 625–679. https://doi.org/10.1093/petrology/29.3.625

McMillan, N. J., Dickin, A. P., & Haag, D. (2000). Evolution of magma source regions in the Rio Grande rift, southern New Mexico. GSA Bulletin, 112(10), 1582–1593. https://doi.org/10.1130/0016-7606(2000)112<1582:EOMSRI>2.0.CO;2

Palme, H., & O'Neill, H. S. C. (2014). 3.1 Cosmochemical estimates of mantle composition. In H. Holland & K. K. Turekian (Eds.), Treatise on Geochemistry (2nd ed.). Elsevier. https://doi.org/10.1016/B978-0-08-095975-7.00201-1

Panter, K. S., Castillo, P., Krans, S., Deering, C., McIntosh, W., Valley, J. W., Kitajima, K., Kyle, P., Hart, S., & Blusztajn, J. (2018). Melt Origin across a Rifted Continental Margin: a Case for Subduction-related Metasomatic Agents in the Lithospheric Source of Alkaline Basalt, NW Ross Sea, Antarctica. Journal of Petrology, 59(3), 517–558. https://doi.org/10.1093/petrology/egy036

Pertermann, M., & Hirschmann, M. M. (2003). Partial melting experiments on a MORB-like pyroxenite between 2 and 3 GPa: Constraints on the presence of pyroxenite in basalt source regions from solidus location and melting rate. Journal of Geophysical Research: Solid Earth, 108(B2). https://doi.org/ 10.1029/2000JB000118

Pilet, S. (2015). Generation of low-silica alkaline lavas: Petrological constraints, models, and thermal implications. In G. R. Foulger, M. Lustrino, & S. D. King (Eds.), The Interdisciplinary Earth: A Volume in Honor of Don L. Anderson (pp. 281–304). Geological Society of America. https://doi.org/10.1130/2015.2514(17)

Pilet, S., Baker, M. B., Müntener, O., & Stolper, E. M. (2011). Monte Carlo simulations of metasomatic enrichment in the lithosphere and implications for the source of alkaline basalts. Journal of Petrology, 52(7–8), 1415–1442. https://doi.org/10.1093/petrology/egr007

Pilet, S., Baker, M. B., & Stolper, E. M. (2008). Metasomatized lithosphere and the origin of alkaline lavas. Science, 320(5878), 916–919. https://doi.org/10.1126/science.1156563

Pitcavage, E., Furman, T., Nelson, W. R., Kalegga, P. K., & Barifaijo, E. (2021). Petrogenesis of primitive lavas from the Toro Ankole and Virunga Volcanic Provinces: Metasomatic mineralogy beneath East Africa's Western Rift. Lithos, 396–397, 106192. https://doi.org/10.1016/j.lithos.2021.106192

Rooney, T. O. (2020). The Cenozoic magmatism of East Africa: Part V – Magma sources and processes in the East African Rift. Lithos, 360–361, 105296. https://doi.org/10.1016/j.lithos.2019.105296

Rooney, T. O., Herzberg, C., & Bastow, I. D. (2012). Elevated mantle temperature beneath East Africa. Geology, 40(1), 27–30. https://doi.org/10.1130/G32382.1

Rudnick, R. L., & Gao, S. (2014). 4.1 - Composition of the Continental Crust. In H. D. Holland & K. K. Turekian (Eds.), Treatise on Geochemistry (Second Edition) (Second Edi, pp. 1–51). Elsevier. https://doi.org/10.1016/B978-0-08-095975-7.00301-6

Steinberger, B., & Becker, T. W. (2018). A comparison of lithospheric thickness models. Tectonophysics, 746, 325–338. https://doi.org/10.1016/j.tecto.2016.08.001

Szwillus, W., Afonso, J. C., Ebbing, J., & Mooney, W. D. (2019). Global Crustal Thickness and Velocity Structure From Geostatistical Analysis of Seismic Data. Journal of Geophysical Research: Solid Earth, 124(2), 1626–1652. https://doi.org/10.1029/2018JB016593

Tetreault, J. L., & Buiter, S. J. H. (2018). The influence of extension rate and crustal rheology on the evolution of passive margins from rifting to break-up. Tectonophysics, 746, 155–172. https://doi.org/10.1016/j.tecto.2017.08.029

Turcotte, D. L., & Schubert, G. (2002). Geodynamics (2nd ed.). Cambridge University Press. https://doi.org/10.1017/CBO9780511807442

Wasylenki, L. E., Baker, M. B., Kent, A. J. R., & Stolper, E. M. (2003). Near-solidus Melting of the Shallow Upper Mantle: Partial Melting Experiments on Depleted Peridotite. Journal of Petrology, 44(7), 1163–1191. https://doi.org/10.1093/petrology/44.7.1163

CHAPTER 2: IMPACTS OF EARLY SYN-RIFT MELTING ON THE MAGMATIC AND STRUCTURAL EVOLUTION OF A RIFT[2]

2.1. Introduction

Syn-rift magmatism occurring at or shortly after the onset of rifting is often attributed to decompression melting of easily fusible mafic or ultramafic rocks entrained in the lithosphere and/or asthenosphere (e.g., Aviado et al., 2015; McMillan et al., 2000; Panter et al., 2018; Rooney, 2020). This early syn-rift melting produces alkalic magmatism that precedes decompression melting of the more pervasive upper mantle lherzolite (Pilet et al., 2008, 2011). As rifting proceeds, fertile and volatile components in the upper mantle are consumed (e.g., Mayle & Harry, 2023). Ensuing melting of lherzolite produces increasingly abundant tholeiitic magmas as the rift matures, ultimately producing midocean ridge basalt (MORB) and new oceanic crust at continental breakup (Kushiro, 1996; Wasylenki et al., 2003). Eclogite, pyroxenite, amphibole-bearing metasomes, and hydrous lithologies are often invoked as the source of early syn-rift magmas. These relatively fusible source rocks are typically envisioned to have been emplaced in the uppermost mantle (lower lithosphere and upper asthenosphere) by prior magmatism or metasomatism that is often attributed to mantle plumes or previous subduction episodes (Aviado et al., 2015; Pilet, 2015). Examples of rifts in which early syn-rift magmatism has been attributed to melting of fusible materials entrained in the upper mantle include the East African Rift System (Rooney, 2020), the Rio Grande Rift and Basin and Range province (Leeman & Harry, 1993; McMillan et al., 2000), and the West Antarctic Rift System (Panter & Martin, 2023; Rocchi & Smellie, 2021). Previous studies show that syn-rift melting enhances cooling of the ascending mantle as a result of latent heat consumed during

---

[2] Chapter 2 has been prepared for submission to *Geology*.

melting (e.g., Bown & White, 1995; Pedersen & Ro, 1992). In rift systems that have more than one fusible lithology, this cooling of the mantle complicates the later magmatic history. The earliest syn-rift melts are produced by the most fusible lithologies present in the lithosphere and/or asthenosphere. The temperature reduction associated with the production of these melts may delay or prevent later melting of less fusible lithologies. In this paper we expand on previous studies of syn-rift melting in a compositionally heterogeneous mantle (Mayle & Harry, 2023) to investigate how cooling associated with the latent heat of melting affects later magmatism and the thermal and strength evolution of a rift. We present a new 1D geodynamic modeling program which considers the latent heat of melting and computes the volume of melt generated from a compositionally heterogenous upper mantle during rifting. We employ this program to consider the effects of early syn-rift latent heat consumption on later magmatism and how it impacts the strength of the lithosphere.

2.2. Methods

To evaluate the impacts of latent heat of melting on the thermal, magmatic, and structural evolution of a rift, we modified the MATLAB program MELT1D (Mayle & Harry, 2023) to produce a new geodynamic modeling tool, MELT1D2. MELT1D2 uses a fourth order Runge-Kutta finite difference method to compute a 1D pressure-temperature (P-T) profile in the lithosphere and asthenosphere as the lithosphere thins or thickens during extension or compression (Appendix A2). The P-T profiles are used to calculate melt fraction vs. depth (F) and total melt production (thickness) through time for various hypothetical mantle compositions. The MELT1D2 model consists of crust, lithosphere mantle, and asthenosphere mantle. Users define the thickness, density, and thermal properties of each layer. Heat production in the crust may be included. A library of functions (solidi, liquidi, and melting functions) simulating melting of a variety of mafic and hydrous or anhydrous ultramafic rocks in the mantle is provided. These include dry and wet depleted lherzolite, which are taken to represent the dominant asthenospheric and lithospheric mantle rocks in the models presented here (Brown & Lesher, 2016; Katz et al., 2003; McKenzie & Bickle, 1988); dry and wet pyrolite, taken to represent a more primitive mantle (Brown & Lesher, 2016); dry harzburgite taken to represent a refractory mantle (Brown & Lesher, 2016); dry pyroxenite taken to represent fusible ultramafic source rocks (Brown & Lesher, 2016; Hirschmann et al., 2003; Kimura & Kawabata, 2015; Pertermann & Hirschmann, 2003); and basalt taken to represent fusible mafic source rocks (Harry & Leeman, 1995; Mayle & Harry, 2023). Users define the mantle composition by prescribing the initial mass fraction of each lithology. The lithosphere is assumed to deform by uniform pure shear with the asthenosphere rising vertically beneath. User specified boundary conditions include constant side velocities (either extension or shortening) or constant velocities at the base of the lithosphere (either thinning or thickening). Thermal boundary conditions include surface temperature, mantle potential temperature, and the asthenosphere adiabatic gradient.

MELT1D2 begins the model in thermal equilibrium as determined by solving the steady state conductive heat equation for the lithosphere temperature-depth profile and applying adiabatic conditions in the asthenosphere. Pressures are then calculated using the temperature profile and density model. It is possible that the computed initial P-T profile exceeds the solidus for one or more of the user-prescribed mantle compositional components. The initial compositional model is therefore corrected if necessary, so as not to exceed the mantle's storage capacity of each lithology given the prescribed initial P-T conditions.

To step the model forward in time, the depth of each node in the finite difference model is first updated according to the kinematic extension/compression model. The 1D transient conductive heat equation, including a latent heat term for each lithology, is then solved to determine lithosphere temperatures at the new time (Appendix A2). After computing the lithosphere T profile, the asthenosphere T profile is updated for adiabatic decompression/compression. Pressure and then melt fraction of each composition is calculated for the lithosphere and asthenosphere. Melt fractions are calculated using solidi, liquidi, and melting functions for each lithology as described in detail in Appendix A of Mayle and Harry (2023). A latent heat correction is then applied to the asthenosphere temperature profile as described by Schubert et al. (2001). The incremental increase in melt fraction between time steps is integrated over depth to estimate the total melt production for each lithology during the given time interval. When comparing the asthenosphere temperatures calculated using the latent heat approximation in MELT1D2 with those from a more thermodynamically rigorous code such as REEBOX PRO (Brown & Lesher, 2016; Brown et al., 2020) assuming similar thermal parameters (e.g., entropy change due to melting, specific heat, and thermal expansion coefficients), we find that the MELT1D2 asthenosphere temperatures (and thus melt fractions) are slightly higher than those from REEBOX PRO. Despite not solving the full thermodynamic system, MELT1D2 only overestimates asthenosphere temperatures by a maximum of ~13 – 15 °C in the compositional models evaluated in this work when compared to calculations using REEBOX PRO, with corresponding melt fractions overestimated by ~0 – 0.07 (Appendix B2). Thus, the temperatures and melt production estimates computed with MELT1D2 are considered maxima.

2.3. Model results and discussion

2.3.1. Model setup

The models simulating rifting that are presented here are similar to the Type model of Mayle and Harry (2023) and are considered to represent typical rift conditions. The models consist of three layers (crust, lithosphere mantle, asthenosphere) that extend from the surface to 400 km depth. The initial thicknesses of the crust and lithosphere are 40 km and 120 km, respectively. The initial width of the extending region is 200 km. The models maintain a surface temperature of 0 °C, mantle potential temperature of 1350 °C, and asthenosphere adiabatic gradient of 4×10^{-4} °C m^{-1}. A constant lithosphere thinning rate of 2 mm yr^{-1} is applied, which corresponds to an initial extension rate of ~3 mm yr^{-1} (accelerating to ~12 cm yr^{-1} after 500% extension). The model is extended until the crust has thinned to 7 km, corresponding to 500% extension. This is similar to the thickness of continental crust at the seaward edge of many rifted continental margins (e.g., Druet et al., 2018; Lau et al., 2006), and so is taken to approximate the time of continental breakup. The lithosphere has thinned to 20 km at this time.

The syn-rift melting histories of three different idealized mantle compositions are evaluated. In the first, the mantle consists entirely of lherzolite, which we take to be representative of the ambient upper mantle (lithosphere and asthenosphere) in all models. We use the DMM (depleted MORB mantle) melting relations of Brown and Lesher (2016) for this lithology. We refer to this model as the DMM-only model. The second compositional model contains 15% fusible ultramafic components (MIX1G pyroxenite of Hirschmann et al., 2003) entrained within the upper mantle lherzolite and is referred to as DMM+P1. MIX1G pyroxenite is taken here to represent pyroxenite veins or intrusions emplaced by prior magmatic episodes. The third model, referred to as DMM+P1+P2, contains 15% ultramafic material (MIX1G pyroxenite) in the upper mantle as well as 15% of a mafic and more fusible composition (G2 pyroxenite of Pertermann & Hirschmann, 2003). The G2 pyroxenite is more basaltic and fusible than MIX1G pyroxenite and taken to represent subducted oceanic crust or intrusions emplaced during prior magmatic episodes. While buoyancy is not calculated in these simple 1D models we recognize that asthenosphere mantle with 15-30% pyroxenite would require a thermal anomaly in order to upwell (Brown & Lesher, 2014; Shorttle et al. 2014).

2.3.2. Impact of melting on rift thermal evolution

The models show that the maximum amount of melting occurs near the lithosphere-asthenosphere boundary (LAB), regardless of the composition. Accordingly, this is the depth at which the mantle temperature is most impacted by latent heat consumed during melting. For example, if the mantle consists only of lherzolite (DMM-only model), LAB temperatures at the end of rifting are ~50 °C cooler in the models including latent heat than in models neglecting latent heat (Figure 2.1). Corresponding maximum melt fractions at the LAB are 0.152 and 0.187 (Figure 2.1 insets).

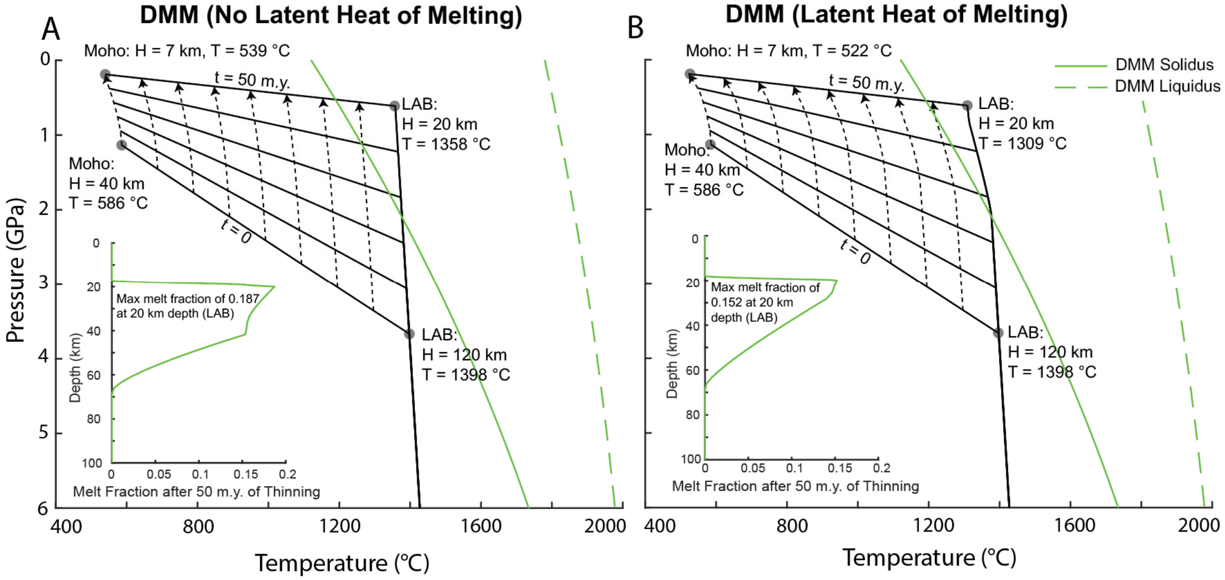

Figure 2.1. Pressure–temperature (P-T) plots for the DMM model (A) without and (B) with latent heat of melting considered. DMM solidus - solid green line; liquidus - dashed green line. Subvertical dashed lines show P_T paths of individual packets of rock in the lithospheric mantle. P-T paths are shown at 10 km (pre-rift) depth intervals, from the base of the crust (Moho) to the lithosphere-asthenosphere boundary (LAB). Solid lines show P-T conditions in the mantle at 10 m.y. intervals, from the onset of extension (t = 0) to the end of rifting (t = 50 m.y.). Subhorizontal and subvertical solid lines indicate lithosphere and asthenosphere mantle P-T paths, respectively. Subplots show melt fraction vs. depth at the end of rifting (t = 50 m.y.). H and T indicate lithosphere depth and temperature at the base of the lithosphere at the given time.

The inclusion of fusible components in the mantle (DMM+P1 and DMM+P1+P2 models) results in relatively lower melt fractions of less fusible sources and larger degrees of syn-rift cooling (Figure 2.2). For example, by the end of thinning in the DMM+P1 model the maximum melt fractions are 0.149 for DMM (0.003 less than in the DMM-only model) and 0.372 for MIX1G pyroxenite. The resulting temperature at the LAB is 1303 °C which is 6 °C cooler than the DMM-only model (Figure 2.2a). Similarly, the maximum melt fractions of DMM (0.126) and MIX1G pyroxenite (0.262) are lower in the DMM+P1+P2 model than in either the DMM-only and DMM+P1 models. However, the maximum melt fraction of G2 pyroxenite is 1 indicating that the G2 component has melted out. The temperature at the LAB (1281 °C) in the DMM+P1+P2 model is 22 °C and 28 °C cooler than the DMM+P1 and DMM-only models, respectively (Figure 2.2b). The enhanced cooling (and decreased melt fractions for DMM) experienced by DMM+P1

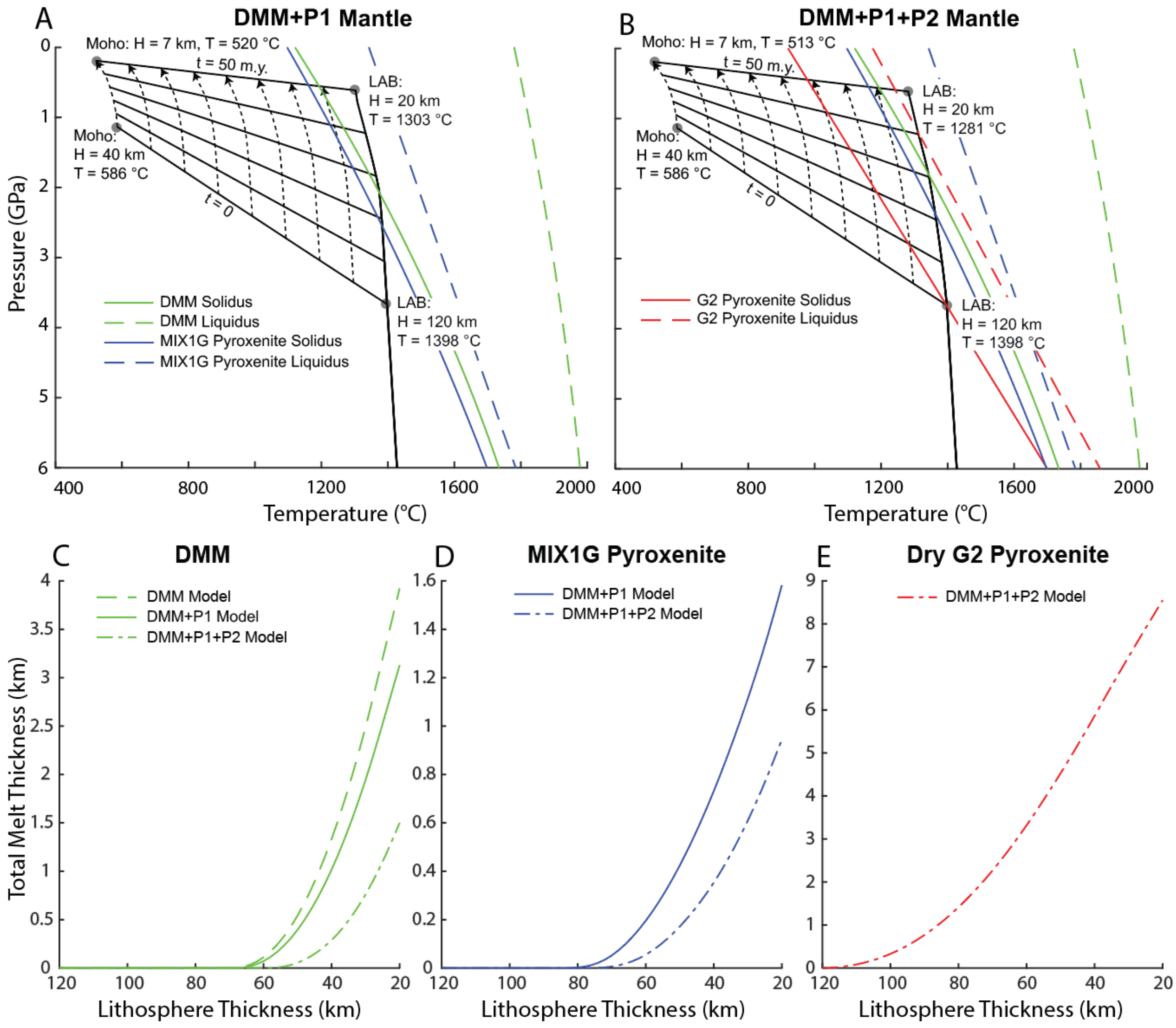

Figure 2.2. Top row: Pressure–temperature (P-T) plots for the DMM+P1 model (85% DMM, 15% G2 pyroxenite) (A) and the DMM+P1+P2 model (70% DMM, 15% G2 pyroxenite, 15% MIX1G pyroxenite) (B). Models include latent heat of melting (compare to Figure 1B). Solidi (solid colored lines) and liquidi (dashed colored lines) are shown for DMM lherzolite (green), MIX1G pyroxenite (blue), and G2 pyroxenite (red). Bottom Row: Thickness of melt produced during extension in the various models by (C) DMM lherzolite, (D) MIX1G pyroxenite, and (E) G2 pyroxenite.

and DMM+P1+P2 models relative to the DMM-only model is attributed to enhanced cooling due to latent heat consumption during melting of the most fusible lithologies (i.e., MIX1G and G2 pyroxenite).

2.3.3. Impact of early syn-rift melting on magmatic evolution of the rift

Enhanced cooling of the upper mantle associated with latent heat consumed during early syn-rift melting of the most fusible components in a heterogeneous mantle may delay or prevent melting of less fusible lithologies (e.g., Phipps Morgan, 2001). These less fusible lithologies require either more decompression (more lithosphere thinning) or addition of heat to melt relative to mantle that does not contain highly fusible components. For example, a mantle consisting entirely of lherzolite (DMM-only model) begins to melt after the lithosphere has thinned to 70 km (Figure 2.2c). In the DMM+P1 model containing 15% MIX1G pyroxenite, the pyroxenite begins melting after the lithosphere has thinned to only 84 km (Figure 2.2d). Enhanced cooling due to melting of the pyroxenite delays melting of DMM until the lithosphere has thinned to 68 km (rather than the 70 km required if MIX1G pyroxenite is absent). In the DMM+P1+P2 model, G2 pyroxenite begins to melt at the onset of lithosphere thinning (Figure 2.2e). The resulting enhanced cooling delays melting of both MIX1G pyroxenite (until the lithosphere has thinned to 78 km rather than 84 km) and DMM (until 60 km rather than 68 km or 70 km).

In all models tested, mantle with more fusible material produced more total melt. For example, the DMM-only model produced 3.9 km of total melt, the DMM+P1 model produced 5.7 km of total melt, and the DMM+P1+P2 model produced 11 km of total melt. The thickness of melt produced at breakup from a given lithology is lower if other more fusible lithologies are also present (Figures 2.2c -2.2e). For example, in the DMM-only model, where DMM is the only lithology present, 3.9 km of melt is produced by breakup. In the DMM+P1 model, 3.1 km and 1.6 km of melt (5.7 km total) are produced from the DMM and MIX1G pyroxenite sources, respectively, by the end of rifting. In the DMM+P1+P2 model, 1.5 km of melt is produced from the DMM source, 0.9 km of melt is produced from the MIX1G pyroxenite source, and 8.6 km of melt is produced from the G2 pyroxenite source by breakup (11 km total). These melt thicknesses are similar to the amount of melt produced to form new oceanic crust at the time of continental breakup (White et al., 1992). If a more fusible lithology is present, the less fusible lithology produces less melt over the duration of thinning. The decrease in melt production of the less fusible lithologies due to melting of the more fusible lithologies is consistent with previous models of decompression melting of the asthenosphere (Brown & Lesher, 2016; Matthews et al., 2016, 2021; Phipps

Morgan, 2001; Shorttle et al., 2014). As pointed out by Phipps Morgan (2001) and Hirschmann and Stolper (1996), melting of the most fusible lithologies may be enhanced by heat transfer from less fusible lithologies. This would coincide with cooling of the less fusible lithologies. The models considered here did not consider the transfer of heat from the least to most fusible lithologies. Consequently, the models shown here likely underestimate the volume of melt from the most fusible lithology and overestimate the volume and underestimate the amount of extension prior to onset of melting of less fusible lithologies.

2.3.4. Impact of early syn-rift melting on lithosphere strength

To compare the strength of the lithosphere during extension between the different compositional models, dislocation creep flow laws are assumed for the crust (wet quartz after Hirth et al., 2001) and mantle (dry olivine after Hirth & Kohlstedt, 2003) with a frictional limit defined by Byerlee's law (Byerlee, 1978) (Figure 2.3). At the end of thinning, the integrated lithospheric strength (obtained by integrating the yield strength curve over the thickness of the lithosphere) for the DMM, DMM+P1, and DMM+P1+P2 models are similar (3.6×10^{12} N m^{-1}, 3.7×10^{12} N m^{-1}, and 3.8×10^{12} N m^{-1}, respectively). Regardless of the degree of mantle metasomatism, the latent heat consumption associated with syn-rift melting has minimal impact on the strength evolution of a rift over the range of thinning rates tested (1 – 4 mm yr^{-1}). This is because most of the syn-rift cooling associated with latent heat consumption during melting occurs near the LAB, as this is where most melt is produced (Figures 2.1b, 2.2a, and 2.2b). However, this has little effect on the integrated lithospheric strength because mantle temperatures are so high at this depth that the mantle remains weak compared to the crust and uppermost mantle (Figure 2.3). While it is broadly accepted that magmatism assists and promotes rifting, we find that the cooling associated with latent heat consumption due to melting does not greatly impact lithosphere temperatures and thus the latent heat of melting has little to no influence on the structural evolution of a rift. This implies that other aspects of melting such as dike propagation (Buck et al., 2006), localized heating due to intrusions (Schmeling & Wallner, 2012), and fault lubrication (Toro et al., 2006) play a much larger role in rifting.

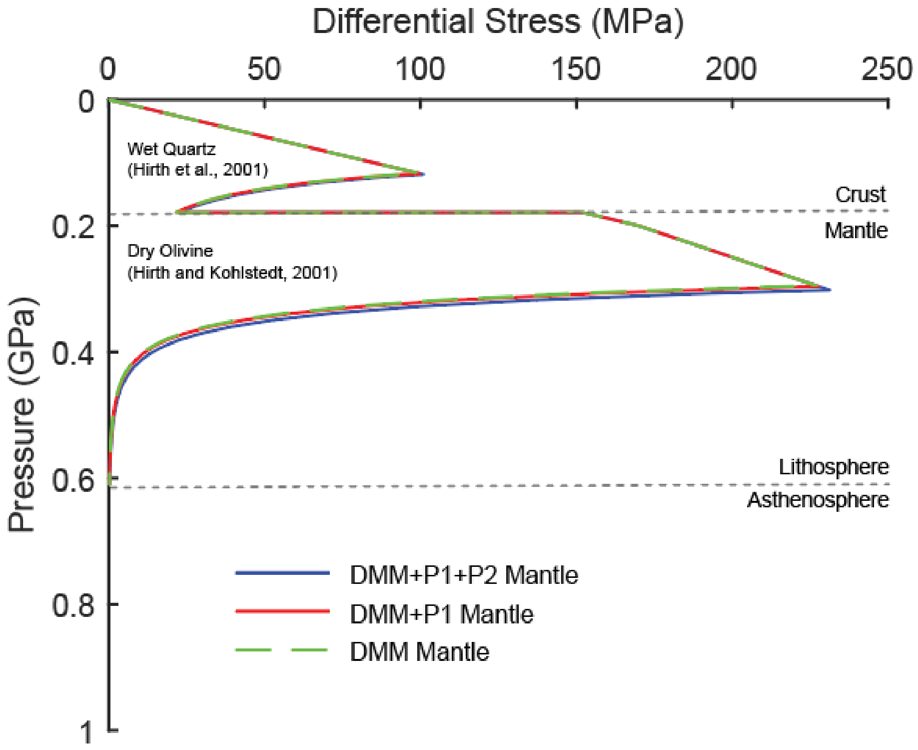

Figure 2.3. Yield stress vs. pressure for the DMM (dashed green line), DMM+P1 (red), and DMM+P1+P2 (blue) models at the end of rifting (t = 50 m.y.). Rheological model uses wet quartz (Hirth et al., 2001) and dry olivine (Hirth and Kohlstedt, 2001) dislocation flow laws for the crust and lithosphere mantle, respectively, and Byerlee's law to simulate frictional failure. Note similarity of strength envelopes for all compositional models.

2.4. Conclusions

The effects of latent heat consumed by syn-rift magma production on the thermal, magmatic, and strength evolution of a rift were evaluated for three different mantle compositional models: depleted lherzolite mantle (DMM-only model: 100% DMM), moderately metasomatized mantle (DMM+P1 model: 85% DMM, 15% MIX1G pyroxenite), and highly metasomatized mantle (DMM+P1+P2 model: 70% DMM, 15% MIX1G pyroxenite, 15% G2 pyroxenite). We find that:

1. Melting and thus cooling of the mantle due to latent heat consumed by melting is most pronounced in the lower lithosphere and upper asthenosphere, reducing temperatures at the LAB by as much as ~30 °C in the most highly metasomatized mantle model (DMM+P1+P2 model) compared to the depleted mantle model (DMM-only model).
2. Cooling due to latent heat consumed by melting of the most fusible lithologies during the earliest stages of extension inhibits later melting of less fusible lithologies. Less fusible lithologies require relatively more thinning to begin melting and produce less melt if more fusible lithologies are present in the upper mantle prior to extension (Figure 2.4).
3. Cooling due to latent heat consumption by syn-rift melting has little impact on the net strength of the lithosphere, as most of the strength resides in the uppermost mantle (near the base of the crust) and within the crust, where no decompression melting is predicted to occur.

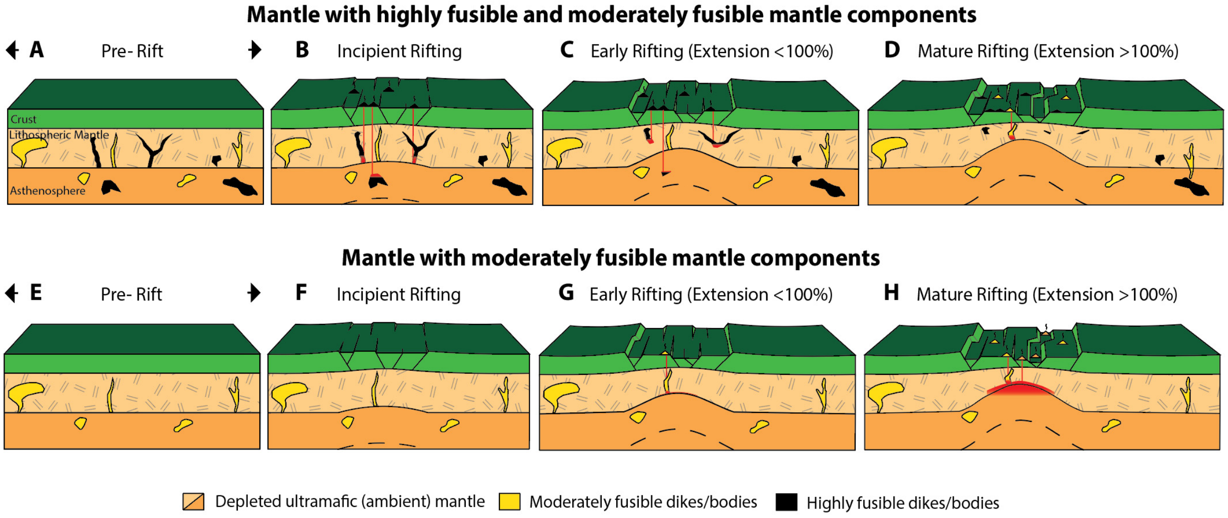

Figure 2.4. Conceptual model showing melting sequence in a heterogeneous mantle during extension. A-D): Melt sequence in mantle containing highly fusible (e.g., G2 pyroxenite) and moderately fusible (e.g., MIX1G pyroxenite) components embedded in lherzolite (similar to DMM+P1+P2 model). E-H: Melt sequence in mantle containing moderately fusible (e.g., MIX1G pyroxenite) components embedded in lherzolite (similar to DMM+P1 model). In the top row, highly fusible source rocks begin to melt at the onset of rifting (B) and continue to produce melt through the early stages of rifting (extension < 100%) (C). By mature rifting stages (extension > 100%), moderately fusible sources in a heterogenous mantle also begin to melt (D). In the bottom row, moderately fusible sources begin to melt during the early stages of rifting (G), earlier than the mantle model with more fusible components. In the mature rifting stages, moderately fusible sources continue to produce melt (H) and ambient mantle (e.g., DMM) begins to melt. Melt is indicated by red. Triangles indicate surface expression of magmatism and are colored by source. The dashed line in B-D and F-H represents upwelling asthenosphere. Figure is modified from Mayle and Harry (2023).

Appendix A2

We use a new 1D model, MELT1D2, to compute the pressure, *P*, and temperature, *T*, profiles within the lithosphere and asthenosphere as the lithosphere thins (or thickens) beneath a rift (or orogen). The P-T profiles are used to estimate the melt thickness produced by thinning (or thickening) of the lithosphere and rising asthenosphere. The code considers the melting of a library of lithologies ranging from ultramafic to mafic including hydrous and anhydrous sources. To do this we modified MELT1D to include latent heat of melting when computing the temperature and melt fraction, *F*. In the lithosphere, we add a latent heat term to the heat equation after Schubert et al. (2001). In the asthenosphere, the temperature profile is taken to be adiabatic. This profile is then corrected for the change in temperature associated with the latent heat of melting. This approximates the full thermodynamic solution in the asthenosphere and validation of this approximation is described below in Appendix B2. Utilizing the approximation allows users to consider the latent heat of melting (in the lithosphere and asthenosphere) for lithologies not currently in more thermodynamically rigorous codes such as REEBOX PRO (Brown & Lesher, 2016; Brown et al., 2020), pyMelt (Matthews et al., 2022), and MELTs (Ghiorso & Sack, 1995).

Below we describe the algorithm of MELT1D2 (Figure A2.1), which estimates decompression/compression melting of user defined lithologies and fractional abundance in a layered model that includes the crust, lithosphere mantle, and asthenosphere. We first describe the initial conditions and computations completed during the initial timestep, which represent the model before the onset of rifting/convergence. This is followed by a description of the calculations completed in all other timesteps which begin with a description of the 1D mechanical model that tracks the thickness of the crust and lithosphere through time (either extension or compression). Then we describe how temperatures are solved. First, we solve the heat equation for the lithosphere temperature profile, including the latent heat of melting term. The asthenosphere temperatures are then updated for adiabatic decompression. Next, we update the density and pressure in the lithosphere and asthenosphere. This P-T profile is then used to

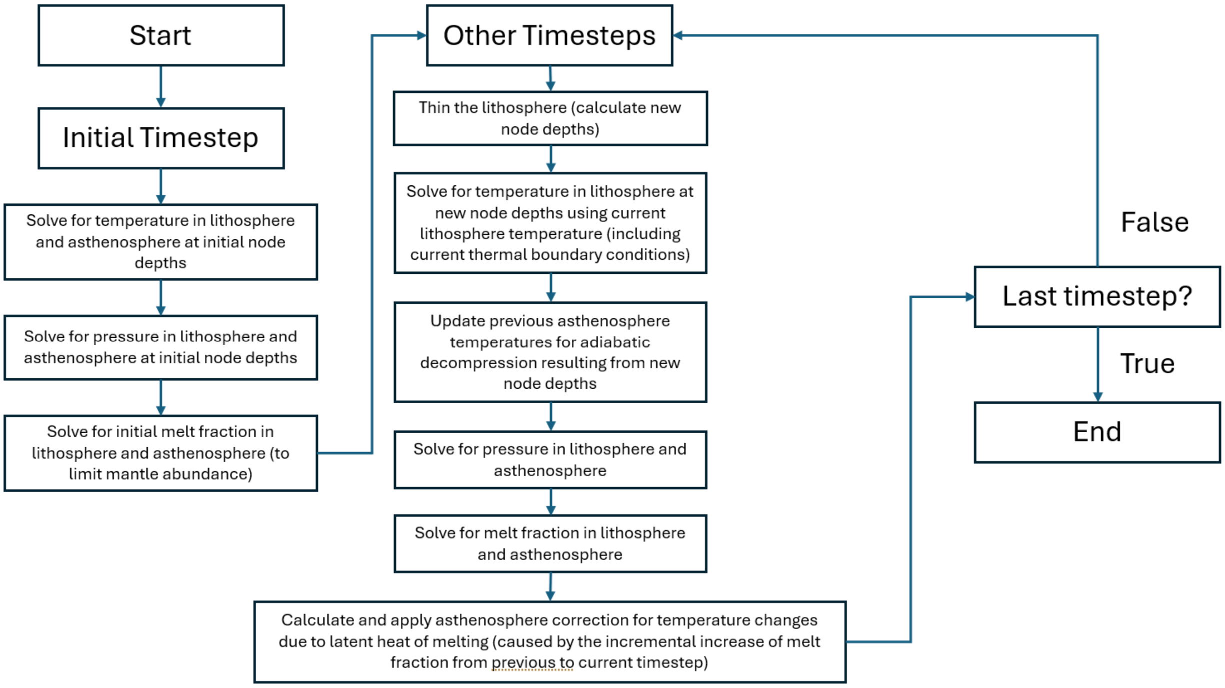

Figure A2.1. General programmatic flow chart for MELT1D2.

calculate the melt fraction of each lithology scaled by the fractional abundance as a function of depth at the new time step. Then, we compute the asthenosphere temperature change (decrease) due to latent heat consumed during melting and update the asthenosphere temperatures. Finally, we integrate the melt fraction over depth to calculate total melt production (thickness) at a given time for each lithology.

The model is discretized on a Lagrangian reference frame, with model nodes that ascend or descend as the lithosphere thickens or thins. Initial conditions and computations for the model at $t = 0$, where t is time, are described by Mayle and Harry (2023) and include assumptions that initial lithosphere temperatures are steady state ($dT/dt = 0$) and that asthenosphere temperatures are adiabatic. Using lithosphere and asthenosphere temperatures, the pressure and then nominal melt fractions for each model composition are computed. The nominal melt fraction of each lithology at $t = 0$ represents portions of the given lithology that could not be sequestered at initial pressure and temperature conditions. We then take the user-defined ideal compositional model and reduce it by the nominal melt fraction to find the initial compositional model.

For all following timesteps, model nodes ascend/descend as the lithosphere thins /thickens. If assuming constant extension/compression rate, U_x, the depth of each node in the lithosphere is given by:

$$z(t) = \frac{z(0)}{\left(1 + \frac{U_x t}{L_0}\right)}, \qquad 0 < z < z_L \tag{A1}$$

where L_0 is the initial rift width and z_L is the depth to the base of the lithosphere. The ascent rate of each node, U_z, is found by:

$$U_z(t) = \frac{-z(0)\frac{U_x}{L_0}}{\left(1 + \frac{U_x t}{L_0}\right)^2}, \qquad 0 < z < z_L. \tag{A2}$$

If assuming constant lithosphere thinning /thickening rate (U_{zl}) the depth and ascent rate of each node in the lithosphere is given by:

$$z(t) = z(0) - U_z t, \qquad 0 < z < z_L \tag{A3}$$

$$U_z(t) = U_{zl}\frac{z(0)}{z_L}, \qquad 0 < z < z_L \tag{A4}$$

In the asthenosphere, the depths to model nodes are recalculated as the base of the lithosphere ascends/descends to keep the number of nodes in the asthenosphere and the depth to the bottom of the asthenosphere constant.

The temperature profile is then computed. In the lithosphere we compute the *T(z)* profile by solving the heat equation (Mayle & Harry, 2023) with a term for latent heat (Schubert et al., 2001) using finite differences as described by Harry and Leeman (1995):

$$\rho C_p \frac{dT}{dt} = A + \nabla \cdot k\nabla T + \rho C_p U_z G_a + T\Delta S \frac{dF}{dt} X, \qquad 0 < z < z_L \tag{A5}$$

where *A* is heat production, ρ is density, C_p is specific heat, *k* is thermal conductivity, G_a is the mantle adiabatic temperature gradient, ΔS is entropy change due to melting, and *X* is the mass fraction of the lithology. Equation A5 is identical to the heat equation solved in MELT1D with the exception of the last term which is the new functionality in MELT1D2. The thermal boundary conditions necessary to solve for lithosphere temperatures are the surface temperature and temperature at the top of the asthenosphere (taken from the previous timestep). We then update the previous asthenosphere temperatures for adiabatic decompression/compression:

$$T(z) = T_0(z) + G_a \Delta z, \qquad z_L \leq z \leq z_a \tag{A6}$$

where Δz is the node depth from the previous timestep subtracted from the current node depth, z_a is the depth to the base of the asthenosphere, and T_0 is the temperature of the node from the previous timestep. The updated temperature in the lithosphere and the previous temperature in the asthenosphere (updated for decompression) are used to calculate *P(z)* and *F(z)* for each model composition as described by Mayle and Harry (2023). Next, we apply the asthenosphere correction for temperature changes due to latent heat of melting, ΔT, for the current timestep. First, we linearly approximate the temperature change due to latent heat of melting after Schubert et al. (2001):

$$\Delta T(z) = T(z)\Delta S \Delta F(z)\frac{X}{C_p}, \qquad z_L \leq z \leq z_a \tag{A7}$$

where $\Delta F(z)$ is the incremental increase of melt fraction from the previous to current timestep. Then we update asthenosphere temperatures for the temperature change due to latent heat of melting:

$$T(z) = T(z) - \Delta T(z), \qquad z_L \leq z \leq z_a\,. \tag{A8}$$

Last, we integrate *F(z)* to find melt production as described in Mayle and Harry (2023).

Appendix B2

To evaluate the accuracy of the approximation of melt production in the asthenosphere and the corresponding effect on asthenosphere temperatures we compare the MELT1D2 and REEBOX PRO (Brown & Lesher, 2016; Brown et al., 2020) solutions. REEBOX PRO is a thermodynamically robust forward modeling application that simulates adiabatic decompression of upwelling mantle. This tool solves for both the temperature and melt fraction for a given pressure in the asthenosphere using thermodynamic and experimental constraints. To compare results of MELT1D2 with those of REEBOX PRO, we use the compositional models previously discussed in the Results and Discussion section and similar thermal parameters (e.g., entropy change due to melting, specific heat, and thermal expansion coefficients) for both codes. These compositional models include the DMM-only (depleted mantle), DMM+P1 (moderately metasomatized mantle), and DMM+P1+P2 (highly metasomatized mantle) cases. We find that the approximation of cooling due to latent heat of melting used in MELT1D2 produces similar asthenosphere temperatures in comparison to REEBOX PRO. The maximum difference between asthenosphere temperatures from MELT1D2 and REEBOX PRO occurs when the modeled asthenosphere is at its shallowest depths at the end of modeled extension (Table B2.1 and Figure B2.1). By the end of modeled thinning, the top of the asthenosphere lies at ~0.6 GPa for all three cases. As reported in the results and discussion section, the temperatures at the top of the asthenosphere for the DMM-only, DMM+P1, and DMM+P1+P2 models are 1309 °C, 1303 °C and 1281 °C, respectively, in MELT1D2. The REEBOX PRO temperatures are slightly lower for the same compositional models (1296 °C, 1290 °C, and 1266 °C, respectively). Thus, the MELT1D2 asthenosphere temperatures at the top of the asthenosphere are approximately 13 – 15 °C hotter than the REEBOX PRO temperatures. The higher modeled temperatures at the top of the asthenosphere by the end of modeled extension in MELT1D2 lead to a greater extent of melting than the REEBOX PRO solution (Table B2.1). For example, in the tested compositions (at the end of rifting) the greatest difference in melt fraction between MELT1D2 and REEBOX PRO results are observed

Table B2.1. Comparison of melt fractions and mantle temperatures in the asthenosphere at breakup[a] for MELT1D2 and REEBOX PRO

Model	Mantle Composition	Melt Fraction		Mantle Temperature (°C) at LAB[b]		Temperature Difference (MELT1D2 temperature – REEBOX PRO temperature)	Melt Fraction Difference (MELT1D2 melt fraction – REEBOX PRO melt fraction)
		REEBOX PRO	MELT1D2	REEBOX PRO	MELT1D2		
DMM	100% DMM	0.148	0.152	1296.03	1308.94	12.91	0.004
DMM+P1	85% DMM	0.146	0.149	1289.98	1302.79	12.81	0.003
	15% MIX1G Pyroxenite	0.303	0.372				0.069
DMM+P1+P2	70% DMM	0.092	0.126	1266.13	1281.35	15.22	0.034
	15% MIX1G Pyroxenite	0.193	0.262				0.069
	15% G2 Pyroxenite	1	1				0

[a] We assume breakup occurs when the crust has thinned to 7 km which is the thickness of oceanic crust.
[b] LAB is the lithosphere-asthenosphere boundary.

for MIX1G pyroxenite. In the DMM+P1+P2 model, MELT1D2 melt fraction for MIX1G pyroxenite are ~0.07 lower than the REEBOX PRO melt fraction. Our approximation results summarized in Table B2.1, show that the MELT1D2 asthenosphere melt fractions are ~0 – 0.07 higher than the REEBOX PRO estimates.

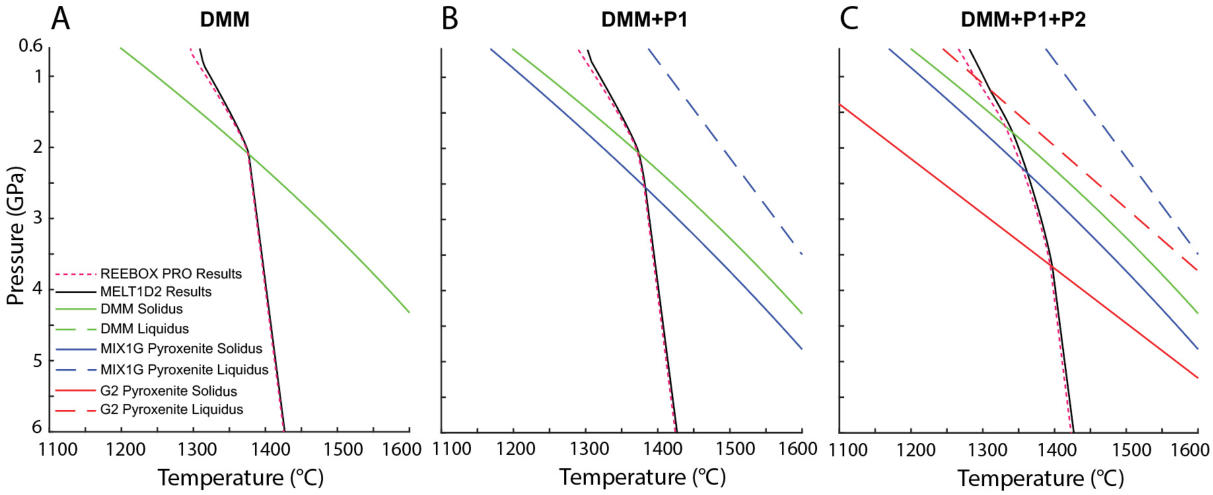

Figure B2.1. Pressure–temperature (P-T) plots of the asthenosphere at the end of rifting for MELT1D2 (black solid line) and REEBOX PRO (pink dashed line) for identical mantle compositions which ranges from pressures of 0.6 – 6 GPa. The results are shown for different mantle compositional models A) DMM (100% DMM), B) DMM+P1 (80% DMM, 15% MIX1G pyroxenite), and C) DMM+P1+P2 (70% DMM, 15% MIX1G pyroxenite, and 15% G2 pyroxenite). The solidi (solid lines) and liquidi (dashed lines) are shown for DMM (green), MIX1G pyroxenite (blue), and G2 pyroxenite (red).

References in chapter 2

Aviado, K. B., Rilling-Hall, S., Bryce, J. G., & Mukasa, S. B. (2015). Submarine and subaerial lavas in the West Antarctic Rift System: Temporal record of shifting magma source components from the lithosphere and asthenosphere. Geochemistry, Geophysics, Geosystems, 16(12), 4344–4361. https://doi.org/10.1002/2015GC006076

Bown, J. W., & White, R. S. (1995). Effect of finite extension rate on melt generation at rifted continental margins. Journal of Geophysical Research, 100(B9), 18011–18029. https://doi.org/10.1029/94jb01478

Brown, E. L., & Lesher, C. E. (2014). North Atlantic magmatism controlled by temperature, mantle composition and buoyancy. Nature Geoscience, 7(11), 820–824. https://doi.org/10.1038/ngeo2264

Brown, E. L., & Lesher, C. E. (2016). REEBOX PRO: A forward model simulating melting of thermally and lithologically variable upwelling mantle. Geochemistry, Geophysics, Geosystems, 17(10), 3929–3968. https://doi.org/10.1002/2016GC006579

Brown, E. L., Petersen, K. D., & Lesher, C. E. (2020). Markov chain Monte Carlo inversion of mantle temperature and source composition, with application to Reykjanes Peninsula, Iceland. Earth and Planetary Science Letters, 532, 116007. https://doi.org/10.1016/J.EPSL.2019.116007

Buck, W. R., Einarsson, P., & Brandsdóttir, B. (2006). Tectonic stress and magma chamber size as controls on dike propagation: Constraints from the 1975–1984 Krafla rifting episode. Journal of Geophysical Research: Solid Earth, 111(B12). https://doi.org/https://doi.org/10.1029/2005JB003879

Byerlee, J. (1978). Friction of rocks. Pure and Applied Geophysics, 116(4–5), 615–626. https://doi.org/10.1007/BF00876528

Druet, M., Muñoz-Martín, A., Granja-Bruña, J. L., Carbó-Gorosabel, A., Acosta, J., Llanes, P., & Ercilla, G. (2018). Crustal structure and continent-ocean boundary along the Galicia continental margin (NW Iberia): Insights from combined gravity and seismic interpretation. Tectonics, 37(5), 1576–1604. https://doi.org/https://doi.org/10.1029/2017TC004903

Ghiorso, M. S., & Sack, R. O. (1995). Chemical mass transfer in magmatic processes IV. A revised and internally consistent thermodynamic model for the interpolation and extrapolation of liquid-solid equilibria in magmatic systems at elevated temperatures and pressures. Contributions to Mineralogy and Petrology, 119(2), 197–212. https://doi.org/10.1007/BF00307281

Harry, D. L., & Leeman, W. P. (1995). Partial melting of melt metasomatized subcontinental mantle and the magma source potential of the lower lithosphere. Journal of Geophysical Research: Solid Earth, 100(B6), 10255–10269. https://doi.org/10.1029/94JB03065

Hirschmann, M. M., & Stolper, E. M. (1996). A possible role for garnet pyroxenite in the origin of the “garnet signature” in MORB. Contributions to Mineralogy and Petrology, 124(2), 185–208. https://doi.org/10.1007/s004100050184

Hirschmann, M. M., Kogiso, T., Baker, M. B., & Stolper, E. M. (2003). Alkalic magmas generated by partial melting of garnet pyroxenite. Geology, 31(6), 481–484. https://doi.org/10.1130/0091-7613(2003)031<0481:AMGBPM>2.0.CO;2

Hirth, G., & Kohlstedf, D. (2003). Rheology of the upper mantle and the mantle wedge: A view from the experimentalists. Geophysical Monograph-American Geophysical Union, 138, 83–106.

Hirth, G., Teyssier, C., & Dunlap, J. W. (2001). An evaluation of quartzite flow laws based on comparisons between experimentally and naturally deformed rocks. International Journal of Earth Sciences, 90(1), 77–87. https://doi.org/10.1007/s005310000152

Katz, R. F., Spiegelman, M., & Langmuir, C. H. (2003). A new parameterization of hydrous mantle melting. Geochemistry, Geophysics, Geosystems, 4(9), 1–19. https://doi.org/10.1029/2002GC000433

Kimura, J. I., & Kawabata, H. (2015). Ocean Basalt Simulator version 1 (OBS 1): Trace element mass balance in adiabatic melting of a pyroxenite-bearing peridotite. Geochemistry, Geophysics, Geosystems, 16(1), 267–300. https://doi.org/10.1002/2014GC005606

Kushiro, I. (1996). Partial melting of a fertile mantle peridotite at high pressures: An experimental study using aggregates of diamond. In A. Basu & S. R. Hart (Eds.), Earth Processes: Reading the Isotopic Code (pp. 109–122). American Geophysical Union (AGU). https://doi.org/https://doi.org/10.1029/GM095p0109

Lau, K. W. H., Louden, K. E., Funck, T., Tucholke, B. E., Holbrook, W. S., Hopper, J. R., & Christian Larsen, H. (2006). Crustal structure across the Grand Banks—Newfoundland Basin Continental Margin — I. Results from a seismic refraction profile. Geophysical Journal International, 167(1), 127–156.

https://doi.org/10.1111/j.1365-246X.2006.02988.x

Leeman, W. P., & Harry, D. L. (1993). A binary source model for extension-related magmatism in the Great Basin, western North America. Science, 262(5139), 1550–1554. https://doi.org/10.1126/science.262.5139.1550

Matthews, S., Shorttle, O., & Maclennan, J. (2016). The temperature of the Icelandic mantle from olivine-spinel aluminum exchange thermometry. Geochemistry, Geophysics, Geosystems, 17(11), 4725–4752. https://doi.org/https://doi.org/10.1002/2016GC006497

Matthews, S., Wong, K., & Gleeson, M. (2022). pyMelt: An extensible Python engine for mantle melting calculations. Volcanica, 5(2), 469–475. https://doi.org/10.30909/vol.05.02.469475

Matthews, S., Wong, K., Shorttle, O., Edmonds, M., & Maclennan, J. (2021). Do olivine crystallization temperatures faithfully record mantle temperature variability? Geochemistry, Geophysics, Geosystems, 22(4), e2020GC009157. https://doi.org/https://doi.org/10.1029/2020GC009157

Mayle, M., & Harry, D. L. (2023). Syn-rift magmatism and sequential melting of fertile lithologies in the lithosphere and asthenosphere. Journal of Geophysical Research: Solid Earth, 128(9), e2023JB027072. https://doi.org/https://doi.org/10.1029/2023JB027072

McKenzie, D., & Bickle, M. J. (1988). The volume and composition of melt generated by extension of the lithosphere. Journal of Petrology, 29(3), 625–679. https://doi.org/10.1093/petrology/29.3.625

McMillan, N. J., Dickin, A. P., & Haag, D. (2000). Evolution of magma source regions in the Rio Grande rift, southern New Mexico. GSA Bulletin, 112(10), 1582–1593. https://doi.org/10.1130/0016-7606(2000)112<1582:EOMSRI>2.0.CO;2

Panter, K. S., & Martin, A. P. (2023). West Antarctic mantle deduced from mafic magmatism. In A. P. Martin & W. van der Wal (Eds.), The Geochemistry and Geophysics of the Antarctic Mantle (pp. 133–149). Geological Society of London, Memoirs. https://doi.org/10.1144/M56-2021-10

Panter, K. .S, Castillo, P., Krans, S., Deering, C., McIntosh, W., Valley, J. W., Kitajima, K., Kyle, P., Hart, S., & Blusztajn, J. (2018). Melt origin across a rifted continental margin: A case for subduction-related metasomatic agents in the lithospheric source of alkaline basalt, NW Ross Sea, Antarctica. Journal of Petrology, 59(3), 517–558. https://doi.org/10.1093/petrology/egy036

Pedersen, T., & Ro, H. E. (1992). Finite duration extension and decompression melting. Earth and Planetary Science Letters, 113(1), 15–22. https://doi.org/https://doi.org/10.1016/0012-821X(92)90208-D

Pertermann, M., & Hirschmann, M. M. (2003). Partial melting experiments on a MORB-like pyroxenite between 2 and 3 GPa: Constraints on the presence of pyroxenite in basalt source regions from solidus location and melting rate. Journal of Geophysical Research: Solid Earth, 108(B2). https://doi.org/https://doi.org/10.1029/2000JB000118

Phipps Morgan, J. (2001). Thermodynamics of pressure release melting of a veined plum pudding mantle. Geochemistry, Geophysics, Geosystems, 2(4). https://doi.org/https://doi.org/10.1029/2000GC000049

Pilet, S. (2015). Generation of low-silica alkaline lavas: Petrological constraints, models, and thermal implications. In G. R. Foulger, M. Lustrino, & S. D. King (Eds.), The Interdisciplinary Earth: A Volume in Honor of Don L. Anderson (pp. 281–304). Geological Society of America. https://doi.org/10.1130/2015.2514(17)

Pilet, S., Baker, M. B., Müntener, O., & Stolper, E. M. (2011). Monte Carlo simulations of metasomatic enrichment in the lithosphere and implications for the source of alkaline basalts. Journal of Petrology, 52(7–8), 1415–1442. https://doi.org/10.1093/petrology/egr007

Pilet, S., Baker, M. B., & Stolper, E. M. (2008). Metasomatized lithosphere and the origin of alkaline lavas. Science, 320(5878), 916–919. https://doi.org/10.1126/science.1156563

Rocchi, S., & Smellie, J. L. (2021). Chapter 5.1b Northern Victoria Land: petrology. In J. L. Smellie, K. S. Panter, & A. Geyer (Eds.), Volcanism in Antarctica: 200 Million Years of Subduction, Rifting and Continental Break-up (pp. 383–413). Geological Society of London, Memoirs. https://doi.org/10.1144/M55-2019-19

Rooney, T. O. (2020). The Cenozoic magmatism of East Africa: Part V – Magma sources and processes in the East African Rift. Lithos, 360–361, 105296. https://doi.org/10.1016/j.lithos.2019.105296

Schmeling, H., & Wallner, H. (2012). Magmatic lithospheric heating and weakening during continental rifting: A simple scaling law, a 2-D thermomechanical rifting model and the East African Rift System. Geochemistry, Geophysics, Geosystems, 13(8). https://doi.org/https://doi.org/10.1029/2012GC004178

Schubert, G., Turcotte, D. L., & Olson, P. (2001). Mantle convection in the Earth and planets. Cambridge University Press.

Shorttle, O., Maclennan, J., & Lambart, S. (2014). Quantifying lithological variability in the mantle. Earth and Planetary Science Letters, 395, 24–40. https://doi.org/https://doi.org/10.1016/j.epsl.2014.03.040

Toro, G. Di, Hirose, T., Nielsen, S., Pennacchioni, G., & Shimamoto, T. (2006). Natural and experimental evidence of melt lubrication of faults during earthquakes. Science, 311(5761), 647–649. https://doi.org/10.1126/science.1121012

Wasylenki, L. E., Baker, M. B., Kent, A. J. R., & Stolper, E. M. (2003). Near-solidus melting of the shallow upper mantle: Partial melting experiments on depleted peridotite. Journal of Petrology, 44(7), 1163–1191. https://doi.org/10.1093/petrology/44.7.1163

CHAPTER 3: SOURCES OF SYN-RIFT MAGMATISM IN THE WEST ANTARCTIC RIFT SYSTEM: INSIGHTS FROM 2D FINITE ELEMENT MODELS OF EXTENSION AND MELTING[3]

3.1. Introduction

Magmatism that occurs during the early stages of continental rifting has been attributed to decompression melting of compositionally fertile components entrained in less fertile lherzolite mantle (Fitton et al., 1991; Harry & Leeman, 1995; Leeman & Fitton, 1989; Leeman & Harry, 1993; Pilet, 2015; Pilet et al., 2008, 2011). Fertile rocks emplaced during prior magmatic events are envisioned to melt sequentially, with the most fertile (least mafic or most hydrous) rocks melting early during the rift history and less fertile rocks (e.g., dry lherzolite) melting later (e.g., Mayle & Harry, 2023). Such a scenario has been suggested to account for the appearance of early syn-rift magmas and progressive changes in basalt chemistry in both narrow rift systems such as the East African Rift and Rio Grande Rift (e.g., McMillan et al., 2000; Pitcavage et al., 2021; Rooney, 2020) and broad rift systems such as the Basin and Range province of western North America (Farmer et al., 2020; Fitton et al., 1991; Harry & Leeman, 1995; Leeman & Harry, 1993). In this paper, we investigate the impacts that early syn-rift melting has on the thermal evolution of a broad continental rift, and how that in turn impacts the strength of the lithosphere and ensuing magmatic and structural evolution of the rift. We focus on the West Antarctic Rift System (WARS), which is frequently referred to as a broad continental rift system (Bialas et al., 2007; Fitzgerald et

---

[3] Chapter 3 has been prepared for submission to *Geophysics, Geochemistry, and Geosystems.*

al., 1986; Huerta & Harry, 2007; Jordan et al., 2020; Panter & Martin, 2023; Storey & Granot, 2021; van Wijk et al., 2008).

The WARS is an 800 - 1000 km wide region of extended crust in West Antarctica (WANT) that lies between the Transantarctic Mountains (TAMS) to the west and Marie Byrd Land to the east (Figure 3.1). There are two main phases of WARS extension: early broad rifting followed by later focused rifting. The initial Cretaceous broad rifting phase was largely amagmatic and produced a series of extensional basins spanning the Ross Sea (Cooper et al., 1991a; Davey & Brancolini, 1995; Lawver & Gahagan, 1994; Panter &

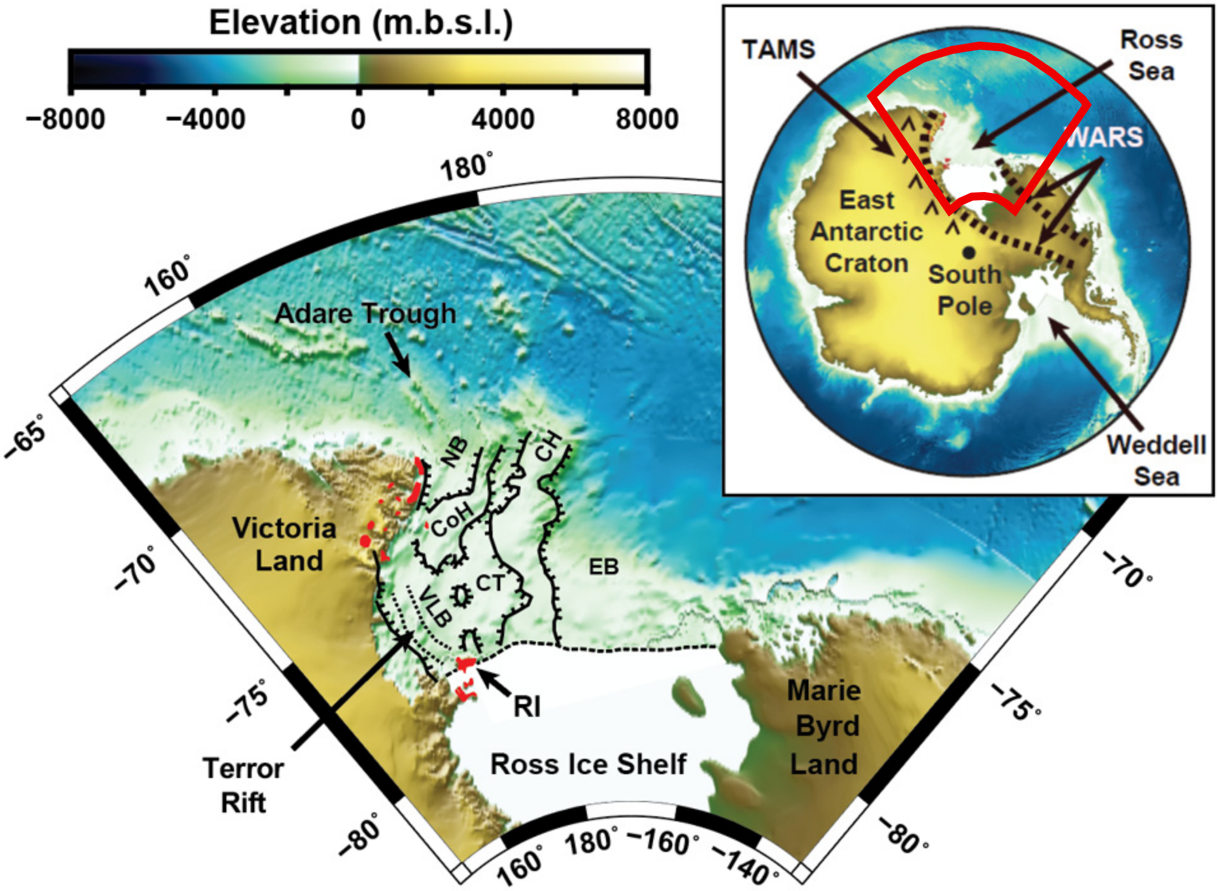

Figure 3.1. Location map of the West Antarctic Rift System (WARS) in the Ross Sea region after Wenman et al (2020). The WARS, the Ross Sea, and Transantarctic Mountains (TAMS) are shown on the inset map. Red outline on inset map shows extent of location map. Black lines show main structures of the Ross Sea (Fielding et al., 2008); red, Cenozoic alkaline volcanic rocks from Victoria Land and Ross Island (RI); Coulman High (CoH); Central High (CH); Central Trough; Eastern Basin (EB); Northern Basin (NB); Victoria Land Basin (VLB).

Martin, 2023; Smellie et al., 2020). This was followed by a Cenozoic phase in which rifting became focused on the margins as extension in the central Ross Sea slowed (Cooper et al., 1991a; Davey & Brancolini, 1995; Fielding et al., 2006; Huerta & Harry, 2007; Spiegel et al., 2016; Storey & Granot, 2021). This Cenozoic rifting was accompanied by magmatism along both flanks of the rift (Smellie & Martin, 2021; Smellie & Rocchi, 2021; Wilch et al., 2021). Two main sources of WARS Cenozoic magmatism have been recognized. Magmatism in Marie Byrd Land and the Ross Island region (including the Ross Island, Mount Morning, and Mount Discovery Volcanic Fields) is widely attributed to melting of mantle plumes underlying each of these regions (Behrendt et al., 1994; Esser et al., 2004; Kyle et al., 1992; LeMasurier & Landis, 1996; Panter & Martin, 2023; Phillips et al., 2018; Storey et al., 1999). Magmatism elsewhere along the western rift flank, particularly in North Victoria Land and the western Ross Sea, is suggested to result from decompression melting of compositionally fertile (relative to depleted lherzolite mantle) or hydrous material in the upper mantle (lithosphere and/or asthenosphere) that was emplaced during previous tectonic and magmatic events (Aviado et al., 2015; Panter et al., 2018; Rocchi et al., 2002; Rocchi & Smellie, 2021). In this paper, we test proposed causes of syn-rift (non-plume) magmatism with a series of finite-element geodynamic models that simulate the structural and magmatic history of the WARS. Specifically, we compare the timing and location of melting in the models with the timing and location of syn-rift magmatic rocks erupted in the WARS. The models evaluate the contribution of various proposed fusible compositions in the pre-rift mantle to syn-rift magmatism in the WARS and how that magmatism impacted the thermal and structural evolution of the rift. We specifically test melting of several dry fertile lithologies that have been proposed as sources of syn-rift (non-plume) magmatism. We do not evaluate melting of wet lithologies, which have also been proposed as sources of WARS syn-rift magmatism (e.g., Aviado et al., 2015; Rocchi et al., 2002), due to the need for computationally intensive iterative methods to solve for the melt fraction (e.g., Katz et al., 2003). We also did not test locally elevated mantle temperatures associated with the Ross Island and Marie Byrd Land plumes as we focus on regional models of WARS extension.

3.2. Tectonic and magmatic history of the WARS

3.2.1. Paleozoic and Mesozoic subduction and terrane accretion

During the last phases of greater Gondwana assembly (~650 - 550 Ma) a subduction system formed along the proto-Pacific margin of the East Antarctic craton (Boger & Miller, 2004; Encarnación & Grunow, 1996; Goodge, 1997, 2020). Throughout the Paleozoic and most of the Mesozoic, the trench system migrated towards the Pacific Ocean as terranes were accreted to East Antarctica (Boger & Miller, 2004; Dalziel & Elliot, 1982; Goodge, 2020; Pankhurst et al., 1998; Rocchi et al., 2011). Four main crustal blocks were accreted during this time and amalgamated to form WANT: the Antarctic Peninsula, Ellsworth-Whitmore Mountains, Thurston Island, and Marie Byrd Land (Figure 3.2) (Dalziel & Elliot, 1982; Dalziel & Lawver, 2001; Storey & Granot, 2021). Calc-alkaline magmatic rocks emplaced during this long period of subduction outcrop on both flanks of the WARS. On the western flank, calc-alkaline rocks are found along the length of the TAMS and have estimated ages spanning 590 – 360 Ma (Allibone & Wysoczanski, 2002; Borg et al., 1987; Encarnación & Grunow, 1996; Goodge, 2020). On the eastern flank, calc-alkaline rocks are found in Marie Byrd Land and have ages spanning 450 – 96 Ma (Adams, 1987; Mukasa & Dalziel, 2000; Pankhurst et al., 1998; Smellie et al., 2020). This was accompanied by alkaline magmatism in Marie Byrd Land from 142 – 95 Ma, which has been attributed to back-arc spreading (Mukasa & Dalziel, 2000; Siddoway, 2008; Siddoway et al., 2005; Smellie et al., 2020; Storey et al., 1999; Weaver et al., 1994).

Subduction ended when the Phoenix-Pacific spreading ridge collided with the trench (Figure 3.3) between ~110 – 100 Ma (Bradshaw, 1989; Jordan et al., 2020; Lawver & Gahagan, 1994; Weaver et al., 1994). The initial collision of the trench and spreading ridge occurred along the northern margin of New

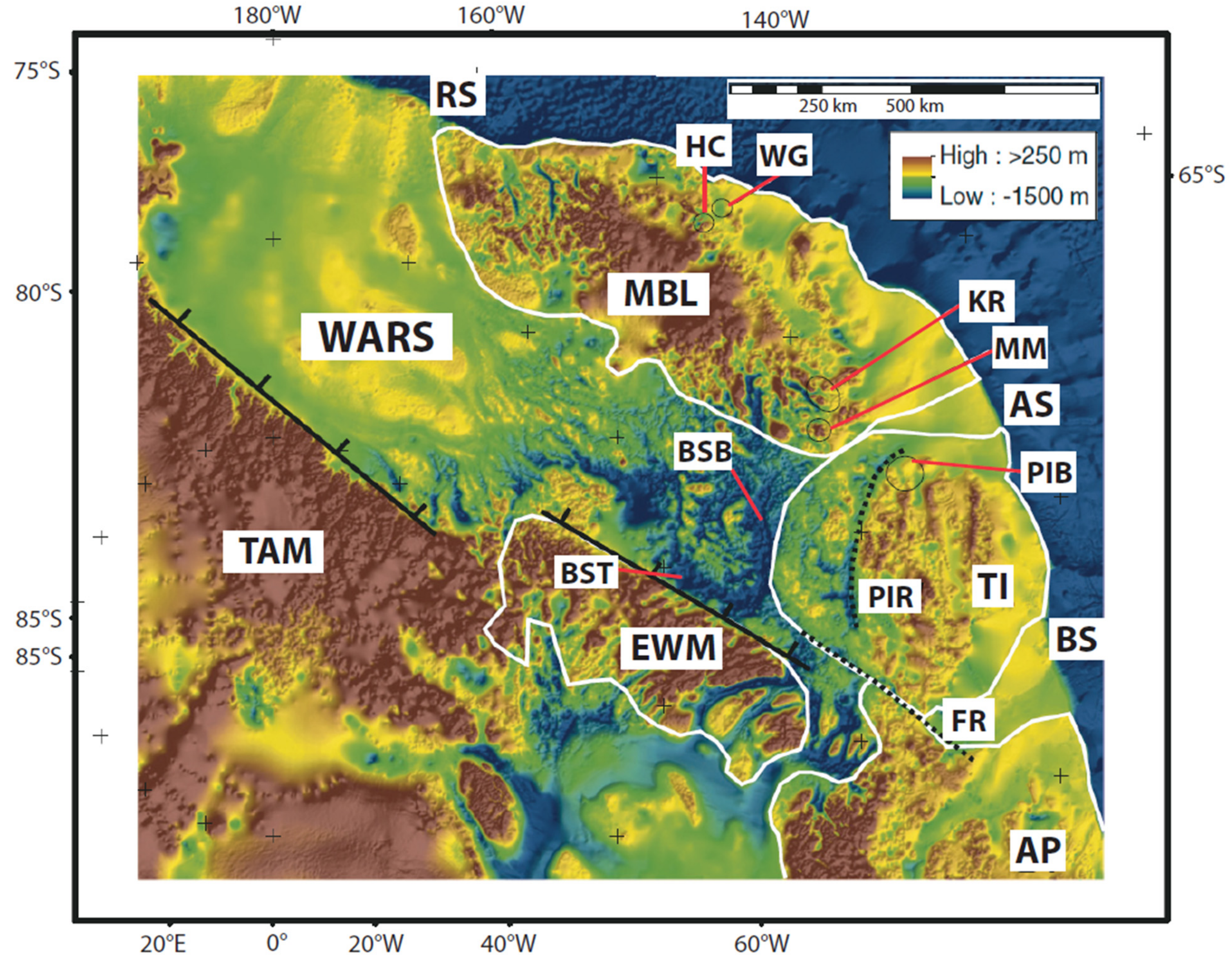

Figure 3.2. Key locations and subglacial topography of West Antarctica after Spiegel et al. (2019). Dotted lines show the axes of rift basins (PIR: Pine Island Rift and FR: Ferrigno Rift). White lines delineate crustal blocks of West Antarctica (MBL: Marie Byrd Land, TI: Thurston Island, AP: Antarctic Peninsula, and EWM: Ellsworth Whitmore Mountains). AS: Amundsen Sea, BS: Bellingshausen Sea, BSB: Byrd Subglacial Basin, BST: Bentley Subglacial Trench, HC: Hobbs Coast, KR: Kohler Range, MM: Mount Murphy, PIB: Pine Island Bay, RS: Ross Sea, TAM: Transantarctic Mountains, WARS: West Antarctic Rift System, WG: Wrigley Gulf.

Zealand, which abutted Marie Byrd Land during the Cretaceous (Bradshaw, 1989; Lawver & Gahagan, 1994; Siddoway, 2008; Weaver et al., 1994). The intersection of the trench and ridge migrated eastward along the Antarctic plate boundary, progressively shutting down subduction and related calc-alkaline magmatism as the two collided (Jordan et al., 2020; Lawver & Gahagan, 1994; Mukasa & Dalziel, 2000; Weaver et al., 1994). The last pulses of calc-alkaline magmatism occurred in the Ruppert and Hobbs Coasts in west-central Marie Byrd Land at 110 Ma and in Pine Island Bay and the Kohler Range of eastern Marie Byrd Land (Figure 3.2) at 96 Ma (Mukasa & Dalziel, 2000).

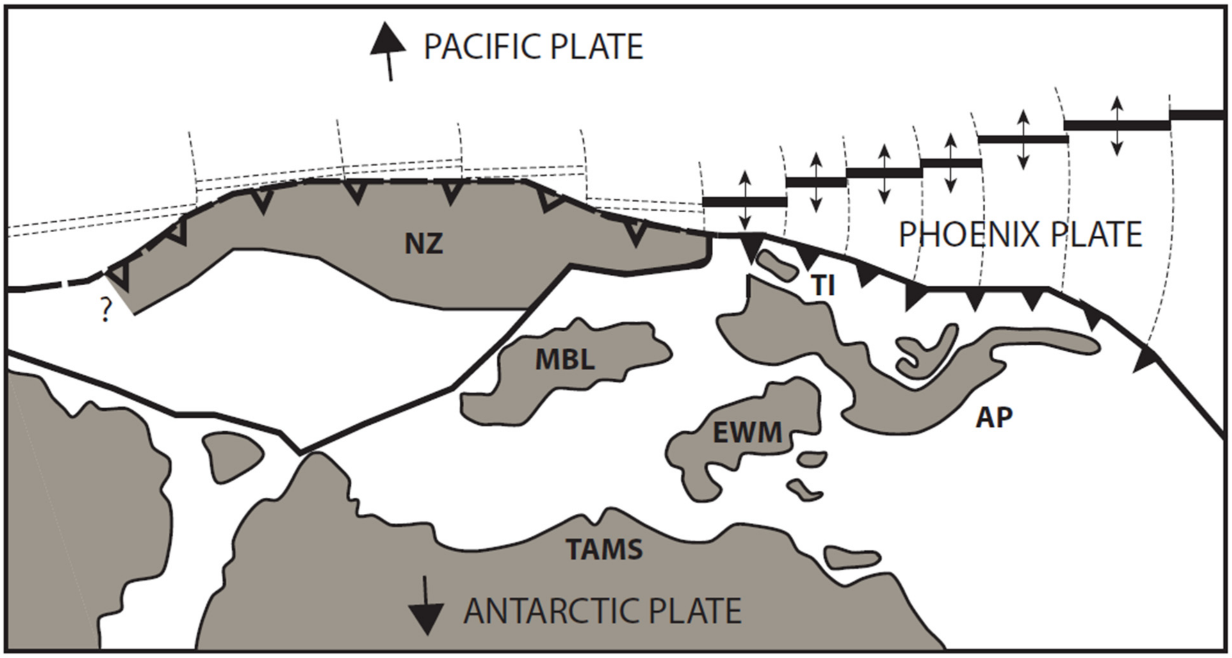

Figure 3.3. Reconstruction of West Antarctic crustal blocks (AP: Antarctic Peninsula, EWM: Ellsworth Whitmore Mountains, MBL: Marie Byrd Land, and TI: Thurston Island) and New Zealand (NZ) at ~100 Ma during ridge-trench collision after Weaver et al (1994). As the ridge collided with the trench, subduction and rifting ceased. After this collision, New Zealand was transferred from the Antarctic to the Pacific plate. Thin dashed lateral lines represent inactive spreading ridge segments. Thin dashed vertical lines represent transform faults. Black rectangles with opposing arrows represent active spreading ridge segments. Open toothed black line represents an extinct segment of the trench and the closed toothed black line represents the active segment. The thick solid black line separating New Zealand and Marie Byrd Land represents the Antarctic plate boundary after the ridge-trench collision. TAMS: Transantarctic Mountains.

3.2.2. Mesozoic and Cenozoic extension of the WARS

3.2.2.1. Cretaceous WARS extension

WARS extension began near the end of subduction at ~105 Ma with an initial broad rifting phase that continued at least until breakup between New Zealand and WANT at ~85 Ma (Jordan et al., 2020; Lawver & Gahagan, 1994; Siddoway, 2008). This rifting phase accommodated most of the extension in the WARS and created the four major Ross Sea basins: the Eastern Basin, Central Basin, Northern Basin, and Victoria Land Basin (Figure 3.1) (Cooper et al., 1991a, 1991b; Davey & Brancolini, 1995). The broad rifting phase was largely amagmatic apart from the alkaline magmatism associated with back-arc spreading in Marie Byrd Land noted above (Panter & Martin, 2023; Siddoway, 2008; Smellie et al., 2020). A possible exception is the presence of magmatic rocks within the interior of the WARS which have been inferred from high amplitude magnetic anomalies in the Ross Sea and Ross Ice Shelf (Behrendt et al., 1991, 1994, 1996; Jordan et al., 2020; Tinto et al., 2019). The ages of these inferred magmatic rocks are unknown and may pre-date, post-date, or be coeval with WARS broad extension.

3.2.2.2. Cenozoic WARS extension

3.2.2.2.1. Western flank of the WARS

Rifting waned within the interior of the WARS and became focused along the margins during the Paleogene (Cooper et al., 1991a, 1991b; Davey & Brancolini, 1995; Fielding et al., 2006, 2008; Granot & Dyment, 2018; Storey & Granot, 2021). Stratal thickness changes observed on seismic profiles show that subsidence and thus extension of the central Ross Sea greatly slowed by the Paleogene (Brancolini et al., 1995; Cooper et al., 1991b; Davey & Brancolini, 1995). As rifting of the central WARS slowed, rifting along the western margin accelerated (Cooper et al., 1991a; Granot et al., 2010, 2013; Granot & Dyment, 2018; Salvini et al., 1997). This is evidenced by basinward thickening of strata and faults observed on seismic profiles and in boreholes from Victoria Land Basin indicating that subsidence rates and faulting increased after 34 Ma (Fielding et al., 2006, 2008; Sauli et al., 2021). Other evidence of accelerated rifting along the western flank includes marine magnetic anomalies extending from the Adare Basin into the Northern Basin. These anomalies indicate seafloor spreading occurred between 43 – 26 Ma (Cande et al., 2000; Cande & Stock, 2006; Davey et al., 2006, 2016) and may have continued at a slower rate until 11 Ma (Granot & Dyment, 2018). The focusing of rifting along the western margin of the Ross Sea during the Paleogene was accompanied by TAMS uplift, which apatite fission track analysis suggests began as early as 55 Ma (Fitzgerald, 1992, 2002; Fitzgerald et al., 1986).

The earliest syn-rift magmatism along the western flank of the Ross Sea is alkaline plutonism that occurred in North Victoria Land between ~50 – 20 Ma (Rocchi et al., 2002; Rocchi & Smellie, 2021). This was followed by volcanism (dominantly alkaline) which spans ~19 Ma to present with most occurring after

10 Ma (Smellie & Martin, 2021; Smellie & Rocchi, 2021). This volcanism is present along the length of the western Ross Sea margin and adjacent TAMS region and includes Victoria Land, the Terror Rift in the Victoria Land Basin, and the Ross Island region (Aviado et al., 2015; Panter et al., 2018; Smellie & Martin, 2021; Smellie & Rocchi, 2021).

Causes of Cenozoic magmatism along the western flank of the WARS differ based on location. Volcanism in the Ross Island region has been attributed to melting of a hot mantle plume currently centered beneath Ross Island (Esser et al., 2004; Kyle et al., 1992; Phillips et al., 2018; Storey et al., 1999). This is supported by slow seismic velocities in the upper mantle and a thinned mantle transition zone under Ross Island, which suggest elevated temperatures consistent with a plume that may persist into the lower mantle (Emry et al., 2020; Lloyd et al., 2020; Phillips et al., 2018; White-Gaynor et al., 2019; Wiens et al., 2023). Enriched incompatible trace element signatures and isotopic compositions in basaltic rocks from the Ross Island region (relative to mid-ocean ridge basalt, MORB) are attributed to the melting of sources more fertile than depleted lherzolite mantle (Martin et al., 2021; Phillips et al., 2018; Sims et al., 2008). The Ross Island region basaltic rocks have a HIMU signature (high μ = 238U/204Pb) which is generally interpreted as being characteristic of melts generated from a plume rising from the core mantle boundary (Hanyu et al., 2011; Homrighausen et al., 2018; Phillips et al., 2018; Sims et al., 2008).

Besides the plume related magmatism in the Ross Island region, magmatism along the western flank of the WARS is enigmatic. The mantle in the WARS region is thought to be relatively cool except for where the Ross Island and Marie Byrd Land plumes are present. Cool mantle temperatures (mantle potential temperature $T_p < 1350$ °C) are indicated by geodynamic models of the WARS structural evolution (Bialas et al., 2007; Harry et al., 2018; Huerta & Harry, 2007; van Wijk et al., 2008) and pressure-temperature histories of Late Cenozoic basalts from North Victoria Land (Armienti & Perinelli, 2010; Perinelli et al., 2006, 2011). These temperatures are well below those of mantle plumes, which are typically ~100 to 300 °C above the global average mantle potential temperature of ~1350 °C (Herzberg et al., 2007; Katsura, 2022; Lee et al., 2009; Rooney et al., 2012). Given present lithospheric thicknesses (60 – 80 km: An et al., 2015b; Wiens et al., 2023) and relatively low mantle potential temperatures ($T_p < 1350$ °C) along the western flank, little to no melting of dry depleted lherzolite mantle would occur (e.g., Mayle & Harry, 2023). However, more fertile (fusible) source rocks such as pyroxenite, basalt, or hydrous lithologies would likely melt under these conditions. Such lithologies in the lithosphere mantle and/or asthenosphere have been suggested to be the source rocks for Cenozoic syn-rift magmatism in North Victoria Land (both onshore and offshore) and Victoria Land Basin based on major element, trace element, and isotopic compositions (Aviado et al., 2015; Panter et al., 2018; Rocchi et al., 2002; Rocchi & Smellie, 2021). Additionally, distinct negative potassium anomalies in these rocks suggest the presence of hydrous minerals (i.e., amphibole and mica) in the source rock (e.g., Panter et al., 2018; Panter & Martin, 2023). Further evidence is provided by major-oxide concentrations (SiO_2, Al_2O_3, and Na_2O) of primitive Ross Sea lavas which Aviado et al. (2015) attribute to a multi-component mantle containing fusible lithologies (i.e., depleted lherzolite ambient mantle containing pyroxenite, hydrous lithologies, and/or eclogite bodies). Such fusible lithologies are suggested to have been emplaced in the lithosphere and/or asthenosphere during the preceding long history of subduction along the western Antarctic margin or during prior tectonomagmatic episodes (Aviado et al., 2015; Panter et al., 2018; Panter & Martin, 2023; Perinelli et al., 2011; Rocchi et al., 2002; Rocchi & Smellie, 2021).

3.2.2.2.2. Eastern flank of the WARS

The geology of the eastern flank of the WARS was dominated by the Marie Byrd Land plume during the Cenozoic (e.g., LeMasurier & Landis, 1996; Panter et al., 2021; Wilch et al., 2021). This is evidenced by magmatism (dominantly alkaline), which began by ~37 Ma and continues into the present, with most occurring after ~14 Ma (Panter et al., 2021; Wilch et al., 2021). These magmatic rocks have a strong HIMU geochemical signature which is attributed to a plume source (Hart et al., 1997; Panter et al., 2000, 2021; Panter & Martin, 2023). Magmatism was accompanied by uplift of the Marie Byrd Land dome beginning by ~20 Ma (LeMasurier & Landis, 1996; Spiegel et al., 2016). Other evidence of a plume is provided by seismic imaging which shows a thin mantle transition zone beneath Marie Byrd Land (Emry et al., 2015) and slow seismic velocities spanning the upper and lower mantle suggesting elevated plume temperatures may extend down to the core mantle boundary (Hansen et al., 2014; Lloyd et al., 2015, 2020; Wiens et al., 2023).

Evidence of Cenozoic extension along the eastern flank of the WARS is limited. Examples include thin crust inferred from aerogravity in the Byrd Subglacial Basin and Pine Island Rift (Figure 3.2) (Jordan et al., 2010). Cenozoic extension is also inferred in nearby southeastern Marie Byrd Land on the basis of thermochronological evidence of rapid cooling and exhumation at ~30 Ma (Spiegel et al., 2016).

3.3. Methods

3.3.1. Overview

The geodynamic modeling code ASPECT (Advanced Solver for Planetary Evolution, Convection, and Tectonics) was used to simulate the structural, thermal, and magmatic evolution of the WARS. These models were utilized to test the melting of fusible lithologies in the lithosphere and asthenosphere to account for early syn-rift magmatism. ASPECT is a finite-element modeling code that solves the transient Stokes, continuity, and heat equations for the velocity, temperature, and pressure fields through time in a deforming Earth (Bangerth et al., 2024b, 2024a; Dannberg & Heister, 2016; Heister et al., 2017; Kronbichler et al., 2012). To test the various hypotheses for the origins of syn-rift WARS magmatism, new functionality was added to ASPECT to simulate melting of several new lithologies. The new additions combine the melting, freezing, and melt transport functionality currently in ASPECT with models having a rheologically layered Earth, where each layer deforms by ductile creep with a plastic limit. The modifications to ASPECT are described in detail below.

3.3.2. Description of ASPECT

ASPECT models begin with a user-defined model geometry, an initial temperature field, thermal and velocity boundary conditions, assigned rock compositions and corresponding material properties for each element. If an element straddles a compositional boundary, the material properties are averaged using the fractional abundance of each composition. If melting is included in the model, user-defined melting relations must also be given. ASPECT solves the momentum, continuity, heat, and advection equations to step the model forward through time, beginning with the user-defined initial geometry, composition field, thermal state, and boundary conditions. First, ASPECT solves the Stokes system for the pressure *P* and velocity fields *u*. If no melt is present, the momentum and continuity equations are solved using:

$$-\nabla \cdot \left[2\eta_s \left(\varepsilon(\boldsymbol{u}) - \frac{1}{3}(\nabla \cdot \boldsymbol{u})I\right)\right] + \nabla P = \rho g \,, \tag{1}$$

$$\nabla \cdot (\rho \boldsymbol{u}) = 0 \,, \tag{2}$$

where η_s is the shear viscosity (described below), $\varepsilon(u)$ is the strain rate, *g* is the acceleration due to gravity, ρ is the density, and *I* is the identity matrix. If melt is present in a cell, a modified form of the Stokes system is solved for the solid velocity u_s, compaction pressure P_c, and fluid pressure P_f (Dannberg & Heister, 2016):

$$-\nabla \cdot \left[2\eta_s \left(\varepsilon(\boldsymbol{u_s}) - \frac{1}{3}(\nabla \cdot \boldsymbol{u_s})I\right)\right] + \nabla P_f + \nabla P_c = \bar{\rho} g \,, \tag{3}$$

$$\begin{gathered} \nabla \cdot \boldsymbol{u_s} - \nabla \cdot K_D \nabla P_f - K_D \nabla P_f \cdot \frac{\nabla \rho_f}{\rho_f} = \\ -\nabla \cdot K_D \rho_f g + \Gamma\left(\frac{1}{\rho_f} - \frac{1}{\rho_s}\right) - \frac{\phi}{\rho_f} \boldsymbol{u_s} \cdot \nabla \rho_f - (\boldsymbol{u_s} \cdot g)(1-\phi)\beta_s \rho_s - K_D g \cdot \nabla \rho_f \,, \end{gathered} \tag{4}$$

$$\nabla \cdot \boldsymbol{u_s} + \frac{P_c}{\eta_b} = 0 \ , \qquad (5)$$

where η_s and η_b are the effective shear and bulk viscosities, ρ_f and ρ_s are the fluid and solid densities, $\overline{\rho}$ is the volumetric average of the solid and fluid densities, β_s is the solid compressibility constant, Γ is the melting rate, and ϕ is the melt fraction. Formulations for the viscosities and densities used in equations (1 – 5) are described in detail below and model constants are given in Tables 3.1 and 3.2. The Darcy coefficient K_D is:

$$K_D = \frac{k_\phi}{\eta_f} \ , \qquad (6)$$

and permeability k_ϕ is

$$k_\phi = k_0 \phi^3 (1-\phi)^2 \ , \qquad (7)$$

where melt viscosity η_f and reference permeability k_0 are user-defined constants. Melting and freezing are then computed according to the melting functions for the user-selected lithology.

Table 3.1. General Model Parameters

General Parameters	
Surface Temperature	0 °C
Basal Temperature (410 km)	1393 - 1453 °C
Mantle Potential Temperature	1270 - 1330 °C
Mantle Adiabatic Gradient	3×10^{-4} °C m^{-1}
Reference Temperature	20 °C
Reference Pressure	1×10^{5} Pa
Melt Parameters	
Reference Melt Density	2900 kg m^{-3}
Melt Viscosity	100 Pa s
Bulk Viscosity Constant	1
Reference Permeability	1×10^{-10} m^{2}
Melt Compressibility	5×10^{-11} Pa^{-1}
Melt Thermal Expansivity	3.1×10^{-5} °C^{-1}

Depletion Density Change	0 kg m^{-3}
Batch or Fractional Melting	Batch
Exponential Melt Weakening Factor	27
Approximation for the Fluid Pressure Gradient	Bulk Density
Entropy change due to melting	
Basalt	-240 J kg^{-1} $°C^{-1}$
Dry Lherzolite	-300 J kg^{-1} $°C^{-1}$
DMM	-300 J kg^{-1} $°C^{-1}$
MIX1G pyroxenite	-240 J kg^{-1} $°C^{-1}$
Mantle fraction for each lithology case	
Basalt	0.3
Dry Lherzolite	1
DMM	1
MIX1G pyroxenite	0.3
Viscosity / Strain Limits	
Minimum Strain Rate	1 x 10^{-20} s^{-1}
Minimum Viscosity	1 x 10^{18} Pa s
Maximum Viscosity	1 x 10^{26} Pa s

The temperature field is then updated to account for decompression, conduction, advection, and heat generation/absorption:

$$\frac{\partial T}{\partial t} = (H_r + H_s + H_a + H_l + \nabla \cdot k_T \nabla T)\frac{1}{\bar{\rho} C_p} - \boldsymbol{u} \cdot \nabla T\ , \tag{8}$$

where thermal conductivity k_T and specific heat capacity C_p are user-defined phase independent constants, t is time, and H_r is the volumetric radiogenic heat production. H_s, H_l, and H_a represent shear heating, latent heat, and adiabatic heat changes, respectively. The form of H_s, H_l, H_r, and H_a are decided by the user. In ASPECT, the user either provides functions for these terms or selects from a library of existing formulations and must define the corresponding constants. The heating terms used in the WARS models are described below in the Model Description section.

Table 3.2. Model Layer Parameters

Variable	Upper Crust	Lower Crust	Lithospheric Mantle	Asthenosphere
Constant Heat Production Rate (W m^{-3})	1.5×10^{-6} (Cratonic Domain) 2.0×10^{-6} (Accreted Domain)	-	-	-
Thermal Conductivity (W m^{-1} $°C^{-1}$)	2.5	2.5	3.4	3.4
Specific Heat (J kg^{-1} $°C^{-1}$)	875	875	1250	1250
Reference Density (kg m^{-3})	2850	2850	3300	3300
Thermal Expansivity Coefficient ($°C^{-1}$)	3.1×10^{-5}	3.1×10^{-5}	3.1×10^{-5}	3.1×10^{-5}
Compressibility (Pa^{-1})	5×10^{-12}	5×10^{-12}	5×10^{-12}	5×10^{-12}
Plasticity Parameters[a]				
Angle of Internal Friction (degrees)	23	23	23	23
Cohesion (Pa)	6.5×10^{7}	6.5×10^{7}	6.5×10^{7}	6.5×10^{7}
Rheologies	Diorite[a]	Diorite[a]	Dunite[a]	Lherzolite[b]
Prefactor for Creep	5×10^{-18} Pa^{-1} s^{-1}	5×10^{-18} Pa^{-1} s^{-1}	4×10^{-25} Pa^{-1} s^{-1}	1.2×10^{-15} Pa^{-1} m^{m} s^{-1}
Stress Exponent	2.4	2.4	4.5	1
Grain Size Exponent	-	-	-	3
Grain Size (m)	-	-	-	0.01
Activation Energy (J mol^{-1})	2.19×10^{5}	2.19×10^{5}	4.98×10^{5}	3.70×10^{5}
Activation Volume (m^{3} mol^{-1})	0	0	0	0

[a](Harry et al., 2018; Carter & Tsenn, 1987; Ranalli & Murphy, 1987)
[b](Karato, 2013; Zimmerman & Kohlstedt, 2004)

The rock composition of each element is updated by advecting the composition and melt fields (if present). The advection equation for the composition field is:

$$\frac{\partial c_i}{\partial t} + \boldsymbol{u} \cdot \nabla c_i = q_i \,, \tag{9}$$

where *c* is the volume fraction of composition *i* and q_i is the reaction (e.g., melting/solidification) rate. The advection equation for the volume fraction of melt is:

$$\frac{\partial \phi}{\partial t} + \boldsymbol{u_s} \cdot \nabla \phi = \frac{\Gamma}{\rho_s} + (1 - \phi)(\nabla \cdot \boldsymbol{u_s} + \beta_s \rho_s g \cdot \boldsymbol{u_s})\,. \tag{10}$$

3.3.3. Modifications to ASPECT

To simulate melting of a compositionally heterogeneous mantle, ASPECT (2.6.0-pre) was modified by adding: i) an expanded variety of lithologies available for melt computations, ii) the ability to compute melting in a rheologically heterogeneous model, and iii) a linear pressure dependence in the density formulation. New solidi, liquidi, and melting functions were added into ASPECT (see Appendix A of Mayle & Harry, 2023) for basalt (Harry & Leeman, 1995; Mayle & Harry, 2023), MIX1G pyroxenite (Hirschmann et al., 2003), and depleted MORB mantle (DMM) (Brown & Lesher, 2016). The melt fraction is calculated in the model using the melting relations for one chosen lithology. The ASPECT modifications to the melting calculations allow users to specify the fractional abundance of this lithology prior to modeling. This is applied to all elements in the model. Melt fraction in each element is computed using the modeled P-T conditions applied to the melting relations of the chosen lithology. Then melt fraction is scaled by the fractional abundance specified for the lithology. It is possible that the starting (pre-rift) geotherm lies above the solidus of a given lithology. Thus, functionality was added to ASPECT to scale the starting fractional abundance accordingly.

The new additions to ASPECT also allow melting to be evaluated in Earth models which obey flow laws where viscosity is temperature, pressure, melt fraction, and strain rate dependent. Prior to these modifications, viscosity in ASPECT models which permit melting was only dependent on temperature and melt fraction. With the new modifications, the maximum viscosity in these models can also be limited by a pressure-dependent plastic yield stress. These additions to ASPECT impact the viscosity terms in the Stokes system. Viscous behavior in the model is governed by power law creep:

$$\eta_0 = \frac{1}{2} A^{-\frac{1}{n}} d^{\frac{m}{n}} \dot{\varepsilon}_{II}^{\frac{1-n}{n}} \exp\left(\frac{E + PV}{nRT}\right), \tag{11}$$

where η_0 is the intrinsic viscosity, d is the grain size, $\dot{\varepsilon}_{II}$ is the second invariant of the deviatoric strain rate tensor, E is the activation energy, V is the activation volume, R is the gas exponent, and A, n, and m are empirically determined constants. If no melt is present, the shear viscosity in equation (1) is equal to the intrinsic viscosity:

$$\eta_s = \eta_0 \, . \tag{12}$$

If melt is present, both the shear and bulk viscosities are needed. The shear viscosity is determined by modifying the intrinsic viscosity for the presence of melt (Dannberg & Heister, 2016; Keller et al., 2013):

$$\eta_s = \eta_0 \exp(-a\phi) \, , \tag{13}$$

where a is the exponential melt weakening constant. The bulk viscosity is only needed when melt is present and is calculated using the intrinsic viscosity (Dannberg & Heister, 2016; Keller et al., 2013):

$$\eta_b = \eta_0 \frac{c_b}{\phi} \, , \tag{14}$$

where c_b is the bulk viscosity constant. Regardless of whether melt is present or not, a plastic limit is placed on the maximum shear stress σ_s (Bangerth et al., 2024a; Gerya, 2019):

$$\sigma_s = 2\eta_s \dot{\varepsilon}_{II} \leq \sigma_y \; . \tag{15}$$

Yield stress σ_y is defined using the Drucker Praeger plastic yield criterion:

$$\sigma_y = C\cos(\theta) + P\sin(\theta) \, , \tag{16}$$

where C is the cohesion and ϑ is the internal friction angle. Shear viscosity is limited by the yield stress:

$$\eta_s \leq \frac{\sigma_y}{2\dot{\varepsilon}_{II}} \; . \tag{17}$$

A similar limit is placed on the bulk viscosity.

For the models shown in this work, new solid and melt density formulations were added to ASPECT that describe a linear relationship between density and pressure/temperature (Gerya, 2019):

$$\rho_s = \left(\rho_{sref} + (\Delta\rho_d * \gamma)\right) * \left(1 - \left(T - T_{ref}\right)\alpha\right) * \left(1 + \left(P - P_{ref}\right)\beta_s\right) , \tag{18}$$

$$\rho_f = \rho_{fref} * \left(1 - \left(T - T_{ref}\right)\alpha\right) * \left(1 + \left(P - P_{ref}\right)\beta_f\right), \qquad (19)$$

where γ is the volume fraction of rock that has been depleted (if positive) or enriched (if negative) by melting and/or freezing. The user-defined parameters are the densities of the solid ρ_{sref} and fluid ρ_{fref} at the reference temperature T_{ref} and reference pressure P_{ref}, the melt and solid compressibility constants β_f and β_s, the thermal expansivity constant (taken to be the same for both solid and fluid phases) α, and the density change per fraction depletion or enrichment $\Delta\rho_d$.

3.4. Model description

3.4.1. Model geometry and boundary conditions

The WARS models developed for this study are similar to those of Harry et al. (2018) and Huerta and Harry (2007) which replicate the WARS structural evolution (Tables 3.1 and 3.2). Unlike these previous models, the WARS models presented here include both the lithosphere and asthenosphere. The WARS ASPECT models shown here use a two-dimensional (2D) rectangular geometry which is 1500 km wide and extends to a depth of 410 km (Figure 3.4). The initial meshes for the WARS models are generated by ASPECT and consist of ~13,500 - 23,000 rectangular elements. ASPECT's initial adaptive mesh refinement is utilized to coarsen and refine the mesh based on estimated errors in the temperature and velocity fields (Bangerth et al., 2024a). WARS models with higher temperatures result in initial meshes with more elements. Mantle potential temperatures are varied in the WARS models (ranging between T_p of 1270 °C and 1330 °C) as described in detail in the Model Setup section. The largest elements in the initial meshes have dimensions of ~3 km by 12 km and the smallest have dimensions of ~1 km by 3 km. Through time ASPECT continues to refine and coarsen the mesh using adaptive mesh refinement.

The WARS models consist of four layers (Table 3.2): upper crust, lower crust, lithospheric mantle, and asthenosphere. The corresponding layer thicknesses in the cratonic domain (East Antarctica) are 30 km and 9 km for the upper and lower crust and 141 km for the lithospheric mantle. In the accreted

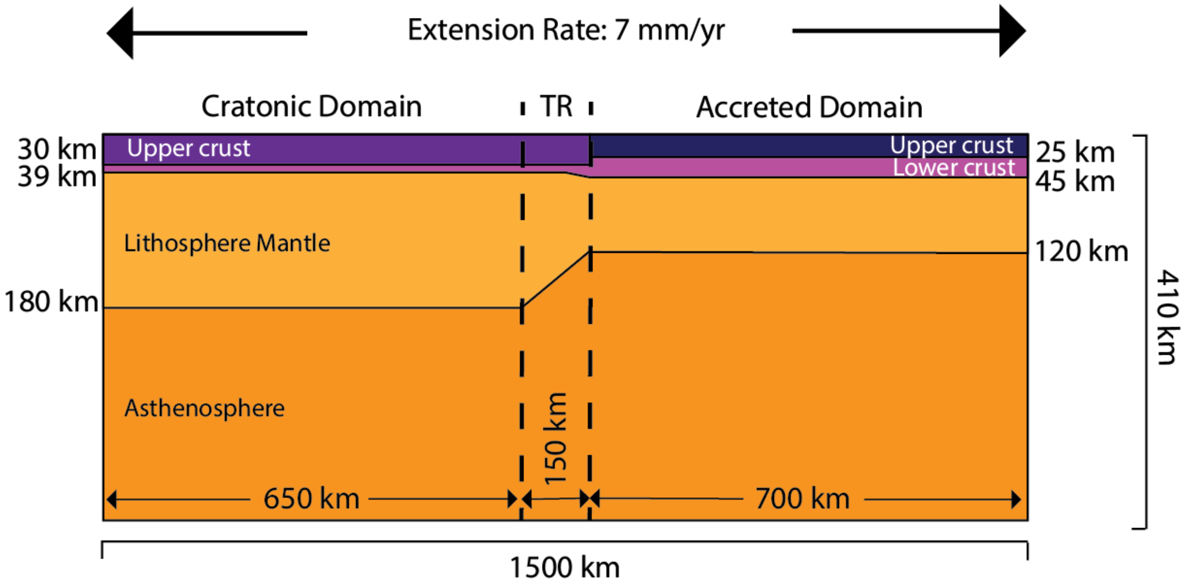

Figure 3.4. Initial model geometries across the cratonic domain (analogous to East Antarctica) and the accreted domain (analogous to West Antarctica). Transitional region (TR) connecting lithosphere of the cratonic and accreted domains is 150 km wide. Lower crustal ramp connecting the crust of the cratonic and accreted domains is 60 km wide.

domain (West Antarctica) the corresponding layer thicknesses are 25 km, 20 km, and 75 km, respectively. The cratonic and accreted domains of the model are connected by a 60 km-wide region of transitional crust thickness overlaying a 150 km-wide region of transitional mantle lithosphere thickness. For the crust (upper and lower) and lithospheric mantle, dislocation creep flow laws for dry diorite and dry dunite, respectively, are used (Carter & Tsenn, 1987; Harry et al., 2018; Ranalli & Murphy, 1987). For the asthenosphere, a dry lherzolite diffusion creep flow law is utilized (Karato, 2013; Zimmerman & Kohlstedt, 2004). After Huerta and Harry (2007) and Harry et al. (2018), extension is simulated by applying a horizontal outflow velocity boundary condition of 3.5 mm yr^{-1} at each side of the model for a total extension rate of 7 mm yr^{-1}. This extension rate is consistent with estimates of total extension (600 – 1000 km) from the WARS over 100 m.y. (e.g., Siddoway, 2008 and discussion in Section 3.2.2.). A vertical inflow velocity boundary condition is applied at the base of the model to balance horizontal outflow. Thermal boundary conditions include a surface temperature prescribed to be 0 °C and a basal temperature which is determined from the mantle adiabat as described below.

3.4.2. Thermal parameters

Thermal processes considered in the WARS models include radiogenic heat production in the upper crust, adiabatic temperature changes, and latent heat consumed or released during melting/freezing (equation 8). Heat production in the upper crust is assigned a constant heat production rate of $H_r = 1.5 \times 10^{-6}$ W m^{-3} in the cratonic domain and $H_r = 2 \times 10^{-6}$ W m^{-3} in the accreted domain. These heat production values follow Huerta and Harry (2007) and Harry et al. (2018), which were adopted for their consistency with surface heat flow estimates from the WARS. Radiogenic heat production in the lower crust, lithospheric mantle, and asthenosphere are prescribed to be zero. Adiabatic heating is calculated using:

$$H_a = \alpha T((1-\phi)\boldsymbol{u_s} \cdot \nabla P) + \alpha T(\phi \boldsymbol{u_f} \cdot \nabla P), \tag{20}$$

where u_f is the melt velocity (Bangerth et al., 2024a). Latent heat released or absorbed is given by:

$$H_l = \rho T \Delta S \left(\frac{\partial \phi}{\partial t} + \boldsymbol{u_s} \cdot \nabla \phi\right), \tag{21}$$

where ΔS is the user-defined entropy change due to melting or freezing (Bangerth et al., 2024a).

3.4.3. Pre-rift thermal state

To create a 2D pre-rift thermal model, temperatures at layer interfaces were initially specified for a series of one-dimensional (1D) steady-state profiles spaced 1 km apart across the width of the model. The temperatures between the interfaces were then interpolated in ASPECT onto a 2D mesh. Using the interpolated 2D initial temperature field as the starting thermal state, ASPECT was then run without extension to allow the model to reach thermal and isostatic equilibrium. The resulting temperature field is taken to be the pre-rift thermal state which was used as the starting thermal condition for the extending WARS models.

In the initial 1D steady-state temperature profiles, asthenosphere temperatures are assumed to follow a linear adiabat:

$$T(z) = T_p + G_a * z\,, \qquad z \geq Z_l \tag{22}$$

where G_a is the mantle adiabatic gradient, T_p is the mantle potential temperature, z is depth, and Z_l is the depth to the base of the lithosphere. Lithosphere temperatures follow the steady-state 1-D heat equation for a multi-layer lithosphere after Hasterok & Chapman (2011) where the temperature T_{i+1} and heat flow q_{i+1} at the base of a layer is given by:

$$T_{i+1} = T_i + \frac{q_i}{k_i}\Delta z_i - \frac{H_{ri}\Delta {z_i}^2}{2k_i}\,, \qquad z < Z_l \tag{23}$$

where T_i and q_i are the temperature and heat flow at the top of a layer, respectively, and k_i, Δz_i, and H_{ri} are the thermal conductivity, thickness, and radiogenic heat production of the layer. The indices i correspond to one of three lithosphere layers: upper crust, lower crust, or lithosphere mantle. Radiogenic heat production is zero in all layers except the upper crust. To solve for temperatures at each layer boundary for every 1D steady-state profile, equation (23) was expanded for temperature at each interface. The equations for the interfaces were then combined to recast in terms of surface temperature T_1 and temperature at the base of the lithosphere T_4. The resulting equation is then rearranged to solve for surface heat flow q_1:

$$q_1 = \frac{T_4 - T_1 + H_{r1}\Delta z_1\left(\frac{\Delta z_1}{2k_1} + \frac{\Delta z_2}{k_2} + \frac{\Delta z_3}{k_3}\right)}{\frac{\Delta z_1}{k_1} + \frac{\Delta z_2}{k_2} + \frac{\Delta z_3}{k_3}}, \tag{24}$$

where surface temperature (T_1) is assigned by the user and T_4 is defined by the adiabatic gradient (equation 22). Once surface heat flow was known for a given 1D profile, the temperature at each lithosphere layer interface was calculated.

The temperatures between the layer interfaces of the 1D steady state profiles were then interpolated onto the initial 2D mesh in ASPECT and used as an initial condition. ASPECT was then run with no extension (no inflow or outflow velocity boundary conditions) until the model reached 2D steady-state conditions. Steady-state conditions were assumed when the maximum velocity in the initial model was < 1 mm yr^{-1}. After initial pressure and temperature conditions were determined, the compositional model was adjusted. This is necessary if the user-defined lithological model contains fractional abundances that are above the respective solidus in parts of the model.

3.5. Model setup

Five separate model suites were constructed to test melting of different mantle source rock compositions. The models have the same rheological structure, differing only in their melting relations. The five model suites simulate melting for mantle composed of: i) 100% depleted lherzolite (DMM) (Brown & Lesher, 2016), ii) 100% fertile lherzolite (pyrolite composition) (Dannberg & Heister, 2016; Katz et al., 2003), iii) 30% pyroxenite (Hirschmann et al., 2003) and 70% peridotite, iv) 30% basalt (Harry & Leeman, 1995; Mayle & Harry, 2023) and 70% peridotite, and v) a reference model where no melting was permitted. ASPECT currently permits evaluating the melting of only one composition in a given simulation. Consequently, in the models containing 70% peridotite, melting was evaluated only for the more fertile (less abundant) composition. All models were assigned the same initial conditions (described in detail above in the Model Description section) except for the temperature. Each of the five model suites were evaluated with three different mantle potential temperatures: i) T_p = 1270 °C, taken to represent a cold mantle case, ii) T_p = 1300 °C, taken to represent a cool mantle case, and iii) T_p = 1330 °C, taken to represent a warm mantle case. This spans the range of mantle temperatures found to best reproduce the WARS structural evolution in previous geodynamic modeling studies (Bialas et al., 2007; Harry et al., 2018; Huerta & Harry, 2007; van Wijk et al., 2008). As noted in those papers, these temperatures are relatively cool compared to global ambient mantle potential temperatures which typically range from 1300 – 1400 °C and average ~1350 °C (Herzberg et al., 2007; Katsura, 2022; Lee et al., 2009).

3.6. Results

3.6.1. Structural evolution

The models were run to simulate 100 m.y. of extension, corresponding to the Late Cretaceous to present period of WARS extension. All models produce a similar structural evolution regardless of whether or not melting is included in the simulation. These models undergo two major rift stages: an initial stage in which rifting is broadly distributed throughout the WARS region (Stage 1: 0 – 50 m.y.) followed by a stage in which rifting is more narrowly focused along the margins of the WARS (Stage 2: 50 – 100 m.y.) (Figures 3.5 – 3.7). The broad rifting stage (Stage 1) can be separated into two substages: Substage 1A (0 – 10 m.y.) and Substage 1B (10 – 50 m.y.). Substage 1A is characterized by broad extension throughout the lithosphere across the breath of the accreted domain that forms the West Antarctic side of the model. In Substage 1B, extension and thus lithosphere thinning begins to concentrate in the western one-third of the accreted domain (Zone 1 in Figures 3.5c, 3.6c, and 3.7c) and easternmost part of the transitional lithosphere between the cratonic and accreted domains and begins to wane across the remainder of the accreted domain. The narrow rifting stage (Stage 2) can also be broken into two substages: Substage 2A (50 – 65 m.y.) and Substage 2B (65 – 100 m.y). In Substage 2A, strain continues to become more tightly focused along the western and eastern margins of Zone 1 (Zones 1a and 1c, respectively, in Figures 3.5d, 3.6d, and 3.7d) and begins to wane in the interior (Zone 1b in Figures 3.5d, 3.6d, and 3.7d). Strain continues to wane in the remainder of the accreted domain east of Zone 1. In Substage 2B, extension shuts down throughout the lithosphere of the accreted domain and concentrates in an emerging neck (Zone 1a in Figures 3.5e, 3.6e, and 3.7e) located in the transitional lithosphere along the eastern margin of the cratonic domain. The broad and narrow rift stages (and substages) are described in more detail below.

3.6.1.1. Broad Rifting

3.6.1.1.1. Substage 1A (0 – 10 m.y.)

During Substage 1A (Figure 3.5a – 3.5b, Figure 3.6a – 3.6b, Figure 3.7a – 3.7b), extension is accommodated by uniform stretching of the crust throughout the accreted domain from 0 – 2 m.y. of extension. After 2 m.y., a horst-and-graben style of deformation begins to develop in the crust of the western one-third of the accreted domain closest to the cratonic domain, with ~20 km wide zones of low strain rate bounded by narrow shear bands dipping at angles of ~45° similar to the Basin and Range style of extension in the western U.S. (Stewart, 1971; Wernicke, 1992). This style of extension becomes progressively more prevalent throughout the crust in the western half of the accreted domain from 2 – 10 m.y. For the duration of Substage 1A, the lithosphere mantle of the accreted domain is uniformly extended.

The crust and lithosphere mantle of the cratonic domain is largely unextended in Substage 1A. There are two exceptions. The first occurs within the transitional lithosphere adjacent to the boundary with the accreted domain. Here, strain begins to focus throughout the crust and lithosphere mantle at the onset of extension and becomes progressively more focused with continued extension. The second occurs in the lowermost lithosphere in the eastern half of the cratonic domain. Here, high strain rates associated with shearing occur throughout Substage 1A. In the warm model, these high strain rates are concentrated in a relatively narrow band near the base of the lithosphere in the transitional region.

In the asthenosphere, an upwelling forms at the onset of extension and becomes better established throughout Substage 1A. The main axis of the upwelling is located under the center of the extending accreted domain. Upwelling asthenosphere flow from the bottom of the model merges with the outward flow along the left and right edges of the model.

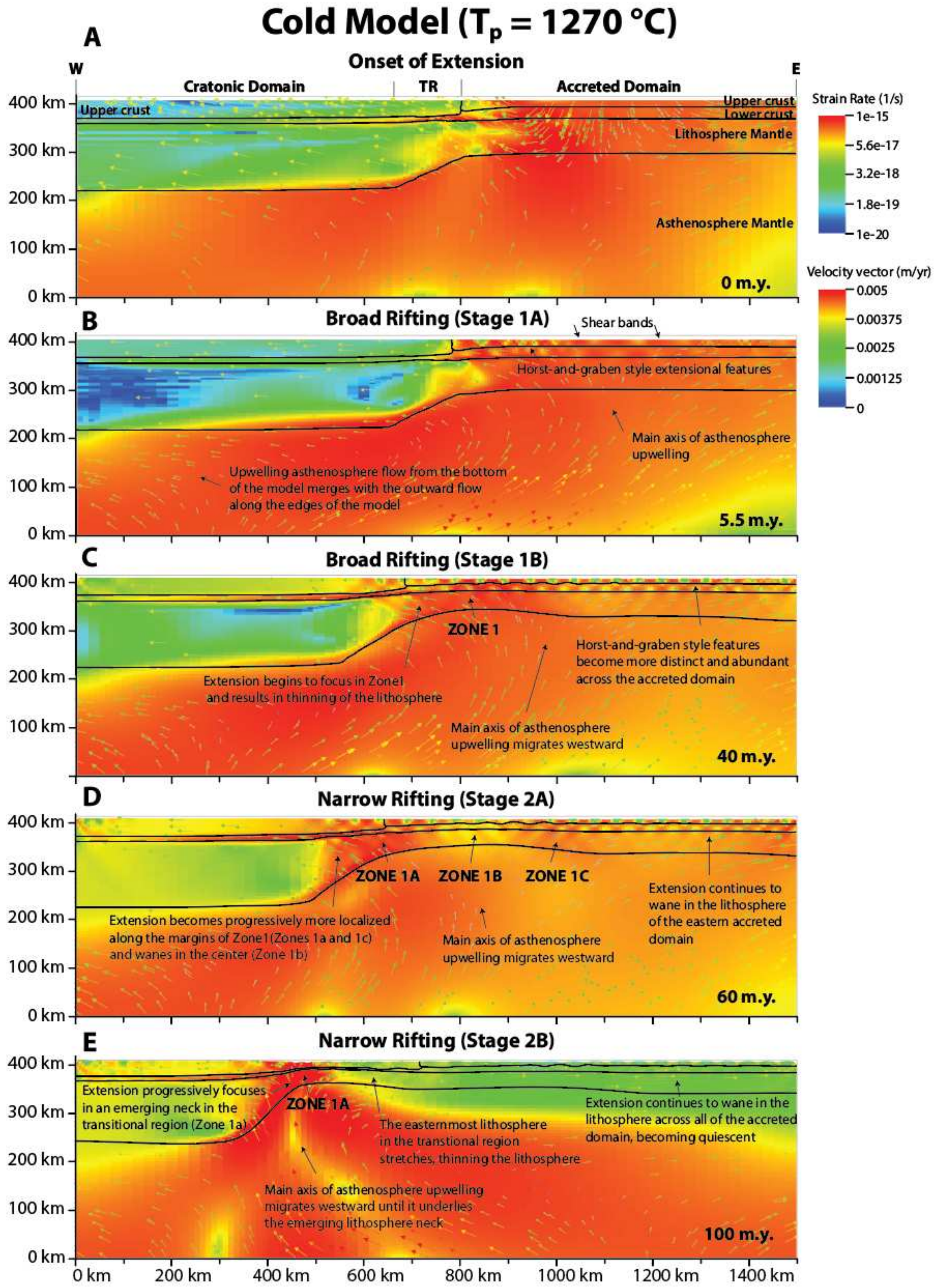

Figure 3.5. Structural evolution of the cold model (T_p = 1270 °C). Results are shown at times that best characterize the structural stage: (A) onset of extension, (B) Substage 1A, (C) Substage 1B, (D) Substage 2A, and (E) Substage 2B. The background colors indicate strain rate and the colors and size of the vectors indicate velocity.

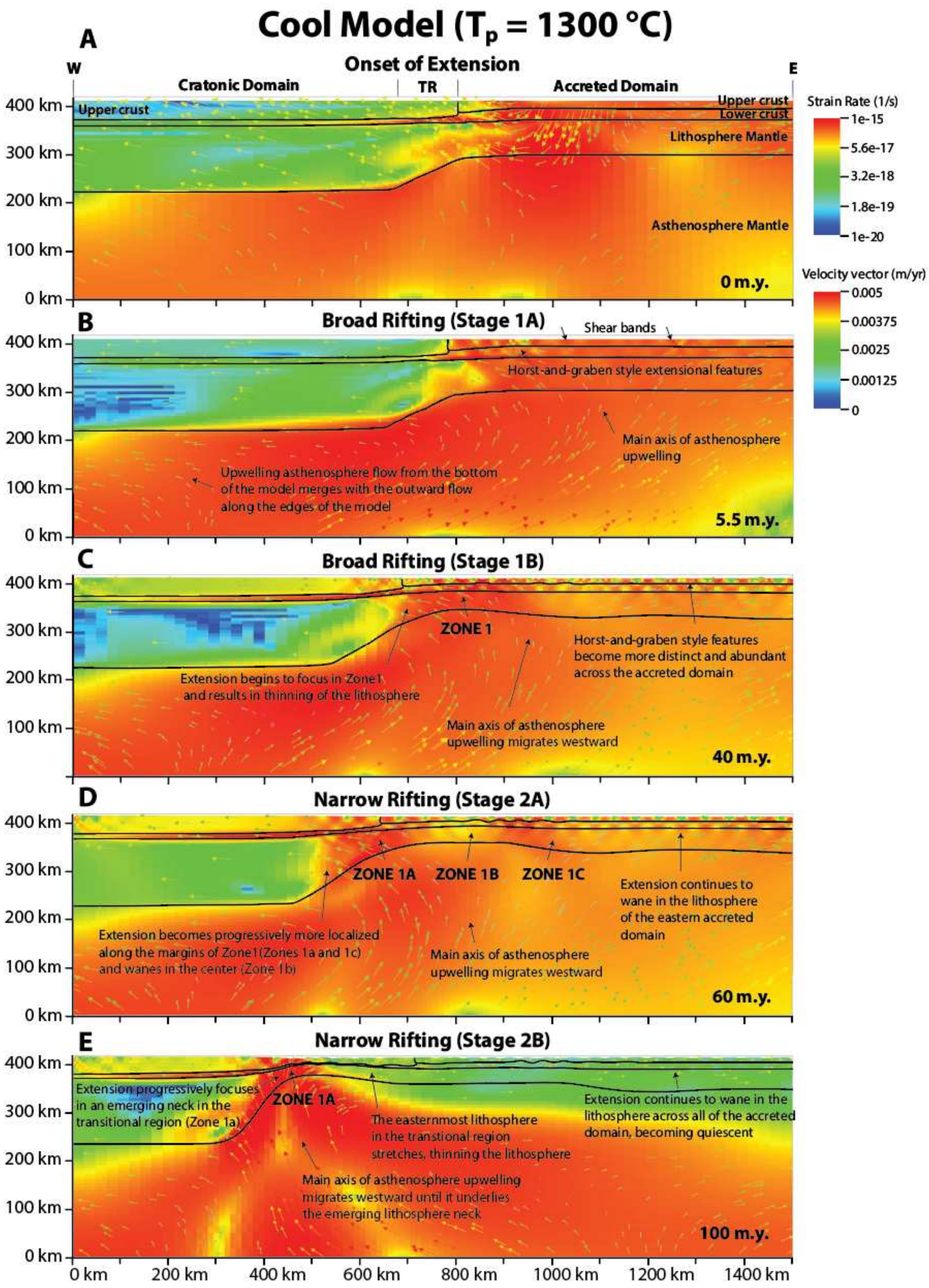

Figure 3.6. Structural evolution of the cool model (T_p = 1300 °C). See description of Figure 3.5.

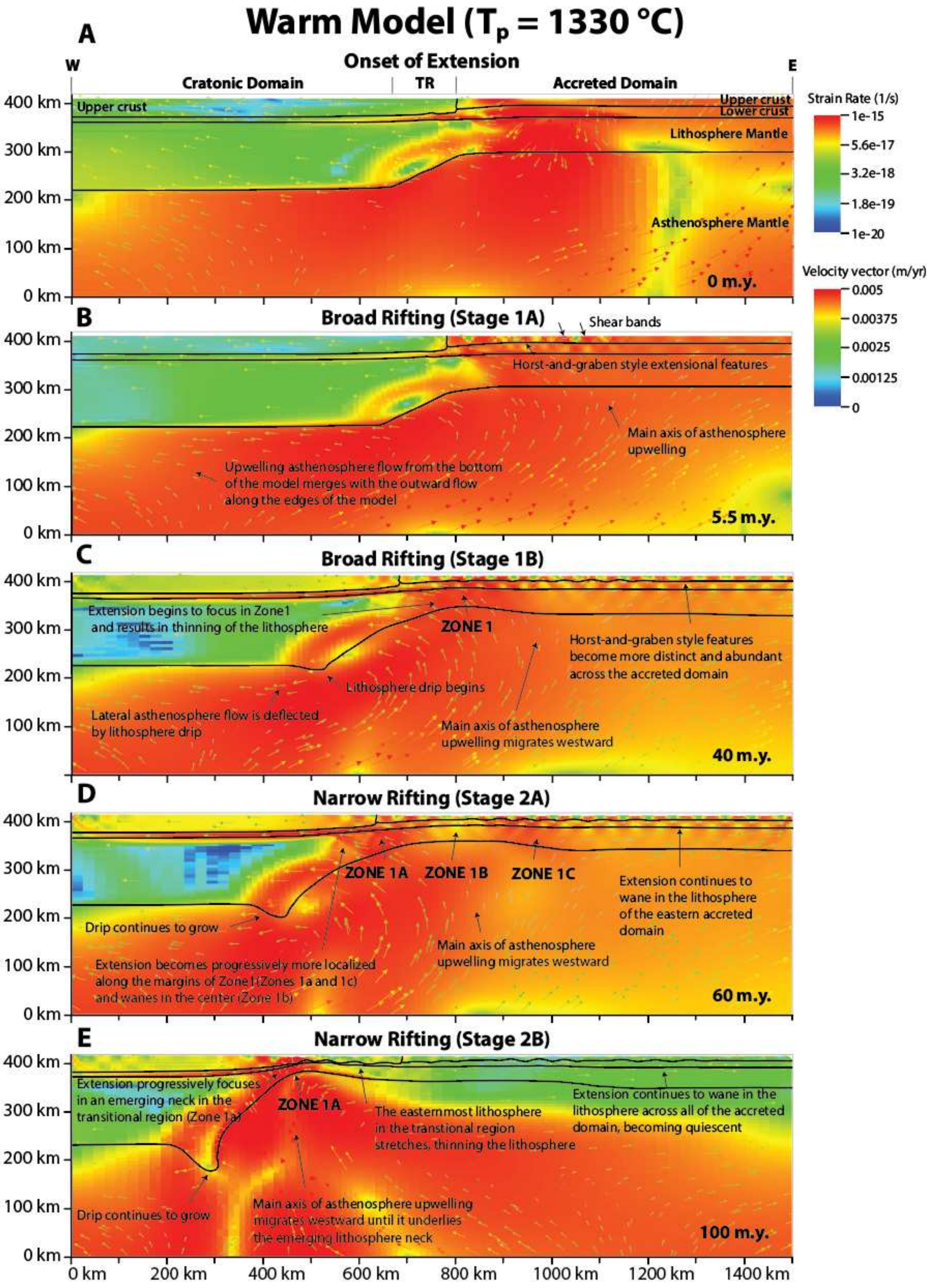

Figure 3.7. Structural evolution of the warm model (T_p = 1330 °C). See description of Figure 3.5.

3.6.1.1.2. Substage 1B (10 – 50 m.y.)

Throughout Substage 1B (Figures 3.5c, 3.6c, and 3.7c), extension of the lithosphere becomes progressively more focused in the western one-third (~250 km wide) of the accreted domain and easternmost part of the transitional lithosphere closest to the cratonic domain (Zone 1 in Figures 3.5c, 3.6c, and 3.7c) and begins to wane across the remainder of the accreted domain. Horst-and-graben style extensional features in the crust described in Substage 1A become progressively more defined and abundant across the broader accreted domain in this substage.

The crust in the cratonic domain begins to extend and continues to accommodate strain throughout Substage 1B. However, crustal strain rates in this part of the model are ~1 to 2 orders of magnitude lower than those in the accreted domain. Crustal strain rates are greatest in the transitional region adjacent to the accreted domain and decrease to the west. The horst-and-graben style structures that began to develop in the crust of the accreted domain during Substage 1A expand into the transitional region. A horizontal shear zone forms at the base of the crust spanning the cratonic domain and becomes better developed as Substage 1B proceeds. The lithosphere mantle beneath the cratonic domain remains relatively unextended during Substage 1B. An exception occurs in the transitional region (eastern part of Zone 1) where extensional strain that began to develop during Substage 1A continues to be accommodated. In the warm model, the lowermost lithosphere in the transitional region begins to form a slight drip after ~40 m.y. of extension.

The asthenosphere flow pattern established in Substage 1A continues to evolve throughout Substage 1B. The main axis of upwelling begins to migrate westward, such that the axis underlies the easternmost margin of Zone 1 by 50 m.y. In the warm model, the developing drip of the lowermost lithosphere in the transitional region slightly deflects the local lateral flow in the uppermost asthenosphere, introducing a downward component.

3.6.1.2. Narrow Rifting

3.6.1.2.1. Substage 2A (50 – 65 m.y.)

During Substage 2A (Figures 3.5d, 3.6d, and 3.7d), strain in the lithosphere becomes progressively more localized along the western and eastern margins of Zone 1 (Zones 1a and 1c, respectively, in Figures 3.5d, 3.6d, and 3.7d) and wanes in the interior (Zone 1b in Figures 3.5d, 3.6d, and 3.7d). During this time, extension in the remainder of the accreted domain further to the east continues to wane.

In the cratonic domain, strain rates in the crust slightly increase during Substage 2A but remain ~1 to 2 orders of magnitude lower than in the crust of the accreted domain. Crustal strain rates remain highest in the transitional region near the boundary with the accreted domain. An exception is the lower crustal shear zone spanning the cratonic domain that formed in Substage 1B, which continues to accommodate strain for the duration of Substage 2A. The highest strain rates in the lithosphere mantle of the cratonic domain occur in the transitional region adjacent to the boundary with the accreted domain. In the warm model, the mantle drip at the base of the lithosphere continues to grow.

The asthenosphere flow pattern established in Substage 1B continues throughout Substage 2A. The main axis of upwelling continues to migrate westward, until it underlies Zone 1b by 65 m.y. In the warm model, the lateral upper asthenosphere flow under the cratonic domain continues to be perturbed by the drip in the lowermost lithosphere underlying the transitional region which continues to deflect local lateral asthenosphere flow.

3.6.1.2.2. Substage 2B (65 – 100 m.y.)

Throughout Substage 2B (Figures 3.5e, 3.6e, and 3.7e), extensional strain rates progressively decrease in the lithosphere of the accreted domain and focus in an emerging neck forming in the transitional region. During this substage, the transitional lithosphere adjacent to the boundary with the accreted domain stretches, thinning the lithosphere. After 100 m.y. of modeled extension, the lithosphere of the accreted domain is quiescent while strain rates are concentrated in a narrow region (~100 km wide) of the transitional lithosphere located ~200 km west of the accreted-cratonic domain boundary (Zone 1a in Figures 3.5e, 3.6e, and 3.7e). The drip in the lowermost lithosphere under the transitional region continues to grow and descends further into the asthenosphere in the warm model.

The asthenosphere flow pattern established in Substage 2A continues until the end of modeled extension at 100 m.y. The main axis of upwelling in the asthenosphere migrates further westward during Stage 2B until it underlies the emerging lithospheric neck in the transitional region (Zone 1a) after 70 m.y. of extension. The main axis of upwelling remains under the neck until the end of modeled extension. In the warm model, the drip of the delaminating lithosphere underlying the transitional region continues to deflect flow in the uppermost asthenosphere.

3.6.2. Magmatic evolution

Of the tested protolith lithologies only basalt melted during extension, regardless of the model mantle potential temperature (1270 °C ≤ T_p ≤ 1330 °C). All models evaluating melting of basalt have similar magmatic histories which strongly correlate with the structural evolution. In general, melt accumulates in a thin layer spanning the breadth of the accreted domain during the early stages of rifting. In the middle stages of rifting, melting becomes more intense (higher melt percents) and takes place over a thicker portion of the upper asthenosphere beneath the western part of the accreted domain (Zone 1) and wanes under the eastern part. In the later stages of rifting, melt becomes progressively more concentrated under an emerging lithosphere neck in the transitional region (Zone 1a) as lithospheric thinning becomes more focused. In all of the models, melt quenches in the uppermost asthenosphere and thus does not make it to the surface. We note that higher permeabilities than tested in these models may permit melt to ascend more quickly through the mantle and thus reach the surface. This is discussed further in Section 3.7.3.2. below.

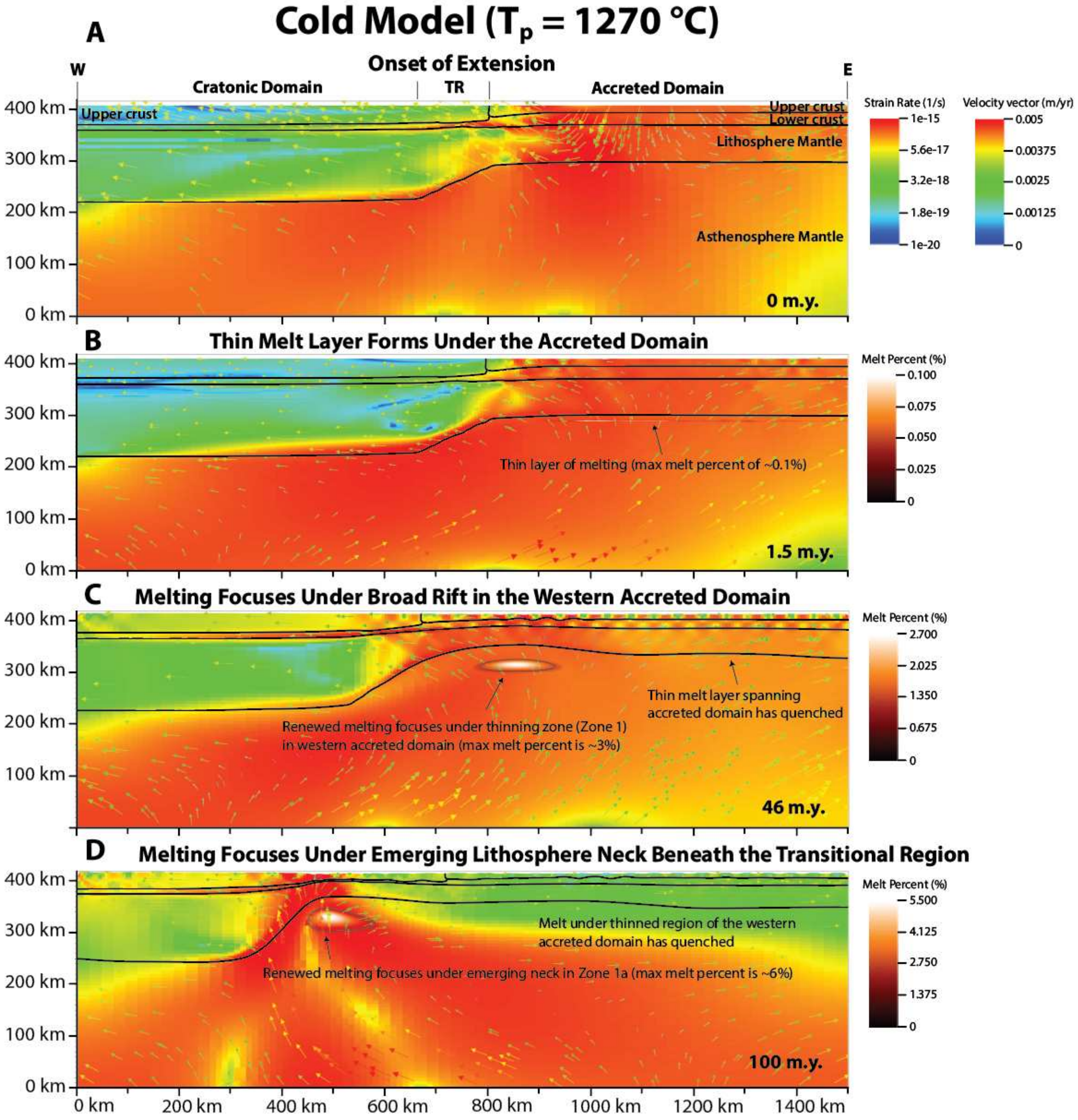

Figure 3.8. Magmatic evolution of the cold model (T_p = 1270 °C). Results are shown at times that best characterize the magmatic evolution: (A) onset of extension, (B) the thin melt layer forms under the accreted domain during early rifting, (C) melting focuses under the broad rift in the western accreted domain during middle rifting, and (D) melting focuses under the emerging lithosphere neck beneath the eastern cratonic domain during late rifting. The background colors indicate strain rate and the colors and size of the vectors indicate velocity. Black line surrounding melt is the 1% melt contour. Transitional region (TR). Note that the melt percent scale is different in each panel to show where melt

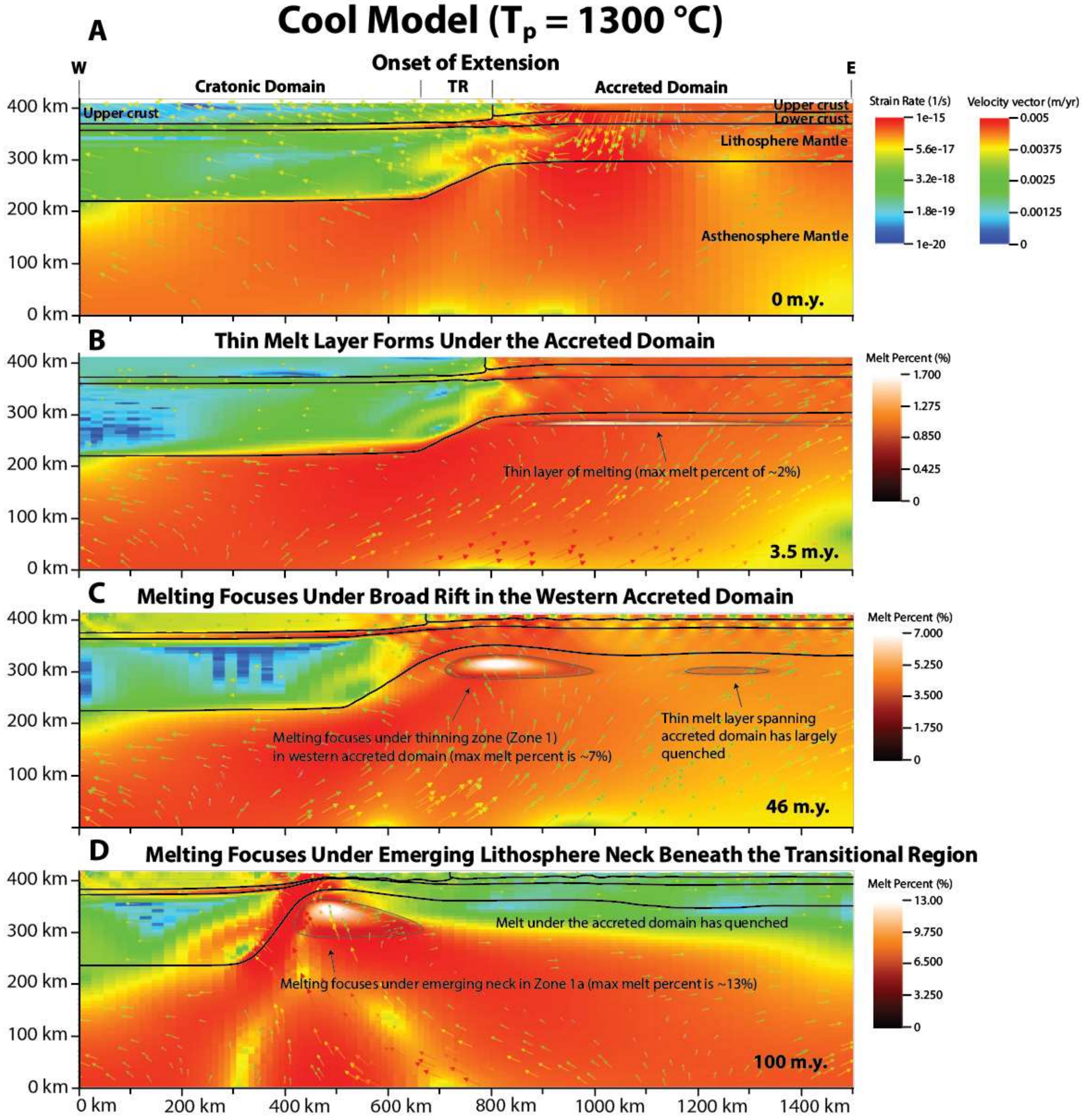

Figure 3.9. Magmatic evolution of the cool model (T_p = 1300 °C). See description of Figure 3.8.is most concentrated.

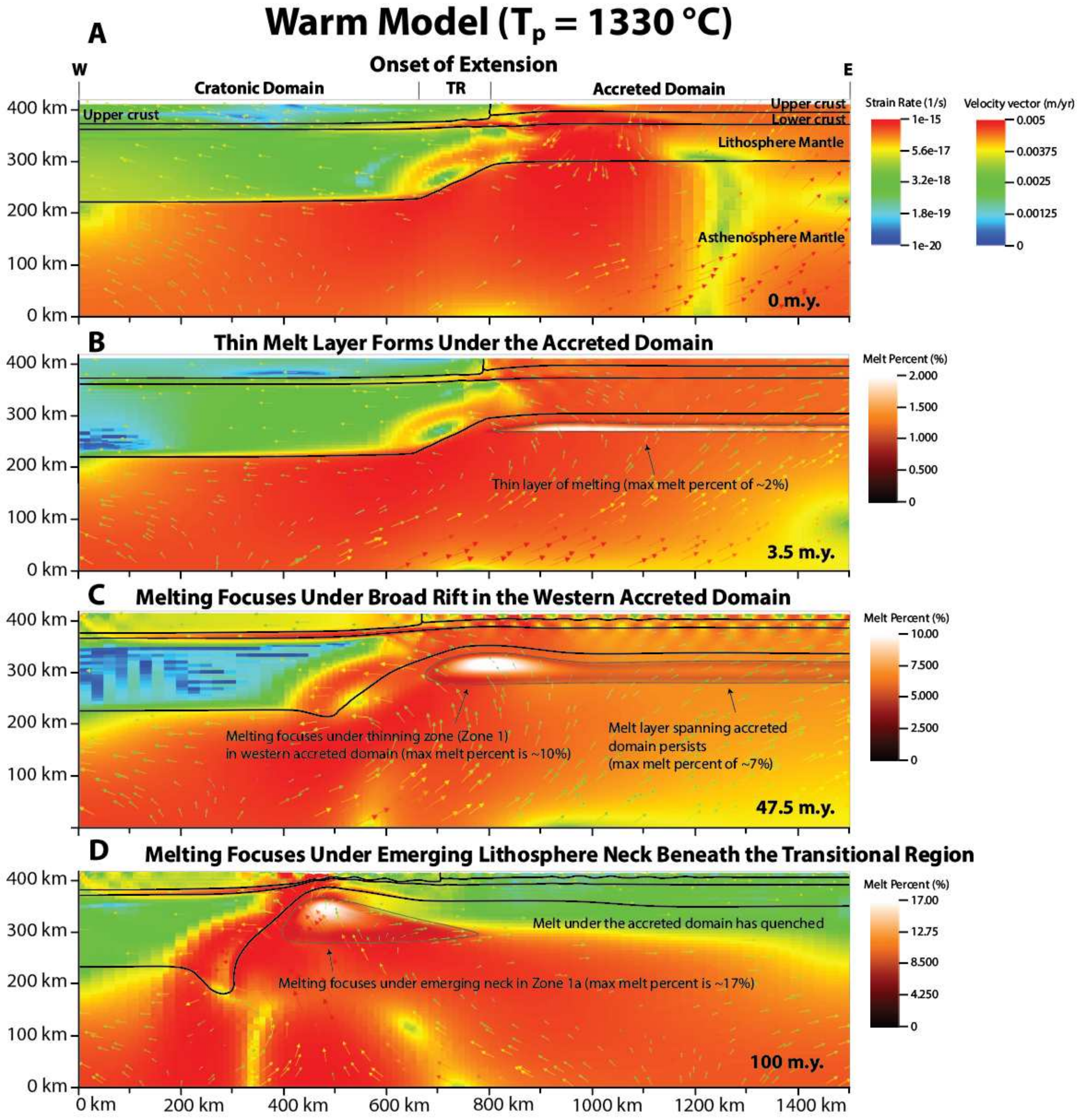

Figure 3.10. Magmatic evolution of the warm model (T_p = 1330 °C). See description of Figure 3.8.

3.6.2.1. Early rifting – Thin melt layer forms under the accreted domain

Basalt protoliths begin to melt during Substage 1A at or near the onset of extension (< 0.025 m.y. of modeled extension) at all evaluated temperatures. Initial melting occurs in a thin layer in the upper asthenosphere spanning the breadth of the extending accreted domain (Figures 3.8a – 3.8b, 3.9a –3.9b, 3.10a – 3.10b). The top of this partially molten layer is initially ~10 km below the base of the lithosphere. Generally, the thickness of the melt layer and melt percents progressively increase as the lithosphere across the accreted domain extends. The maximum melt percents in this melt layer and the time after the onset of extension at which these percents are achieved in the cold, cool, and warm models are < 1% by 3 m.y., ~3% by 21 m.y., and ~7% by 34 m.y., respectively. At these respective times, the melt layer is 5 km thick and lies 10 km from the base of the lithosphere in the cold model, the melt layer is 15 km thick and lies 15 km from the base of the lithosphere in the cool model, and the melt layer is 35 km thick and lies 15 km from the base of the lithosphere in the warm model. As lithosphere thinning rates in the accreted domain begin to decline, melt production rates in the underlying asthenosphere also decline. Melt percentages begin to decline at a slightly later time as melting ceases and melt begins to freeze. Ultimately, melt quenches in this layer which spans the upper asthenosphere beneath most of the accreted domain. The specific time at which this layer quenches varies greatly depending on mantle temperature and is ~6 m.y., ~52 m.y., and ~85 m.y. for the cold, cool, and warm models, respectively.

3.6.2.2. Middle rifting – Melting focuses under broad rift in the accreted domain

Lithosphere thinning and thus melting of the underlying asthenosphere becomes progressively more concentrated in the western one-third of the accreted domain (Zone 1) during Substage 1B (Figures 3.8c, 3.9c, and 3.10c). Melting starts to concentrate in this region by ~13 m.y. and ~10 m.y. in the cool and warm models, respectively. In the cold model, the transition from minor melting over the breadth of the extending accreted domain to melting that is confined to Zone 1 is less gradational than in the cool and warm models. In the cold model, the initial melt layer underlying the breadth of the accreted domain quenches by ~6 m.y. as extension in the region wanes. Renewed melting under Zone 1 begins by ~20 m.y. With continued extension, melt becomes progressively more concentrated in this region in all models, reaching maximum percentages of ~3%, ~7%, and ~11% in the cold, cool, and warm models, respectively. These maximum melt percents are achieved by ~47 m.y. in all models. This roughly coincides with the transition between structural Stages 1 and 2. By 47 m.y., the melt zone is 150 km wide and 25 km thick in the cold model, 290 km wide and 45 km thick in the cool model, and 330 km wide and 60 km thick in the warm model. At this time, the top of the melt zone lies ~25 km, 20 km, and 15 km below the base of the lithosphere in the cold, cool, and warm models, respectively. After 47 m.y., and throughout Substage 2A, melt remains most concentrated beneath Zone 1 but the maximum melt percent progressively decreases. This freezing occurs as strain wanes in the interior of Zone 1 (Zone 1b) and becomes focused on its western and eastern margins (Zones 1a and 1c) during Substage 2A (as described in Section 3.5.2.2.1). In the cool and warm models, melt is present beneath Zone 1 throughout Substage 2A. In the cold model, all melting ceases and melt quenches (<0.1% maximum melt percent) by ~62 m.y. By the end of Substage 2A at 65 m.y., maximum melt percents have decreased to <0.1%, ~5%, and ~9% in the cold, cool, and warm models, respectively.

3.6.2.3. Late rifting – Melting focuses under lithosphere neck in the transitional region

As the lithosphere neck develops in the transitional region (Zone 1a) during Substage 2B, melting becomes progressively more concentrated in the underlying asthenosphere (Figures 3.8d, 3.9d, and 3.10d). In the cool and warm models, the focus of melting shifts from underlying all of Zone 1 to concentrating under the emerging neck in the transitional lithosphere (Zone 1a) near the accreted domain boundary by 75 m.y. and 70 m.y., respectively. In the cold model, renewed melting begins under the necking region (Zone 1a) by 88 m.y. The maximum melt percents in the mantle beneath the lithosphere neck progressively increase until the end of modeled extension at 100 m.y. in all models, and are ~6%, ~13%, and ~17%, in the cold, cool, and warm models, respectively. At this time, the size of the melt region is 130 km wide and 45 km thick in the cold model, 230 km wide and 75 km thick in the cool model, and 390 km wide and 80 km thick in the warm model. At the end of modeled extension, the depth to the top of the melt region lies ~25 km below the base of the lithosphere in the cold model and ~15 km below the base of the lithosphere in the cool and warm models.

3.7. Discussion

3.7.1. Comparisons of the WARS and best-fit geodynamic models

The cool model with a mantle potential temperature of 1300 °C best reproduces both modern observations of the WARS (after 100 m.y. of modeled extension) and the structural and magmatic evolution of the rift. Thus, the cool model is the focus of the discussion (Figure 3.9). This is generally consistent with previous geodynamic models that have suggested a relatively cool asthenosphere ($T_p \leq 1300$ °C) is required to best match the overall structural evolution of the WARS (Bialas et al., 2007; Harry et al., 2018; Huerta & Harry, 2007; van Wijk et al., 2008).

3.7.1.1. Modern WARS observations and the best-fit model after 100 m.y. of extension

3.7.1.1.1. Structural comparisons

The state of the best-fit model after 100 m.y. of extension compares well to modern observations from the WARS (Figure 3.11). At the end of modeled extension in the best-fit model, the broad extended lithosphere region (Zone 1) between ~400 and 1200 km distance (~800 km wide) corresponds well to the Ross Sea in the WARS which is ~800 – 1000 km wide. The region of highly focused extension near the western margin of the Ross Sea in the best-fit model (Zone 1a) located between ~400 and 600 km distance (~200 km wide), is consistent with observations of the width (~180 km) and relative location of Victoria Land Basin in the WARS. In the best-fit model, the crustal boundary between East and West Antarctica is located at ~725 km distance (~325 km east of Victoria Land) under the interpreted Ross Sea. This compares well to the WARS where the crustal boundary is proposed to lie beneath the Ross Sea ~400 km

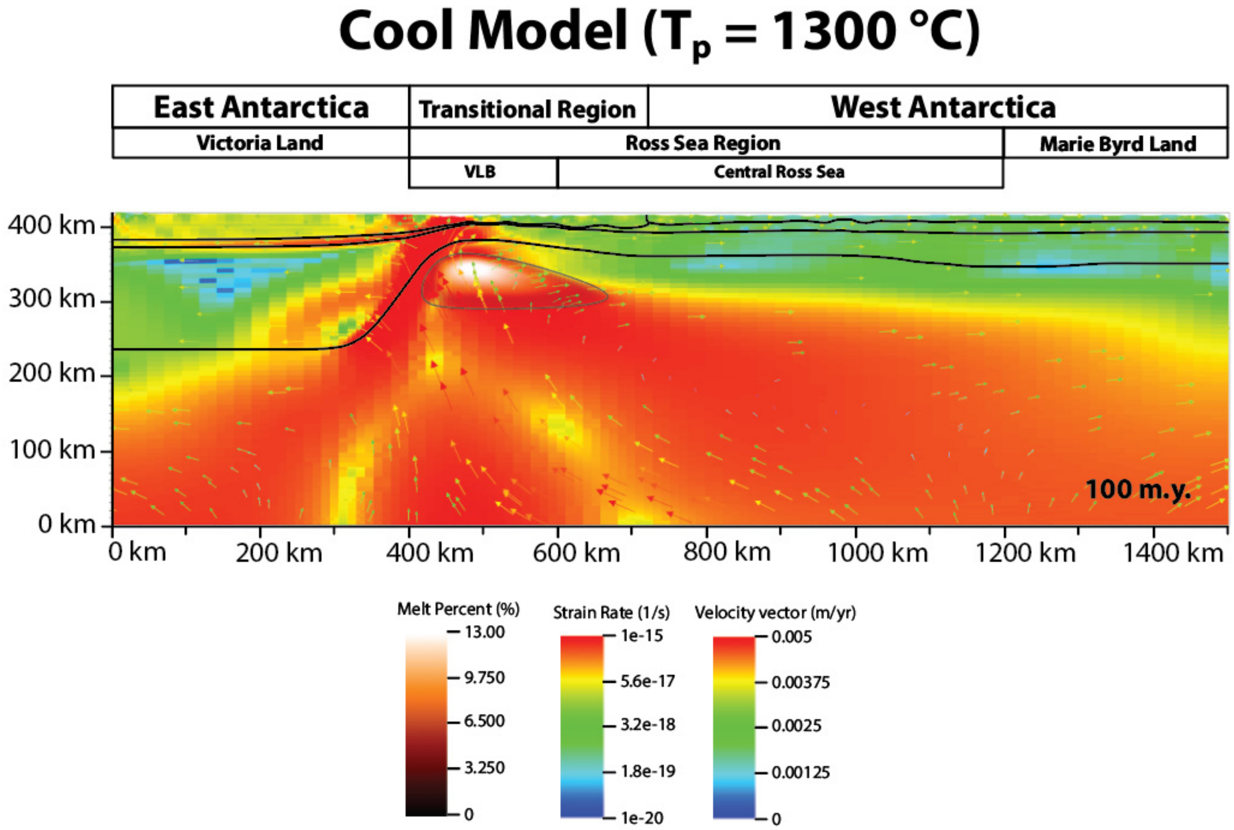

Figure 3.11. Interpreted regions of the West Antarctic Rift System in the best-fit model (T_p = 1300 °C) after 100 m.y. of modeled extension. Same as panel D in Figure 3.9. The background colors indicate strain rate and the colors and size of the vectors indicate velocity. Black line surrounding melt is the 1% melt contour. Victoria Land Basin (VLB).

east of Victoria Land (Jordan et al., 2020; Tinto et al., 2019). The central Ross Sea (excluding the highly extended Victoria Land Basin) in the best-fit model has a uniform crustal thickness of ~20 km which is relatively consistent with observations from the WARS where basins and intrabasin highs range between ~15 – 25 km and ~25 – 30 km, respectively (An et al., 2015a; Chaput et al., 2014; Trey et al., 1999; Wiens et al., 2023). The lithosphere of this region in the model is uniformly ~55 km thick which compares well to modern geophysical observations that range between 60 – 90 km thick with the lowest thicknesses generally occurring to the west (adjacent to Victoria Land Basin) and increasing to the east (An et al., 2015b; Brown & Fischer, 2025; Wiens et al., 2023). In the best-fit model, the crust and lithosphere of Victoria Land Basin are much thinner than the rest of the Ross Sea with thicknesses of ~10 – 20 km and 40 km, respectively. Similar crustal and lithosphere thicknesses are observed in Victoria Land Basin in the WARS which are 15 – 25 km and 50 – 60 km, respectively (An et al., 2015a, 2015b; Chaput et al., 2014; Trey et al., 1999; Wiens et al., 2023).

The western and eastern flanks of the Ross Sea in the best-fit model after 100 m.y. of extension, also compare well to observations from the WARS. In the best-fit model, the western flank spans the area from the western edge of the model at 0 km distance to the boundary between Victoria Land and Victoria Land Basin at ~400 km distance. The western flank remains largely unextended in the best-fit model with crustal and lithosphere thicknesses of ~40 km and 180 km, respectively. This compares well with observations from the WARS, where the crustal and lithosphere thicknesses from the western flank are ~30 – 45 km and ~100 – 180 km, respectively (An et al., 2015a, 2015b; Chaput et al., 2014; Wiens et al., 2023). In the best-fit model, the eastern flank of the Ross Sea corresponds to the area spanning from ~1200 km distance to the eastern edge of the model at 1500 km distance. In this model, the crust east of the Ross Sea has a uniform thickness of ~25 km after 100 m.y. of modeled extension. This is consistent with the WARS where crustal thicknesses from the eastern flank of the Ross Sea range between 25 to 35 km with the greatest thicknesses occurring in Marie Byrd Land (An et al., 2015a; Chaput et al., 2014; Wiens et al., 2023). The lithosphere of the eastern flank in the best-fit model is ~70 km thick which is in close agreement with observations from the WARS where lithosphere thickness is ~70 – 100 km (An et al., 2015b; Brown & Fischer, 2025).

3.7.1.1.2. Magmatic comparisons

After 100 m.y. of extension, the best-fit model suggests melt is present under the western margin of the Ross Sea (Zone 1a) which is consistent with active volcanism currently in Victoria Land and the Ross Island region (Smellie & Martin, 2021; Smellie & Rocchi, 2021). Notably, volcanism in the Ross Island region is attributed to an underlying mantle plume. As noted in Section 3.2.2.2.1., this is supported by slow seismic velocities in the upper mantle and enriched incompatible trace element and isotopic signatures of local basaltic rocks (Martin et al., 2021; Phillips et al., 2018; Sims et al., 2008; White-Gaynor et al., 2019; Wiens et al., 2023).

In the best-fit model, no melt is predicted to underlie the central Ross Sea (excepting the Victoria Land Basin) or the eastern margin at the end of modeled extension. While this result is consistent with the central Ross Sea in the WARS which is largely amagmatic and no modern magmatism is observed (Panter & Martin, 2023; Smellie et al., 2020), active volcanism is present in Marie Byrd Land along the eastern flank (Wilch et al., 2021). This suggests mantle temperatures are hotter under the eastern flank in Marie Byrd Land than those used in the models. This is consistent with an underlying plume which has been invoked as the source of modern volcanism in Marie Byrd Land as discussed above in Section 3.2.2.2.2. (Hart et al., 1997; LeMasurier & Landis, 1996; Panter et al., 2000, 2021).

3.7.1.2. Structural and magmatic evolution of the WARS and best-fit model

3.7.1.2.1. Broad rifting and magmatism

The best-fit model undergoes an initial ~50 m.y. period of broad extension, which agrees with the duration of the broad rift phase in the WARS that occurred between ~105-55 Ma (Cooper et al., 1991a, 1991b; Davey & Brancolini, 1995; Fitzgerald, 2002; Lawver & Gahagan, 1994; Siddoway, 2008; Storey & Granot, 2021). Melting during the broad rifting stage of the best-fit model is generally focused in the upper asthenosphere beneath the extending Ross Sea region. A melt zone forms in the underlying upper asthenosphere and increases in size and melt percent (maximum of 7% melt) as the lithosphere of the Ross Sea region thins. This is consistent with small amounts of melting predicted to have occurred during the Cretaceous phase of broad extension (Aviado et al., 2015; Panter et al., 2018; Rocchi et al., 2002; Rocchi & Smellie, 2021). These authors have suggested this melt quenched in and/or metasomatized the lithosphere. These fertile source rocks embedded in the lithosphere are proposed to be the melt sources of WARS Cenozoic magmatic rocks based on trace element and isotopic compositions (Aviado et al., 2015; Panter et al., 2018; Rocchi & Smellie, 2021). Our models do support melting of fusible dry sources in the upper asthenosphere during the Cretaceous, but this melt quenches in the uppermost asthenosphere before reaching the lithosphere. However, we did not test lower permeabilities which may allow the melt to rise into the lithospheric mantle at this time.

3.7.1.2.2. Narrow rifting and magmatism

In the best-fit model, extension wanes in the central Ross Sea after 50 m.y. of modeled extension and progressively concentrates along the western flank of the WARS from 50 – 100 m.y. This is consistent with observations from the WARS which suggest that extension of the central Ross Sea ceased by the Paleogene (Brancolini et al., 1995; Cooper et al., 1991b; Davey & Brancolini, 1995) and accelerated along the western flank from the Paleogene to the present (Cooper et al., 1991a; Davey et al., 2006; Davey & Brancolini, 1995; Fielding et al., 2006, 2008; Fitzgerald, 1992; Granot et al., 2013; Sauli et al., 2021; Storey & Granot, 2021). In the best-fit model, extension also focuses along the eastern flank for a short time (between 50 – 65 m.y.). In the WARS, evidence of Cenozoic extension near the eastern flank is limited to Pine Island Rift and Byrd Subglacial Basin (Jordan et al., 2010; Spiegel et al., 2016). Results from the best fit model suggest that i) the eastern flank underwent less overall extension than the western flank and ii) extension along the eastern flank ended by 35 Ma (~65 m.y. after the onset of extension). However, the amount of extension and the timing of extension along the eastern flank of the WARS are largely unknown.

In the best-fit model, the melt zone under the Ross Sea region reaches a maximum of 7% melt by 50 m.y. (equivalent to 50 Ma) when broad extension of the Ross Sea transitions to narrow extension focused on the margins. This compares well to the timing of onset of alkaline plutonism in North Victoria Land along the western flank of the Ross Sea at ~50 Ma (Rocchi et al., 2002; Rocchi & Smellie, 2021) and the proposed Cenozoic age of magmatic bodies inferred from Ross Sea and Ross Ice Shelf magnetic anomalies (Behrendt et al., 1991, 1994, 1996). From 50 – 75 m.y. of modeled extension in the best-fit model both melt percent and size of the melt zone underlying the Ross Sea decrease as extension slows in the central region and becomes concentrated along the margins. By 75 m.y. in the best fit model, the focus of melting shifts from under the central Ross Sea region to under the emerging lithosphere neck along the western margin. This is generally consistent with observations from the WARS that most of the known non-plume related magmatic rocks are located along the western edge of the Ross Sea (Aviado et al., 2015; Panter et al., 2018; Rocchi et al., 2002; Rocchi & Smellie, 2021). From 75 – 100 m.y. of modeled extension in the best fit model, melt percents and size of the melt zone under the western flank of the Ross Sea progressively increase reaching a maximum of 13% melt after 100 m.y. of modeled extension. This compares well to observations from the WARS that show volcanism along the western flank begins by ~20 Ma and increases in spatial distribution with time as most volcanism occurs <10 Ma (Smellie & Martin, 2021; Smellie & Rocchi, 2021). Notably, melt is absent from the eastern margin of the Ross Sea region in the best-fit model. This is generally consistent with observations as evidence of Cenozoic rift-related (non-plume) magmatism from the eastern flank of the WARS is limited. An exception is in Marie Byrd Land where Cenozoic magmatism occurred but is generally attributed to a plume rather than decompression melting related to rifting (LeMasurier & Landis, 1996; Panter et al., 2021; Panter & Martin, 2023).

3.7.2. Implications for the WARS

3.7.2.1. Sources of WARS magmatism

As described above in the best-fit model, magmatism simulated by melting of basaltic sources in the mantle reproduces the observed timing and spatial distribution of magmatic rocks emplaced in the Ross Sea region of the WARS with the exception of Cenozoic plume magmatism along the western and eastern margins. This suggests that WARS syn-rift magmatism (excepting plume-related magmatism of the Ross Island region and Marie Byrd Land) is generated by decompression melting of very fusible lithologies. We recognize that partial melting of basalt (as simulated in the models) would not produce rocks of basaltic composition (e.g., Defant & Drummond; Drummond & Defant, 1990) such as those erupted along the flanks of the WARS during the Cenozoic (e.g., Panter et al., 2021; Smellie & Martin, 2021; Smellie &

Rocchi, 2021; Wilch et al., 2021). Wet lithologies were not tested in these models because ASPECT does not currently support hydrous melting, but it can be inferred that these hydrous sources would melt early during the rift history similarl to basalt (e.g., Mayle & Harry, 2023). Unlike melts derived from basaltic protoliths, melts derived from hydrous ultramafic protoliths could produce basaltic melts (e.g., Hirose & Kawamoto, 1995). Decompression melting of hydrous lithologies has been proposed as sources of alkaline syn-rift non-plume magmatism along the western flank of the WARS (Aviado et al., 2015; Panter et al., 2018; Panter & Martin, 2023; Rocchi & Smellie, 2021). These fusible source rocks are suggested to be emplaced in the lithosphere and/or asthenosphere during previous extension or prior subduction episodes.

The WARS models did not attempt to reproduce melt due to the presence of mantle plumes. While mantle plume temperatures were not necessary to generate melt along the western flank in the models, it does not necessarily preclude a mantle plume under Ross Island. Along the eastern flank of the WARS, the models predict no melting which is in contrast with modern observations of widespread Cenozoic magmatism in Marie Byrd Land (e.g., Wilch et al., 2021). Thus, the models are consistent with previous arguments made on the basis of geochemical and seismic observations for elevated mantle temperatures associated with a mantle plume beneath Marie Byrd Land (Hansen et al., 2014; Hart et al., 1997; Lloyd et al., 2015, 2020; Panter et al., 2000, 2021; Panter & Martin, 2023; Wiens et al., 2023). Melting of hydrous phases in the lower lithosphere and upper asthenosphere have also been proposed to contribute to Marie Byrd Land magmatism (e.g., Hart et al., 1997; Panter et al., 2000). As noted in Section 3.1., the models in this paper do not consider the melting of hydrous phases but do not conflict with such arguments.

3.7.2.2. Relationship between WARS magmatism and rifting

In the models tested here, which do not evaluate mantle plumes or the melting of hydrous lithologies, the structural evolution of the WARS was found to be identical whether melting occurs or not.

This suggests that magmatism does not drive rifting in the WARS. However, the magmatic evolution is closely influenced by the structural evolution. Thus, it can be concluded that at least from the models examined here, WARS magmatism responds to rifting and does not drive it.

3.7.3. Broader implications

3.7.3.1. Delamination

Results show that a drip of the lowermost lithosphere mantle under the transitional region forms in the warm model (T_p = 1330 °C) (Figure 3.7). Delamination has been suggested along the Southern TAMS and potentially the Central TAMS based on the geometries of high seismic velocity anomalies which are attributed to cold lithosphere dipping into the hot asthenosphere (Shen et al., 2017, 2018). However, along the northern TAMS (adjacent to the Ross Sea) no such delamination is observed. Delamination has been proposed in both broad and narrow rifts such as under the Sierra Nevada region along the western margin of the Basin and Range province in the western U.S. (Saleeby et al., 2012, 2013) and in the East African Rift System (Furman et al., 2016; Wallner & Schmeling, 2011). Both are rifts that lie above mantle with potential temperatures generally greater than the global average of ~1350 °C (Plank & Forsyth, 2016; Rooney et al., 2012). Thus, it can be inferred that delamination i) is unlikely to occur in rifts if mantle potential temperatures lie significantly below the global average of ~1350 °C and ii) is a consequence mainly of mantle temperature, and not structural style of the rift.

3.7.3.2. Modeled syn-rift magmatism

Unlike reality in which Cenozoic volcanism is observed in the WARS (Smellie & Martin, 2021; Smellie & Rocchi, 2021; Wilch et al., 2021), no melt reached the surface in any model. We infer that the lack of surface volcanism in our models is likely a result of low mantle permeability used in the models. ASPECT utilizes a simple permeability model where permeability is dependent on melt fraction and a reference permeability (equation 7). At low melt fractions, permeability is also low and thus melt ascent rate is slow. This promotes cooling of the melt and therefore quenching. We did not explore higher permeabilities in the WARS models which would allow melt to ascend to the surface, possibly promoting magma assisted rifting (e.g., Buck et al., 2006; Schmeling & Wallner, 2012; Toro et al., 2006).

3.8. Conclusions

This paper presents a series of finite element models with and without magmatism that simulate the geodynamic evolution of the WARS. The purpose of these models was to investigate the potential for various mantle compositions to produce early syn-rift melt and the impacts of this melt on the magmatic and structural evolution of the WARS. A series of models were evaluated with mantle potential temperatures ranging between 1270 °C and 1330 °C, consistent with results from previous geodynamic models (Bialas et al., 2007; Harry et al., 2018; Huerta & Harry, 2007; van Wijk et al., 2008) and thermobarometric estimates from WARS Cenozoic magmatic rocks (Armienti & Perinelli, 2010; Perinelli et al., 2006, 2011). The models tested the melting of different mantle lithologies (e.g., depleted and fertile lherzolite, basalt, and pyroxenite) proposed to be emplaced in the lower lithosphere and upper asthenosphere during previous tectonomagmatic episodes (Aviado et al., 2015; Panter et al., 2018; Rocchi & Smellie, 2021). Results show that:

1. Models with cool mantle temperatures (as indicated by the models with T_p = 1300 °C) best reproduce modern day observations of the WARS and the structural and magmatic evolution of the rift. Generally, this evolution is characterized by a largely amagmatic broad rifting stage (~100 – 50 Ma) resulting in extension of the Ross Sea followed by a magmatic narrow rifting stage (~50 Ma – present?) where extension slows in the central Ross Sea and accelerates along the margins. Models with mantle temperatures near the global average (T_p = 1330 °C) lead to delamination of the lowermost lithosphere under East Antarctica which is not observed along the Ross Sea (Shen et al., 2018). Models with cold mantle temperatures (T_p = 1270 °C) reproduce the structural

evolution of the WARS but suggest a gap in Cenozoic magmatism (from 38 Ma to 12 Ma) which is inconsistent with observations.

2. Of all lithologies evaluated in the WARS models, only basalt melted. During broad rifting (Late Cretaceous – Cenozoic) the models suggest that small degree melts (maximum of ~7% in the best fit model) would be generated by basaltic source rocks in the upper asthenosphere underlying the Ross Sea. This is consistent with magnetic anomalies interpreted to be magmatic rocks underlying the Ross Sea and Ross Ice Shelf (Behrendt et al., 1991, 1994, 1996; Jordan et al., 2020; Tinto et al., 2019). Small degree melting under the Ross Sea is also consistent with proposed petrogenic models which call for the limited melting of subducted slab material during Late Cretaceous broad rifting to metasomatize the mantle and/or to emplace fusible lithologies (Aviado et al., 2015; Panter et al., 2018; Rocchi et al., 2002; Rocchi & Smellie, 2021). During narrow rifting (Cenozoic - present), the focus of melting shifts to the emerging lithosphere neck along the western margin of the Ross Sea and achieves a maximum of 13% melt in the best-fit model after 100 m.y. of extension. This melting suggests that fusible sources could produce Cenozoic magmatism along the western flank of the WARS (e.g., Victoria Land) without invoking a plume or elevated modern mantle temperatures. No melting of any tested lithology occurred under the eastern flank in the models. This suggests that elevated temperatures (i.e., those from a mantle plume) are necessary to reproduce observed Cenozoic magmatism along the eastern flank of the WARS.
3. Basalt was the most fusible source tested. Other lithologies with high fusibilities (which were not tested here) include hydrous lithologies. Thus, our models suggest that very fusible sources such as mafic or hydrous lithologies were likely responsible for WARS syn-rift (non-plume) magmatism along the western flank of the WARS.

4. The structural evolution of the WARS is essentially identical in all models, regardless of whether melting was included or not. However, magmatism is highly responsive to the structural evolution of the WARS. This suggests that the WARS is a passive rift.

References in chapter 3

Adams, C. J. (1987). Geochronology of granite terranes in the ford ranges, marie byrd land, West Antarctica. New Zealand Journal of Geology and Geophysics, 30(1), 51–72. https://doi.org/10.1080/00288306.1987.10422193

Allibone, A., & Wysoczanski, R. (2002). Initiation of magmatism during the Cambrian--Ordovician Ross orogeny in southern Victoria Land, Antarctica. Geological Society of America Bulletin, 114(8), 1007–1018.

An, M., Wiens, D. A., Zhao, Y., Feng, M., Nyblade, A. A., Kanao, M., Li, Y., Maggi, A., & Lévêque, J.-J. (2015a). S-velocity model and inferred Moho topography beneath the Antarctic Plate from Rayleigh waves. Journal of Geophysical Research: Solid Earth, 120(1), 359–383.

An, M., Wiens, D. A., Zhao, Y., Feng, M., Nyblade, A., Kanao, M., Li, Y., Maggi, A., & Lévêque, J.-J. (2015b). Temperature, lithosphere-asthenosphere boundary, and heat flux beneath the Antarctic Plate inferred from seismic velocities. Journal of Geophysical Research: Solid Earth, 120(12), 8720–8742. https://doi.org/https://doi.org/10.1002/2015JB011917

Armienti, P., & Perinelli, C. (2010). Cenozoic thermal evolution of lithospheric mantle in northern Victoria Land (Antarctica): Evidences from mantle xenoliths. Tectonophysics, 486(1), 28–35. https://doi.org/https://doi.org/10.1016/j.tecto.2010.02.006

Aviado, K. B., Rilling-Hall, S., Bryce, J. G., & Mukasa, S. B. (2015). Submarine and subaerial lavas in the West Antarctic Rift System: Temporal record of shifting magma source components from the lithosphere and asthenosphere. Geochemistry, Geophysics, Geosystems, 16(12), 4344–4361. https://doi.org/10.1002/2015GC006076

Bangerth, W., Dannberg, J., Fraters, M., Gassmoeller, R., Glerum, A., Heister, T., Myhill, R., & Naliboff, J. (2024a). ASPECT: Advanced Solver for Planetary Evolution, Convection, and Tectonics, User Manual. https://doi.org/10.6084/m9.figshare.4865333

Bangerth, W., Dannberg, J., Fraters, M., Gassmoeller, R., Glerum, A., Heister, T., Myhill, R., & Naliboff, J. (2024b). ASPECT v3.0.0. Zenodo. https://doi.org/10.5281/zenodo.14371679

Behrendt, J. C., Blankenship, D. D., Finn, C. A., Bell, R. E., Sweeney, R. E., Hodge, S. M., & Brozena, J. M. (1994). CASERTZ aeromagnetic data reveal late Cenozoic flood basalts (?) in the West Antarctic rift system. Geology, 22(6), 527–530. https://doi.org/10.1130/0091-7613(1994)022<0527:CADRLC>2.3.CO;2

Behrendt, J. C., LeMasurier, W. E., Cooper, A. K., Tessensohn, F., Trehu, A., & Damaske, D. (1991). Geophysical studies of the West Antarctic rift system. Tectonics, 10(6), 1257–1273.

Behrendt, J. C., Saltus, R., Damaske, D., McCafferty, A., Finn, C. A., Blankenship, D., & Bell, R. E. (1996). Patterns of late Cenozoic volcanic and tectonic activity in the West Antarctic rift system revealed by aeromagnetic surveys. Tectonics, 15(3), 660–676.

Bialas, R. W., Buck, W. R., Studinger, M., & Fitzgerald, P. G. (2007). Plateau collapse model for the transantarctic mountains-West Antarctic rift system: Insights from numerical experiments. Geology, 35(8), 687–690. https://doi.org/10.1130/G23825A.1

Boger, S. D., & Miller, J. M. L. (2004). Terminal suturing of Gondwana and the onset of the Ross-Delamerian Orogeny: The cause and effect of an Early Cambrian reconfiguration of plate motions. Earth and Planetary Science Letters, 219(1–2), 35–48. https://doi.org/10.1016/S0012-821X(03)00692-7

Borg, S. G., Stump, E., Chappell, B. W., McCulloch, M. T., Wyborn, D., Armstrong, R. L., & Holloway, J. R. (1987). Granitoids of northern Victoria Land, Antarctica: implications of chemical and isotopic variations to regional crustal structure and tectonics. In American Journal of Science (Vol. 287, Issue 2, pp. 127–169). https://doi.org/10.2475/ajs.287.2.127

Bradshaw, J. D. (1989). Cretaceous geotectonic patterns in the New Zealand Region. Tectonics, 8(4), 803–820. https://doi.org/https://doi.org/10.1029/TC008i004p00803

Brancolini, G., Busetti, M., Marchetti, A., De Santis, L., Zanolla, C., Cooper, A. K., Cochrane, G. R., Zayatz, I., Belyaev, V., Knyazev, M., Vinnikovskaya, O., Davey, F. J., & Hinz, K. (1995). Descriptive Text for the Seismic Stratigraphic Atlas of the Ross Sea, Antarctica. In A. K. Cooper, P. F. Barker, & G. Brancolini (Eds.), Geology and Seismic Stratigraphy of the Antarctic Margin (pp. A271–A303). American Geophysical Union (AGU). https://doi.org/https://doi.org/10.1002/9781118669013.app1

Brown, E. L., & Lesher, C. E. (2016). REEBOX PRO: A forward model simulating melting of thermally and lithologically variable upwelling mantle. Geochemistry, Geophysics, Geosystems, 17(10), 3929–3968. https://doi.org/10.1002/2016GC006579

Brown, S. E., & Fischer, K. M. (2025). Investigating the Antarctic Lithosphere Through Sp Receiver Function Analysis. Geochemistry, Geophysics, Geosystems, 26(10), e2025GC012268. https://doi.org/10.1029/2025GC012268

Buck, W. R., Einarsson, P., & Brandsdóttir, B. (2006). Tectonic stress and magma chamber size as controls on dike propagation: Constraints from the 1975–1984 Krafla rifting episode. Journal of Geophysical Research: Solid Earth, 111(B12). https://doi.org/https://doi.org/10.1029/2005JB003879

Cande, S. C., & Stock, J. M. (2006). Constraints on the Timing of Extension in the Northern Basin, Ross Sea. In D. K. Fütterer, D. Damaske, G. Kleinschmidt, H. Miller, & F. Tessensohn (Eds.), Antarctica: Contributions to Global Earth Sciences (pp. 319–326). Springer Berlin Heidelberg. https://doi.org/10.1007/3-540-32934-X_40

Cande, S. C., Stock, J. M., Müller, R. D., & Ishihara, T. (2000). Cenozoic motion between East and West

Antarctica. Nature, 404(6774), 145–150. https://doi.org/10.1038/35004501

Carter, N. L., & Tsenn, M. C. (1987). Flow properties of continental lithosphere. Tectonophysics, 136(1), 27–63. https://doi.org/https://doi.org/10.1016/0040-1951(87)90333-7

Chaput, J., Aster, R. C., Huerta, A., Sun, X., Lloyd, A. J., Wiens, D., Nyblade, A., Anandakrishnan, S., Winberry, J. P., & Wilson, T. (2014). The crustal thickness of West Antarctica. Journal of Geophysical Research: Solid Earth, 119(1), 378–395. https://doi.org/10.1002/2013JB010642

Cooper, A. K., Davey, F. J., & Behrendt, J. C. (1991a). Structural and depositional controls on Cenozoic and (?) Mesozoic strata beneath the western Ross Sea. In M. R. A. Thompson, J. A. Crame, & J. W. Thomson (Eds.), Geological Evolution of Antarctica (pp. 279–284). Cambridge University Press.

Cooper, A. K., Davey, F. J., & Hinz, K. (1991b). Crustal extension and origin of sedimentary basins beneath the Ross Sea and Ross Ice Shelf, Antarctica. In M. R. A. Thompson, J. A. Crame, & J. W. Thomson (Eds.), Geological Evolution of Antarctica (pp. 285–291). Cambridge University Press.

Dalziel, I. W. D., & Elliot, D. H. (1982). West Antarctica: problem child of Gondwanaland. Tectonics, 1(1), 3–19.

Dalziel, I. W. D., & Lawver, L. A. (2001). The lithospheric setting of the West Antarctic ice sheet. The West Antarctic Ice Sheet: Behavior and Environment, Antarct. Res. Ser, 77, 29–44.

Dannberg, J., & Heister, T. (2016). Compressible magma/mantle dynamics: 3D, adaptive simulations in ASPECT. Geophysical Journal International, 207(3), 1343–1366. https://doi.org/10.1093/gji/ggw329

Davey, F. J., & Brancolini, G. (1995). The Late Mesozoic and Cenozoic Structural Setting of the Ross Sea Region. In Geology and Seismic Stratigraphy of the Antarctic Margin (pp. 167–182). American Geophysical Union (AGU). https://doi.org/https://doi.org/10.1029/AR068p0167

Davey, F. J., Cande, S. C., & Stock, J. M. (2006). Extension in the western Ross Sea region-links between Adare Basin and Victoria Land Basin. Geophysical Research Letters, 33(20). https://doi.org/https://doi.org/10.1029/2006GL027383

Davey, F. J., Granot, R., Cande, S. C., Stock, J. M., Selvans, M., & Ferraccioli, F. (2016). Synchronous oceanic spreading and continental rifting in West Antarctica. Geophysical Research Letters, 43(12), 6162–6169. https://doi.org/https://doi.org/10.1002/2016GL069087

Defant, M. J., & Drummond, M. S. (1990). Derivation of some modern arc magmas by melting of young subducted lithosphere. Nature, 347(6294), 662–665. https://doi.org/10.1038/347662a0

Drummond, M. S., & Defant, M. J. (1990). A model for Trondhjemite-Tonalite-Dacite Genesis and crustal growth via slab melting: Archean to modern comparisons. Journal of Geophysical Research: Solid Earth, 95(B13), 21503–21521. https://doi.org/https://doi.org/10.1029/JB095iB13p21503

Emry, E. L., Nyblade, A. A., Horton, A., Hansen, S. E., Julià, J., Aster, R. C., Huerta, A. D., Winberry, J. P., Wiens, D. A., & Wilson, T. J. (2020). Prominent thermal anomalies in the mantle transition zone beneath the Transantarctic Mountains. Geology, 48(7), 748–752. https://doi.org/10.1130/G47346.1

Emry, E. L., Nyblade, A. A., Julià, J., Anandakrishnan, S., Aster, R. C., Wiens, D. A., Huerta, A. D., & Wilson, T. J. (2015). The mantle transition zone beneath West Antarctica: Seismic evidence for hydration and thermal upwellings. Geochemistry, Geophysics, Geosystems, 16(1), 40–58.

Encarnación, J., & Grunow, A. (1996). Changing magmatic and tectonic styles along the paleo-Pacific margin of Gondwana and the onset of early Paleozoic magmatism in Antarctica. Tectonics, 15(6), 1325–1341.

Esser, R. P., Kyle, P. R., & McIntosh, W. C. (2004). 40Ar/39Ar dating of the eruptive history of Mount Erebus, Antarctica: Volcano evolution. Bulletin of Volcanology, 66(8), 671–686. https://doi.org/10.1007/s00445-004-0354-x

Farmer, G. L., Fritz, D. E., & Glazner, A. F. (2020). Identifying Metasomatized Continental Lithospheric Mantle Involvement in Cenozoic Magmatism From Ta/Th Values, Southwestern North America. Geochemistry, Geophysics, Geosystems, 21(5), e2019GC008499. https://doi.org/https://doi.org/10.1029/2019GC008499

Fielding, C. R., Henrys, S. A., & Wilson, T. J. (2006). Rift History of the Western Victoria Land Basin: A new Perspective Based on Integration of Cores with Seismic Reflection Data. Antarctica, 309–318. https://doi.org/10.1007/3-540-32934-x_39

Fielding, C. R., Whittaker, J., Henrys, S. A., Wilson, T. J., & Naish, T. R. (2008). Seismic facies and stratigraphy of the Cenozoic succession in McMurdo Sound, Antarctica: Implications for tectonic, climatic and glacial history. Palaeogeography, Palaeoclimatology, Palaeoecology, 260(1–2), 8–29. https://doi.org/10.1016/j.palaeo.2007.08.016

Fitton, J. G., James, D., & Leeman, W. P. (1991). Basic magmatism associated with late Cenozoic extension in the western United States: Compositional variations in space and time. Journal of Geophysical Research: Solid Earth, 96(B8), 13693–13711. https://doi.org/10.1029/91JB00372

Fitzgerald, P. G. (1992). The Transantarctic Mountains of southern Victoria Land: The application of apatite fission track analysis to a rift shoulder uplift. Tectonics, 11(3), 634–662. https://doi.org/10.1029/91TC02495

Fitzgerald, P. G. (2002). Tectonics and landscape evolution of the Antarctic plate since the breakup of Gondwana, with an emphasis on the West Antarctic Rift System and the Transantarctic Mountains. Royal Society of New Zealand Bulletin, 35, 453–469.

Fitzgerald, P. G., Sandiford, M., Barrett, P. J., & Gleadow, A. J. W. (1986). Asymmetric extension associated with uplift and subsidence in the Transantarctic Mountains and Ross Embayment. Earth and Planetary Science Letters, 81(1), 67–78. https://doi.org/https://doi.org/10.1016/0012-821X(86)90101-9

Furman, T., Nelson, W. R., & Elkins-Tanton, L. T. (2016). Evolution of the East African rift: Drip magmatism, lithospheric thinning and mafic volcanism. Geochimica et Cosmochimica Acta, 185, 418–434. https://doi.org/https://doi.org/10.1016/j.gca.2016.03.024

Gerya, T. (2019). Introduction to Numerical Geodynamic Modelling (2nd ed.). Cambridge University Press.

Goodge, J. W. (1997). Latest Neoproterozoic basin inversion of the Beardmore Group, central Transantarctic Mountains, Antarctica. Tectonics, 16(4), 682–701.

Goodge, J. W. (2020). Geological and tectonic evolution of the Transantarctic Mountains, from ancient craton to recent enigma. Gondwana Research, 80, 50–122. https://doi.org/10.1016/j.gr.2019.11.001

Granot, R., Cande, S. C., Stock, J. M., & Damaske, D. (2013). Revised Eocene-Oligocene kinematics for the West Antarctic rift system. Geophysical Research Letters, 40(2), 279–284. https://doi.org/https://doi.org/10.1029/2012GL054181

Granot, R., Cande, S. C., Stock, J. M., Davey, F. J., & Clayton, R. W. (2010). Postspreading rifting in the Adare Basin, Antarctica: Regional tectonic consequences. Geochemistry, Geophysics, Geosystems, 11(8). https://doi.org/https://doi.org/10.1029/2010GC003105

Granot, R., & Dyment, J. (2018). Late Cenozoic unification of East and West Antarctica. Nature Communications, 9(1). https://doi.org/10.1038/s41467-018-05270-w

Hansen, S. E., Graw, J. H., Kenyon, L. M., Nyblade, A. A., Wiens, D. A., Aster, R. C., Huerta, A. D., Anandakrishnan, S., & Wilson, T. (2014). Imaging the Antarctic mantle using adaptively parameterized P-wave tomography: Evidence for heterogeneous structure beneath West Antarctica. Earth and Planetary Science Letters, 408, 66–78. https://doi.org/10.1016/j.epsl.2014.09.043

Hanyu, T., Tatsumi, Y., Senda, R., Miyazaki, T., Chang, Q., Hirahara, Y., Takahashi, T., Kawabata, H., Suzuki, K., Kimura, J.-I., & Nakai, S. (2011). Geochemical characteristics and origin of the HIMU reservoir: A possible mantle plume source in the lower mantle. Geochemistry, Geophysics, Geosystems, 12(2). https://doi.org/https://doi.org/10.1029/2010GC003252

Harry, D. L., Anoka, J. L., & Jha, S. (2018). Geodynamic models of the West Antarctic Rift System: Implications for the mantle thermal state. Geosphere, 14(6), 2407–2429. https://doi.org/10.1130/GES01594.1

Harry, D. L., & Leeman, W. P. (1995). Partial melting of melt metasomatized subcontinental mantle and the magma source potential of the lower lithosphere. Journal of Geophysical Research: Solid Earth, 100(B6), 10255–10269. https://doi.org/10.1029/94JB03065

Hart, S. R., Blusztajn, J., LeMasurier, W. E., & Rex, D. C. (1997). Hobbs Coast Cenozoic volcanism: Implications for the West Antarctic rift system. Chemical Geology, 139(1–4), 223–248. https://doi.org/10.1016/S0009-2541(97)00037-5

Hasterok, D., & Chapman, D. S. (2011). Heat production and geotherms for the continental lithosphere. Earth and Planetary Science Letters, 307(1), 59–70. https://doi.org/https://doi.org/10.1016/j.epsl.2011.04.034

Heister, T., Dannberg, J., Gassmöller, R., & Bangerth, W. (2017). High Accuracy Mantle Convection Simulation through Modern Numerical Methods. II: Realistic Models and Problems. Geophysical Journal International, 210(2), 833–851. https://doi.org/10.1093/gji/ggx195

Herzberg, C., Asimow, P. D., Arndt, N., Niu, Y., Lesher, C. M., Fitton, J. G., Cheadle, M. J., & Saunders, A. D. (2007). Temperatures in ambient mantle and plumes: Constraints from basalts, picrites, and komatiites. Geochemistry, Geophysics, Geosystems, 8(2). https://doi.org/https://doi.org/10.1029/2006GC001390

Hirose, K., & Kawamoto, T. (1995). Hydrous partial melting of lherzolite at 1 GPa: the effect of H_2O on the genesis of basaltic magmas. Earth and Planetary Science Letters, 133(3–4), 463–473. https://doi.org/10.1016/0012-821X(95)00096-U

Hirschmann, M. M., Kogiso, T., Baker, M. B., & Stolper, E. M. (2003). Alkalic magmas generated by partial melting of garnet pyroxenite. Geology, 31(6), 481–484. https://doi.org/10.1130/0091-7613(2003)031<0481:AMGBPM>2.0.CO;2

Homrighausen, S., Hoernle, K., Hauff, F., Geldmacher, J., Wartho, J.-A., van den Bogaard, P., & Garbe-Schönberg, D. (2018). Global distribution of the HIMU end member: Formation through Archean plume-lid tectonics. Earth-Science Reviews, 182, 85–101. https://doi.org/https://doi.org/10.1016/j.earscirev.2018.04.009

Huerta, A. D., & Harry, D. L. (2007). The transition from diffuse to focused extension: Modeled evolution of the West Antarctic Rift system. Earth and Planetary Science Letters, 255(1–2), 133–147. https://doi.org/10.1016/j.epsl.2006.12.011

Jordan, T. A., Ferraccioli, F., Vaughan, D. G., Holt, J. W., Corr, H., Blankenship, D. D., & Diehl, T. M. (2010). Aerogravity evidence for major crustal thinning under the Pine Island Glacier region (West Antarctica). GSA Bulletin, 122(5–6), 714–726. https://doi.org/10.1130/B26417.1

Jordan, T. A., Riley, T. R., & Siddoway, C. S. (2020). The geological history and evolution of West Antarctica. Nature Reviews Earth & Environment, 1(2), 117–133. https://doi.org/10.1038/s43017-019-0013-6

Karato, S. I. (2013). Rheological Properties of Minerals and Rocks. In Physics and Chemistry of the Deep Earth (pp. 94–144). John Wiley & Sons, Ltd. https://doi.org/https://doi.org/10.1002/9781118529492.ch4

Katsura, T. (2022). A Revised Adiabatic Temperature Profile for the Mantle. Journal of Geophysical Research: Solid Earth, 127(2), e2021JB023562. https://doi.org/https://doi.org/10.1029/2021JB023562

Katz, R. F., Spiegelman, M., & Langmuir, C. H. (2003). A new parameterization of hydrous mantle melting. Geochemistry, Geophysics, Geosystems, 4(9), 1–19. https://doi.org/10.1029/2002GC000433

Keller, T., May, D. A., & Kaus, B. J. P. (2013). Numerical modelling of magma dynamics coupled to tectonic deformation of lithosphere and crust. Geophysical Journal International, 195(3), 1406–1442. https://doi.org/10.1093/gji/ggt306

Kronbichler, M., Heister, T., & Bangerth, W. (2012). High Accuracy Mantle Convection Simulation through Modern Numerical Methods. Geophysical Journal International, 191, 12–29. https://doi.org/10.1111/j.1365-246X.2012.05609.x

Kyle, P. R., Moore, J. A., & Thirlwall, M. F. (1992). Petrologic evolution of anorthoclase phonolite lavas at Mount Erebus, Ross island, Antarctica. Journal of Petrology, 33(4), 849–875. https://doi.org/10.1093/petrology/33.4.849

Lawver, L. A., & Gahagan, L. M. (1994). Constraints on timing of extension in the Ross Sea region. Terra Antartica, 1(3), 545–552.

Lee, C. T. A., Luffi, P., Plank, T., Dalton, H., & Leeman, W. P. (2009). Constraints on the depths and temperatures of basaltic magma generation on Earth and other terrestrial planets using new thermobarometers for mafic magmas. Earth and Planetary Science Letters, 279(1–2), 20–33. https://doi.org/10.1016/J.EPSL.2008.12.020

Leeman, W. P., & Fitton, J. G. (1989). Magmatism associated with lithospheric extension: Introduction. Journal of Geophysical Research: Solid Earth, 94(B6), 7682–7684. https://doi.org/10.1029/JB094iB06p07682

Leeman, W. P., & Harry, D. L. (1993). A binary source model for extension-related magmatism in the Great Basin, western North America. Science, 262(5139), 1550–1554. https://doi.org/10.1126/science.262.5139.1550

LeMasurier, W. E., & Landis, C. A. (1996). Mantle-plume activity recorded by low-relief erosion surfaces in West Antarctica and New Zealand. Bulletin of the Geological Society of America, 108(11), 1450–1466. https://doi.org/10.1130/0016-7606(1996)108<1450:MPARBL>2.3.CO;2

Lloyd, A. J., Wiens, D. A., Nyblade, A. A., Anandakrishnan, S., Aster, R. C., Huerta, A. D., Wilson, T. J., Dalziel, I. W. D., Shore, P. J., & Zhao, D. (2015). A seismic transect across West Antarctica: Evidence for mantle thermal anomalies beneath the Bentley Subglacial Trench and the Marie Byrd Land Dome. Journal of Geophysical Research: Solid Earth, 120(12), 8439–8460.

Lloyd, A. J., Wiens, D. A., Zhu, H., Tromp, J., Nyblade, A. A., Aster, R. C., Hansen, S. E., Dalziel, I. W. D., Wilson, T. J., Ivins, E. R., & O’Donnell, J. P. (2020). Seismic Structure of the Antarctic Upper Mantle Imaged with Adjoint Tomography. Journal of Geophysical Research: Solid Earth, 125(3). https://doi.org/https://doi.org/10.1029/2019JB017823

Martin, A. P., Cooper, A. F., Price, R. C., Kyle, P. R., & Gamble, J. A. (2021). Chapter 5.2b Erebus Volcanic Province: petrology. In J. L. Smellie, K. S. Panter, & A. Geyer (Eds.), Volcanism in Antarctica: 200 Million Years of Subduction, Rifting and Continental Break-up (pp. 447–489). Geological Society of London, Memoirs. https://doi.org/10.1144/M55-2018-80

Mayle, M., & Harry, D. L. (2023). Syn-Rift Magmatism and Sequential Melting of Fertile Lithologies in the Lithosphere and Asthenosphere. Journal of Geophysical Research: Solid Earth, 128(9), e2023JB027072. https://doi.org/https://doi.org/10.1029/2023JB027072

McMillan, N. J., Dickin, A. P., & Haag, D. (2000). Evolution of magma source regions in the Rio Grande rift, southern New Mexico. GSA Bulletin, 112(10), 1582–1593. https://doi.org/10.1130/0016-7606(2000)112<1582:EOMSRI>2.0.CO;2

Mukasa, S. B., & Dalziel, I. W. D. (2000). Marie Byrd Land, West Antarctica: Evolution of Gondwana's Pacific margin constrained by zircon U-Pb geochronology and feldspar common-Pb isotopic compositions. Bulletin of the Geological Society of America, 112(4), 611–627. https://doi.org/10.1130/0016-7606(2000)112<611:MBLWAE>2.0.CO;2

Pankhurst, R. J., Weaver, S. D., Bradshaw, J. D., Storey, B. C., & Ireland, T. R. (1998). Geochronology and geochemistry of pre-Jurassic superterranes in Marie Byrd Land, Antarctica. Journal of Geophysical Research: Solid Earth, 103(B2), 2529–2547.

Panter, K. S., Castillo, P., Krans, S., Deering, C., McIntosh, W., Valley, J. W., Kitajima, K., Kyle, P., Hart, S., & Blusztajn, J. (2018). Melt origin across a rifted continental margin: A case for subduction-related metasomatic agents in the lithospheric source of alkaline basalt, NW Ross Sea, Antarctica. Journal of Petrology, 59(3), 517–558. https://doi.org/10.1093/petrology/egy036

Panter, K. S., Hart, S. R., Kyle, P., Blusztanjn, J., & Wilch, T. (2000). Geochemistry of Late Cenozoic basalts from the Crary Mountains: Characterization of mantle sources in Marie Byrd Land, Antarctica. Chemical Geology, 165(3–4), 215–241. https://doi.org/10.1016/S0009-2541(99)00171-0

Panter, K. S., & Martin, A. P. (2023). West Antarctic mantle deduced from mafic magmatism. In A. P. Martin & W. van der Wal (Eds.), The Geochemistry and Geophysics of the Antarctic Mantle (pp. 133–149). Geological Society of London, Memoirs. https://doi.org/10.1144/M56-2021-10

Panter, K. S., Wilch, T. I., Smellie, J. L., Kyle, P. R., & McIntosh, W. C. (2021). Chapter 5.4b Marie Byrd Land and Ellsworth Land: petrology. In J. L. Smellie, K. S. Panter, & A. Geyer (Eds.), Volcanism in Antarctica: 200 Million Years of Subduction, Rifting and Continental Break-up (pp. 577–614). Geological Society of London, Memoirs. https://doi.org/10.1144/M55-2019-50

Perinelli, C., Armienti, P., & Dallai, L. (2006). Geochemical and O-isotope constraints on the evolution of lithospheric mantle in the Ross Sea rift area (Antarctica). Contributions to Mineralogy and Petrology, 151(3), 245–266. https://doi.org/10.1007/s00410-006-0065-8

Perinelli, C., Armienti, P., & Dallai, L. (2011). Thermal Evolution of the Lithosphere in a Rift Environment as Inferred from the Geochemistry of Mantle Cumulates, Northern Victoria Land, Antarctica. Journal of Petrology, 52(4), 665–690. https://doi.org/10.1093/petrology/egq099

Phillips, E. H., Sims, K. W. W., Blichert-Toft, J., Aster, R. C., Gaetani, G. A., Kyle, P. R., Wallace, P. J., & Rasmussen, D. J. (2018). The nature and evolution of mantle upwelling at Ross Island, Antarctica, with implications for the source of HIMU lavas. Earth and Planetary Science Letters, 498, 38–53. https://doi.org/10.1016/j.epsl.2018.05.049

Pilet, S. (2015). Generation of low-silica alkaline lavas: Petrological constraints, models, and thermal implications. In G. R. Foulger, M. Lustrino, & S. D. King (Eds.), The Interdisciplinary Earth: A Volume in Honor of Don L. Anderson (pp. 281–304). Geological Society of America. https://doi.org/10.1130/2015.2514(17)

Pilet, S., Baker, M. B., Müntener, O., & Stolper, E. M. (2011). Monte Carlo simulations of metasomatic enrichment in the lithosphere and implications for the source of alkaline basalts. Journal of Petrology, 52(7–8), 1415–1442. https://doi.org/10.1093/petrology/egr007

Pilet, S., Baker, M. B., & Stolper, E. M. (2008). Metasomatized lithosphere and the origin of alkaline lavas. Science, 320(5878), 916–919. https://doi.org/10.1126/science.1156563

Pitcavage, E., Furman, T., Nelson, W. R., Kalegga, P. K., & Barifaijo, E. (2021). Petrogenesis of primitive lavas from the Toro Ankole and Virunga Volcanic Provinces: Metasomatic mineralogy beneath East Africa's Western Rift. Lithos, 396–397, 106192. https://doi.org/https://doi.org/10.1016/j.lithos.2021.106192

Plank, T., & Forsyth, D. W. (2016). Thermal structure and melting conditions in the mantle beneath the Basin and Range province from seismology and petrology. Geochemistry, Geophysics, Geosystems, 17(4), 1312–1338. https://doi.org/https://doi.org/10.1002/2015GC006205

Ranalli, G., & Murphy, D. C. (1987). Rheological stratification of the lithosphere. Tectonophysics, 132(4), 281–295. https://doi.org/https://doi.org/10.1016/0040-1951(87)90348-9

Rocchi, S., Armienti, P., D'Orazio, M., Tonarini, S., Wijbrans, J. R., & Di Vincenzo, G. (2002). Cenozoic magmatism in the western Ross Embayment: Role of mantle plume versus plate dynamics in the development of the West Antarctic Rift System. Journal of Geophysical Research: Solid Earth, 107(B9), ECV 5-1-ECV 5-22. https://doi.org/https://doi.org/10.1029/2001JB000515

Rocchi, S., Bracciali, L., Di Vincenzo, G., Gemelli, M., & Ghezzo, C. (2011). Arc accretion to the early Paleozoic Antarctic margin of Gondwana in Victoria Land. Gondwana Research, 19(3), 594–607. https://doi.org/10.1016/j.gr.2010.08.001

Rocchi, S., & Smellie, J. L. (2021). Chapter 5.1b Northern Victoria Land: petrology. In J. L. Smellie, K. S. Panter, & A. Geyer (Eds.), Volcanism in Antarctica: 200 Million Years of Subduction, Rifting and Continental Break-up (pp. 383–413). Geological Society, London, Memoirs. https://doi.org/10.1144/M55-2019-19

Rooney, T. O. (2020). The Cenozoic magmatism of East Africa: Part V – Magma sources and processes in the East African Rift. Lithos, 360–361, 105296. https://doi.org/10.1016/j.lithos.2019.105296

Rooney, T. O., Herzberg, C., & Bastow, I. D. (2012). Elevated mantle temperature beneath East Africa. Geology, 40(1), 27–30. https://doi.org/10.1130/G32382.1

Saleeby, J., Le Pourhiet, L., Saleeby, Z., & Gurnis, M. (2012). Epeirogenic transients related to mantle lithosphere removal in the southern Sierra Nevada region, California: Part I. Implications of thermomechanical modeling. Geosphere, 8(6), 1286–1309. https://doi.org/10.1130/GES00746.1

Saleeby, J., Saleeby, Z., & Le Pourhiet, L. (2013). Epeirogenic transients related to mantle lithosphere removal in the southern Sierra Nevada region, California: Part II. Implications of rock uplift and basin subsidence relations. Geosphere, 9(3), 394–425. https://doi.org/10.1130/GES00816.1

Salvini, F., Brancolini, G., Busetti, M., Storti, F., Mazzarini, F., & Coren, F. (1997). Cenozoic geodynamics of the Ross Sea region, Antarctica: Crustal extension, intraplate strike-slip faulting, and tectonic inheritance. Journal of Geophysical Research: Solid Earth, 102(B11), 24669–24696. https://doi.org/https://doi.org/10.1029/97JB01643

Sauli, C., Sorlien, C., Busetti, M., De Santis, L., Geletti, R., Wardell, N., & Luyendyk, B. P. (2021). Neogene Development of the Terror Rift, Western Ross Sea, Antarctica. Geochemistry, Geophysics, Geosystems, 22(3), 1–20. https://doi.org/10.1029/2020GC009076

Schmeling, H., & Wallner, H. (2012). Magmatic lithospheric heating and weakening during continental rifting: A simple scaling law, a 2-D thermomechanical rifting model and the East African Rift System. Geochemistry, Geophysics, Geosystems, 13(8). https://doi.org/https://doi.org/10.1029/2012GC004178

Shen, W., Wiens, D. A., Anandakrishnan, S., Aster, R. C., Gerstoft, P., Bromirski, P. D., Hansen, S. E., Dalziel, I. W. D., Heeszel, D. S., Huerta, A. D., Nyblade, A. A., Stephen, R., Wilson, T. J., & Winberry, J. P. (2018). The Crust and Upper Mantle Structure of Central and West Antarctica From Bayesian Inversion of Rayleigh Wave and Receiver Functions. Journal of Geophysical Research: Solid Earth, 123(9), 7824–7849. https://doi.org/https://doi.org/10.1029/2017JB015346

Shen, W., Wiens, D. A., Stern, T., Anandakrishnan, S., Aster, R. C., Dalziel, I., Hansen, S., Heeszel, D. S., Huerta, A., Nyblade, A., Wilson, T. J., & Winberry, J. P. (2017). Seismic evidence for lithospheric foundering beneath the southern Transantarctic Mountains, Antarctica. Geology, 46(1), 71–74. https://doi.org/10.1130/G39555.1

Siddoway, C. S. (2008). Tectonics of the West Antarctic Rift System: New Light on the History and Dynamics of Distributed Intracontinental Extension. In A. K. Cooper, P. J. Barrett, H. Stagg, B. Storey, E. Stump, W. Wise, J. Anderson, J. Barron, P. Bart, D. Blankenship, F. Davey, M. Diggles, C. Finn, P. Fitzgerald, F. Florindo, J. Francis, D. Futterer, J. Gamble, J. Goodge, … T. Wilson (Eds.), Antarctica: A Keystone in a Changing World (pp. 91–114). The National Academies Press Proceedings of the 10th International Symposium on Antarctic Earth. https://doi.org/10.3133/of2007-1047.kp09

Siddoway, C. S., Sass, L. C., & Esser, R. P. (2005). Kinematic history of western Marie Byrd Land, West Antarctica: Direct evidence from Cretaceous mafic dykes. Geological Society Special Publication, 246(June 2019), 417–438. https://doi.org/10.1144/GSL.SP.2005.246.01.17

Sims, K. W. W., Blichert-Toft, J., Kyle, P. R., Pichat, S., Gauthier, P.-J., Blusztajn, J., Kelly, P., Ball, L., & Layne, G. (2008). A Sr, Nd, Hf, and Pb isotope perspective on the genesis and long-term evolution of alkaline magmas from Erebus volcano, Antarctica. Journal of Volcanology and Geothermal Research, 177(3), 606–618. https://doi.org/https://doi.org/10.1016/j.jvolgeores.2007.08.006

Smellie, J. L., & Martin, A. P. (2021). Chapter 5.2a Erebus Volcanic Province: volcanology. In J. L. Smellie, K. S. Panter, & A. Geyer (Eds.), Volcanism in Antarctica: 200 Million Years of Subduction, Rifting and Continental Break-up (pp. 415–446). Geological Society of London, Memoirs. https://doi.org/10.1144/M55-2018-62

Smellie, J. L., Martin, A. P., Panter, K. S., Kyle, P., & Geyer, A. (2020). Magmatism in Antarctica and its relation to Zealandia. New Zealand Journal of Geology and Geophysics, 63(4), 578–588. https://doi.org/10.1080/00288306.2020.1781666

Smellie, J. L., & Rocchi, S. (2021). Chapter 5.1a Northern Victoria Land: volcanology. In J. L. Smellie, K. S. Panter, & A. Geyer (Eds.), Volcanism in Antarctica: 200 Million Years of Subduction, Rifting and

Continental Break-up (pp. 347–381). Geological Society of London, Memoirs. https://doi.org/10.1144/M55-2018-60

Spiegel, C., Lindow, J., Kamp, P. J. J., Meisel, O., Mukasa, S., Lisker, F., Kuhn, G., & Gohl, K. (2016). Tectonomorphic evolution of Marie Byrd Land – Implications for Cenozoic rifting activity and onset of West Antarctic glaciation. Global and Planetary Change, 145, 98–115. https://doi.org/10.1016/j.gloplacha.2016.08.013

Stewart, J. H. (1971). Basin and Range Structure: A System of Horsts and Grabens Produced by Deep-Seated Extension. GSA Bulletin, 82(4), 1019–1044. https://doi.org/10.1130/0016-7606(1971)82[1019:BARSAS]2.0.CO;2

Storey, B. C., & Granot, R. (2021). Chapter 1.1 Tectonic history of Antarctica over the past 200 million years. In J. L. Smellie, K. S. Panter, & A. Geyer (Eds.), Volcanism in Antarctica: 200 Million Years of Subduction, Rifting and Continental Break-up (pp. 9–17). Geological Society of London, Memoirs. https://doi.org/10.1144/M55-2018-38

Storey, B. C., Leat, P. T., Weaver, S. D., Pankhurst, R. J., Bradshaw, J. D., & Kelley, S. (1999). Mantle plumes and Antarctica-New Zealand rifting: evidence from mid-Cretaceous mafic dykes. Journal of the Geological Society, 156(4), 659–671.

Tinto, K. J., Padman, L., Siddoway, C. S., Springer, S. R., Fricker, H. A., Das, I., Caratori Tontini, F., Porter, D. F., Frearson, N. P., Howard, S. L., Siegfried, M. R., Mosbeux, C., Becker, M. K., Bertinato, C., Boghosian, A., Brady, N., Burton, B. L., Chu, W., Cordero, S. I., … Bell, R. E. (2019). Ross Ice Shelf response to climate driven by the tectonic imprint on seafloor bathymetry. Nature Geoscience, 12(6), 441–449. https://doi.org/10.1038/s41561-019-0370-2

Toro, G. Di, Hirose, T., Nielsen, S., Pennacchioni, G., & Shimamoto, T. (2006). Natural and Experimental Evidence of Melt Lubrication of Faults During Earthquakes. Science, 311(5761), 647–649. https://doi.org/10.1126/science.1121012

Trey, H., Cooper, A. K., Pellis, G., Della Vedova, B., Cochrane, G., Brancolini, G., & Makris, J. (1999). Transect across the West Antarctic rift system in the Ross Sea, Antarctica. Tectonophysics, 301(1–2), 61–74. https://doi.org/10.1016/S0040-1951(98)00155-3

van Wijk, J. W., Lawrence, J. F., & Driscoll, N. W. (2008). Formation of the Transantarctic Mountains related to extension of the West Antarctic Rift system. Tectonophysics, 458(1–4), 117–126. https://doi.org/10.1016/j.tecto.2008.03.009

Wallner, H., & Schmeling, H. (2011). Sensitivity analysis of rift induced delamination with application to Rwenzori Mountains. Geophysical Journal International, 187(3), 1135–1145. https://doi.org/10.1111/j.1365-246X.2011.05237.x

Weaver, S. D., Storey, B. C., Pankhurst, R. J., Mukasa, S. B., DiVenere, V. J., & Bradshaw, J. D. (1994). Antarctica-New Zealand rifting and Marie Byrd Land lithospheric magmatism linked to ridge subduction and mantle plume activity. Geology, 22(9), 811–814. https://doi.org/10.1130/0091-7613(1994)022<0811:ANZRAM>2.3.CO;2

Wenman, C. P., Harry, D. L., & Jha, S. (2020). Post Middle Miocene Tectonomagmatic and Stratigraphic Evolution of the Victoria Land Basin, West Antarctica. Geochemistry, Geophysics, Geosystems, 21(3). https://doi.org/10.1029/2019GC008568

Wernicke, B. (1992). Cenozoic extensional tectonics of the U.S. Cordillera. In B. C. Burchfiel, P. W. Lipman, & M. L. Zoback (Eds.), The Cordilleran Orogen: Conterminous U.S. (pp. 553–581). Geological Society of America. https://doi.org/10.1130/DNAG-GNA-G3.553

White-Gaynor, A. L., Nyblade, A. A., Aster, R. C., Wiens, D. A., Bromirski, P. D., Gerstoft, P., Stephen, R. A., Hansen, S. E., Wilson, T., Dalziel, I. W. D., Huerta, A. D., Paul Winberry, J., & Anandakrishnan, S. (2019). Heterogeneous upper mantle structure beneath the Ross Sea Embayment and Marie Byrd Land, West Antarctica, revealed by P-wave tomography. Earth and Planetary Science Letters, 513, 40–50. https://doi.org/10.1016/j.epsl.2019.02.013

Wiens, D. A., Shen, W., & Lloyd, A. J. (2023). The seismic structure of the Antarctic upper mantle. In A. P. Martin & W. van der Wal (Eds.), The Geochemistry and Geophysics of the Antarctic Mantle (pp. 195–212). Geological Society of London, Memoirs. https://doi.org/10.1144/M56-2020-18

Wilch, T. I., McIntosh, W. C., & Panter, K. S. (2021). Chapter 5.4a Marie Byrd Land and Ellsworth Land: volcanology. In J. L. Smellie, K. S. Panter, & A. Geyer (Eds.), Volcanism in Antarctica: 200 Million Years of Subduction, Rifting and Continental Break-up (pp. 515–576). Geological Society of London, Memoirs. https://doi.org/10.1144/M55-2019-39

Zimmerman, M. E., & Kohlstedt, D. L. (2004). Rheological Properties of Partially Molten Lherzolite. Journal of Petrology, 45(2), 275–298. https://doi.org/10.1093/petrology/egg089

CONCLUSIONS

In this dissertation I explored the causes and sources of syn-rift magmatism, and their potential impacts on rifting processes that drive continental divergent plate boundaries to break-up. In the first chapter, I evaluated the melting of a compositionally heterogeneous mantle and associated melt production with a newly developed 1D geodynamic tool, MELT1D. This tool simulates extension of the lithosphere and a rising asthenosphere and calculates the resulting pressure-temperature conditions. Pressure and temperature in the lithosphere and asthenosphere are then used to evaluate melting of user-defined lithologies. In chapter 1, I used MELT1D to evaluate the melting of dry and wet depleted lherzolite mantle, dry and wet fertile lherzolite mantle, pyroxenite, and basalt for a range of geodynamic conditions that span global rifts. The results show that there is a relative sequence of melting with mafic and hydrous sources melting first at the onset and during early rifting. As extension proceeds, anhydrous fertile ultramafic sources melt (e.g., pyroxenite and pyrolytic compositions), and as rifting approaches continental breakup, depleted lherzolite begins to melt. Also, the results suggest that the greatest extent of melting occurs at the lithosphere-asthenosphere boundary (LAB). The models show that the parameters with the greatest impact on timing and volumes of magmatism are mantle composition, mantle temperatures, and lithosphere thickness. These results suggest that a cool/thick lithosphere has more potential to store fusible sources than thin/warm lithosphere and thus has a greater ability to produce early syn-rift magmatism.

In the second chapter, I investigated the impacts of latent heat consumed during syn-rift magmatism and how the melting of a multi-lithology mantle may affect the thermal, magmatic, and structural evolution of a rift. To consider the latent heat of melting in the lithosphere and asthenosphere, MELT1D was updated. This modified version of MELT1D, MELT1D2, was used to evaluate three mantle compositional models: a depleted lherzolite mantle model (100% DMM), a moderately metasomatized mantle model (85% DMM, 15% pyroxenite), and a highly metasomatized mantle model (70% DMM, 15% pyroxenite, and 15% relatively more mafic pyroxenite). The results showed that melting and associated cooling are greatest at the LAB (similar to chapter 1 findings). Here, temperatures cool by as much as 30 °C in the highly metasomatized mantle model which experiences the most melting. Because most cooling associated with latent heat of melting occurs at the LAB (where the lithosphere is already very weak compared to the top of the subcontinental lithospheric mantle) it has little effect on the net lithospheric strength. Results also show that early melting of fusible lithologies inhibits later melting of less fusible lithologies due to cooling associated with the latent heat of melting. Thus, less fusible lithologies may require more thinning/extension or an influx of heat to melt and will likely produce less magmatism if more fusible lithologies are present. This suggests a mechanism in which relatively less fusible lithologies could be stored until later stages of extension than would normally be expected. For example, the syn-rift melting of a moderately fusible lithology (e.g., pyroxenite) in a multi-lithology mantle may be delayed due to melting and associated cooling of more fusible lithologies (e.g., basaltic sources) until later stages of extension than would be expected if more fusible sources were not present.

In the third chapter, I tested the hypothesis that WARS (West Antarctic Rift System) syn-rift magmatism was caused by decompression melting of fusible sources in the mantle. To do this, I modified the modeling code ASPECT (Advanced Solver for Planetary Evolution, Convection, and Tectonics) to allow for melting of new lithologies in a rheologically layered earth model undergoing extension. These WARS models generally consisted of a cratonic region with thick lithosphere and thinner crust (East Antarctica) transitioning into an accreted region with thinner lithosphere but thicker crust (West Antarctica). Initial conditions and starting model geometries were used to simulate the WARS based on previous geodynamic models and geophysical and geologic observations. Using ASPECT, I evaluated WARS syn-rift melting of depleted lherzolite, fertile lherzolite, basalt, and pyroxenite. Each lithology was evaluated for temperature models with mantle potential temperatures (T_p) of 1270 °C, 1300 °C, and 1330 °C. Results show that models with a relatively cool mantle (T_p = 1300 °C) best-fit the structural and magmatic evolution of the WARS. Of the lithologies tested, only basalt melted, suggesting that similar fusible sources (i.e. hydrous compositions) could also be responsible for WARS syn-rift magmatism. This suggests that the melting of fusible sources in the lithosphere and asthenosphere may explain magmatism along the western flank without elevated mantle temperatures like those associated with a plume. However, the model does not preclude the presence of a plume under Ross Island. No melting occurs along the eastern flank in the best fit model which is inconsistent with observations of WARS Cenozoic magmatism. This implies that the melting of fusible mantle sources alone could not explain magmatism along the eastern flank of the WARS which is consistent with the presence of the well-known Marie Byrd Land plume. Results also show that the modeled structural evolution of the WARS is the same whether melt is present or not which implies that the structural evolution is not impacted by magmatism. However, magmatism in the models is closely tied to the structural evolution suggesting that the WARS is a passive rift.

This dissertation shows that fusible lithologies can produce syn-rift magmatism potentially beginning at the earliest stages of extension. However, the models also show that the ability of the mantle to host these materials is limited by the pressure-temperature conditions of the lithosphere and asthenosphere at the onset of rifting. For example, the most fusible sources (mafic and hydrous lithologies) typically sit near or at their solidi prior to rifting when present in the mantle such that at the onset of extension they will begin to melt. Thus, these sources are not easily stored for later stages of rifting. In the models, magmatism had little to no significant impact on the structural evolution of a rift, however, magmatism was heavily influenced by the structural evolution. We note that the WARS has been argued to be a relatively cool rift system so the models shown here do not speak to the relationship between magmatism and the structural evolution of warmer rift systems.

Future work building on this dissertation should focus on exploring the relationship between the melting parameters and the structural style of rifts using geodynamic models. This includes but is not limited to testing the melting of different lithologies, melt viscosities, melt densities, melt weakening constants, and melt permeability models. A limitation of the finite-element geodynamic models developed to study the WARS is the (current) inability of ASPECT to include more than one melting relation (mantle lithology) in a given simulation. Future work should also be focused on developing geodynamic models that allow for the melting of multiple lithologies in the same model. Such models would allow for more consistency between the rheology of an earth layer or other distinct geometric body in a model, and its melting behavior.